



Calhoun: The NPS Institutional Archive
DSpace Repository

Theses and Dissertations

1. Thesis and Dissertation Collection, all items

2009-06

Computational fluid dynamic model of steam ingestion into a transonic compressor

Hedges, Collin R.

Monterey, California. Naval Postgraduate School

<http://hdl.handle.net/10945/4785>

This publication is a work of the U.S. Government as defined in Title 17, United States Code, Section 101. Copyright protection is not available for this work in the United States.

Downloaded from NPS Archive: Calhoun



<http://www.nps.edu/library>

Calhoun is the Naval Postgraduate School's public access digital repository for research materials and institutional publications created by the NPS community. Calhoun is named for Professor of Mathematics Guy K. Calhoun, NPS's first appointed -- and published -- scholarly author.

Dudley Knox Library / Naval Postgraduate School
411 Dyer Road / 1 University Circle
Monterey, California USA 93943



NAVAL POSTGRADUATE SCHOOL

MONTEREY, CALIFORNIA

THESIS

**COMPUTATIONAL FLUID DYNAMIC MODEL OF
STEAM INGESTION INTO A TRANSONIC COMPRESSOR**

by

Collin R. Hedges

June 2009

Thesis Advisor:
Second Reader:

Anthony J. Gannon
Garth V. Hobson

Approved for public release; distribution is unlimited

THIS PAGE INTENTIONALLY LEFT BLANK

REPORT DOCUMENTATION PAGE			<i>Form Approved OMB No. 0704-0188</i>	
Public reporting burden for this collection of information is estimated to average 1 hour per response, including the time for reviewing instruction, searching existing data sources, gathering and maintaining the data needed, and completing and reviewing the collection of information. Send comments regarding this burden estimate or any other aspect of this collection of information, including suggestions for reducing this burden, to Washington headquarters Services, Directorate for Information Operations and Reports, 1215 Jefferson Davis Highway, Suite 1204, Arlington, VA 22202-4302, and to the Office of Management and Budget, Paperwork Reduction Project (0704-0188) Washington DC 20503.				
1. AGENCY USE ONLY (Leave blank)		2. REPORT DATE June 2009	3. REPORT TYPE AND DATES COVERED Master's Thesis	
4. TITLE AND SUBTITLE Computational Fluid Dynamic Model of Steam Ingestion into a Transonic Compressor			5. FUNDING NUMBERS	
6. AUTHOR(S) Collin R. Hedges				
7. PERFORMING ORGANIZATION NAME(S) AND ADDRESS(ES) Naval Postgraduate School Monterey, CA 93943-5000			8. PERFORMING ORGANIZATION REPORT NUMBER	
9. SPONSORING /MONITORING AGENCY NAME(S) AND ADDRESS(ES) N/A			10. SPONSORING/MONITORING AGENCY REPORT NUMBER	
11. SUPPLEMENTARY NOTES The views expressed in this thesis are those of the author and do not reflect the official policy or position of the Department of Defense or the U.S. Government.				
12a. DISTRIBUTION / AVAILABILITY STATEMENT Approved for public release; distribution is unlimited			12b. DISTRIBUTION CODE	
13. ABSTRACT (maximum 200 words) <p>The U.S. Navy's concern with steam-induced jet engine stall has become more pertinent with the introduction of the F-35C. During take offs on aircraft carriers, steam from aging catapult systems can potentially seep onto the flight deck. When ingested into jet engines, this steam may increase the engines' susceptibility to stall. The serpentine air inlet ducts and single engine of the F-35C could make it especially vulnerable to this steam-induced stall during takeoff. To better understand and predict steam-induced stall, this study created a computational fluid dynamics (CFD) simulation of steam-induced stall on a single blade passage of a compressor rotor. A single blade passage of the transonic Sanger rotor was generated using computer modeling software. This model was then used in the ANSYS CFX computational fluid dynamics program to simulate steady-state and steam ingestion operations at 95% and 100% rotor design speeds. These CFD simulations generated compressor maps and throttle and steam-induced stall points. The CFD results were then compared to results from throttle-induced stall and steam-induced stall experiments conducted on the Sanger rotor in the transonic compressor rig. This study verified that CFD can estimate steam-induced stall operating margin reduction.</p>				
14. SUBJECT TERMS Computational Fluid Dynamics, Transonic, Compressor, Steam Ingestion, Sanger Rotor			15. NUMBER OF PAGES 123	
			16. PRICE CODE	
17. SECURITY CLASSIFICATION OF REPORT Unclassified	18. SECURITY CLASSIFICATION OF THIS PAGE Unclassified	19. SECURITY CLASSIFICATION OF ABSTRACT Unclassified	20. LIMITATION OF ABSTRACT UU	

THIS PAGE INTENTIONALLY LEFT BLANK

Approved for public release; distribution is unlimited

**COMPUTATIONAL FLUID DYNAMIC MODEL OF STEAM INGESTION INTO
A TRANSONIC COMPRESSOR**

Collin R. Hedges
Ensign, United States Navy
B.S., United States Naval Academy, 2008

Submitted in partial fulfillment of the
requirements for the degree of

MASTER OF SCIENCE IN MECHANICAL ENGINEERING

from the

**NAVAL POSTGRADUATE SCHOOL
June 2009**

Author: Collin R. Hedges

Approved by: Anthony J. Gannon
Thesis Advisor

Garth V. Hobson
Second Reader

Knox T. Millsaps
Chairman, Department of Mechanical and Astronautical
Engineering

THIS PAGE INTENTIONALLY LEFT BLANK

ABSTRACT

The U.S. Navy's concern with steam-induced jet engine stall has become more pertinent with the introduction of the F-35C. During take offs on aircraft carriers, steam from aging catapult systems can potentially seep onto the flight deck. When ingested into jet engines, this steam may increase the engines' susceptibility to stall. The serpentine air inlet ducts and single engine of the F-35C could make it especially vulnerable to this steam-induced stall during takeoff. To better understand and predict steam-induced stall, this study created a computational fluid dynamics (CFD) simulation of steam-induced stall on a single blade passage of a compressor rotor. A single blade passage of the transonic Sanger rotor was generated using computer modeling software. This model was then used in the ANSYS CFX computational fluid dynamics program to simulate steady-state and steam ingestion operations at 95% and 100% rotor design speeds. These CFD simulations generated compressor maps and throttle and steam-induced stall points. The CFD results were then compared to results from throttle-induced stall and steam-induced stall experiments conducted on the Sanger rotor in the transonic compressor rig. This study verified that CFD can estimate steam-induced stall operating margin reduction.

THIS PAGE INTENTIONALLY LEFT BLANK

TABLE OF CONTENTS

I.	INTRODUCTION.....	1
II.	EXPERIMENTAL FACILITY AND PROCEDURE	3
A.	THROTTLE STALL CASES	4
B.	STEAM INGESTION STALL CASES.....	4
III.	MODEL CONSTRUCTION.....	7
IV.	STEADY-STATE ANALYSIS.....	17
A.	COMPUTATIONAL GRID ITERATION TESTING	17
B.	REFINED COMPUTATIONAL GRID EXPERIMENTATION	19
C.	FINAL STEADY-STATE SIMULATION RESULT GENERATION.....	23
V.	QUASI-STEADY-STATE ANALYSIS.....	25
A.	THROTTLE QUASI-STEADY-STATE SIMULATIONS	26
B.	STEAM INGESTION STALL.....	27
VI.	RESULTS AND DISCUSSION	31
A.	PHYSICAL EXPERIMENTAL COMPRESSOR MAPS.....	31
B.	NEW STEAM INGESTION DATA.....	33
C.	TRANSONIC COMPRESSOR RIG MODIFICATIONS	35
D.	OVERALL CFD PERFORMANCE TRENDS.....	38
1.	95 Percent Speed	38
2.	100 Percent Speed	41
3.	The Effects of Periodicity	44
E.	INDIVIDUAL CFD SIMULATION OBSERVATIONS.....	45
1.	Throttle Simulations	45
2.	Steam Ingestion Simulations.....	47
F.	STEAM INGESTION RAMP FUNCTION SLOPE	54
VII.	CONCLUSIONS	57
VIII.	RECOMMENDATIONS.....	59
	LIST OF REFERENCES.....	61
APPENDIX A:	SAMPLE BLADE PROFILES	63
APPENDIX B:	MODAL ANALYSIS ON A ROTOR BLADE.....	65
APPENDIX C:	GRID ITERATION PROCESS.....	69
APPENDIX D:	FINAL REFINED BLADE GRID MESH OPTIONS	73
APPENDIX E:	STEADY-STATE SIMULATION SOLVER SETTINGS	75
APPENDIX F:	THROTTLE STALL SIMULATION SOLVER SETTINGS	83
APPENDIX G:	STEAM INGESTION SIMULATION SOLVER SETTINGS	91
APPENDIX H:	TABULATED EXPERIMENTAL RESULTS.....	99
	INITIAL DISTRIBUTION LIST	105

THIS PAGE INTENTIONALLY LEFT BLANK

LIST OF FIGURES

Figure 1.	F-18 Undergoing Steam-Induced Pop Stall at Naval Station Patuxent River by Hurley [From 6]	1
Figure 2.	Sanger Rotor on the Transonic Compressor Rig	3
Figure 3.	Current Kulite Arrangement	4
Figure 4.	Diagram of Thermocouple Array.....	5
Figure 5.	Transonic Compressor Rig Inlet with Flow Separator	5
Figure 6.	Previous Structured Computational Grid Constructed by Zarro [After 4]	7
Figure 7.	Axial Cross Section of Annulus with one Rotor.....	8
Figure 8.	Compressor Annulus (left) and Single Rotor Passage Models (right).....	9
Figure 9.	Final Rotor Blade Model with Profiles Shown.....	10
Figure 10.	Periodic Boundaries.....	11
Figure 11.	Inlet Boundary	11
Figure 12.	Outlet Boundary.....	12
Figure 13.	Rotor Blade and Hub Boundary.....	12
Figure 14.	Outer Casing Boundary.....	13
Figure 15.	Surface Grid on the Hub Nose Before and After Refinement	14
Figure 16.	Final Computational Grid	15
Figure 17.	100% Speed Grid Iteration Total Pressure Ratio vs. Mass Flow Rate Compressor Map.....	18
Figure 18.	100% Speed Grid Iteration Total to Total Isentropic Efficiency vs. Mass Flow Rate Compressor Map	19
Figure 19.	Maximum Residuals from RMS Convergent Simulation (left) and MAX Convergent Simulation (right)	22
Figure 20.	95% Speed Experimental and CFD Inlet Temperature Plots.....	28
Figure 21.	95% Speed Experimental and CFD Air Mass Fraction Plots	28
Figure 22.	Pressure Ratio vs. Mass Flow Rate Compressor	31
Figure 23.	Efficiency vs. Mass Flow Rate Compressor Map.....	32
Figure 24.	95% Speed Physical Steam Ingestion Event Probe Temperature and Rotor Speed vs. Time Plot	34
Figure 25.	Spatial Temperature Distribution during 95% Speed Steam-Induced Stall.....	35
Figure 26.	Probe Height vs. Temperature Plot at 70% Speed with Flow Separator	36
Figure 27.	Panel Covering Inlet of Transonic Compressor Rig with Upper Section Steam Injection Pipe Location.....	37
Figure 28.	Probe Height vs. Temperature Plot at 90% Speed with Separator, Panel, and Steam Pipe Location Change	38
Figure 29.	95% Speed CFD and Physical Experiment Total Pressure Ratio vs. Mass Flow Rate Plot.....	39
Figure 30.	95% Speed CFD and Physical Experiment Total to Total Isentropic Efficiency vs. Mass Flow Rate Plot.....	40
Figure 31.	100% Speed CFD and Physical Experiment Total Pressure Ratio vs. Mass Flow Rate Plot.....	42

Figure 32.	100% Speed CFD and Physical Experiment Total to Total Isentropic Efficiency vs. Mass Flow Rate Plot.....	42
Figure 33.	95% Speed Outer Casing Pressure Distribution at Open Throttle, 7.715 kg/s (3.500 lbm/s)	45
Figure 34.	95% Speed Outer Casing Pressure Distribution Near Maximum Efficiency, 7.402 kg/s (3.358 lbm/s).....	46
Figure 35.	95% Speed Outer Casing Pressure Distribution at the Steam Stall Point, 6.875 kg/s (3.118 lbm/s)	46
Figure 36.	95% Speed Outer Casing Pressure Distribution Near Stall, 6.620 kg/s (3.005 lbm/s).....	47
Figure 37.	95% Speed Outer Casing Pressure Distribution, Time = 0 seconds, Inlet Temperature = 293.15 K (527.67 °R)	48
Figure 38.	95% Speed Outer Casing Pressure Distribution After a Half Second of Steam Ingestion, Time = 2.5 seconds, Inlet Temperature = 296.75 K (534.15 °R).....	48
Figure 39.	95% Speed Outer Casing Pressure Distribution After One Second of Steam Ingestion, Time = 3 seconds, Inlet Temperature = 300.5 K (540.9 °R)	49
Figure 40.	95% Speed Outer Casing Pressure Distribution After 1.5 Seconds of Steam Ingestion, Time = 3.5 seconds, Inlet Temperature = 304.25 K (547.65 °R).....	49
Figure 41.	95% Speed Mass Flow Rate Plot as Steam Ingestion Occurs	50
Figure 42.	95% Speed Average Inlet Density Plot as Steam Ingestion Occurs	51
Figure 43.	95% Speed Mach One Isosurface, Time = 0 seconds, Inlet Temperature = 293.15 K (518.67 °R).....	52
Figure 44.	95% Speed Mach One Isosurface After a Half Second of Steam Ingestion, Time = 2.5 seconds, Inlet Temperature = 296.75 K (527.67 °R).....	53
Figure 45.	95% Speed Mach One Isosurface After One Second of Steam Ingestion, Time = 3 seconds, Inlet Temperature = 300.5 K (534.15 °R).....	53
Figure 46.	95% Speed Mach One Isosurface After 1.5 Seconds of Steam Ingestion, Time = 3.5 Seconds, Inlet Temperature = 304.25 K (540.9 °R).....	54
Figure 47.	95% Speed Various Temperature Ramp Functions	55
Figure 48.	95% Speed Various Air Mass Fraction Ramp Functions	55
Figure 49.	Mode 1: 756.69 Hertz. The top of the blade moves back and forth. Not much twisting occurs in the blade.....	65
Figure 50.	Mode 2: 2,718.7 Hertz. The top of the blade twists. The front edge buckles.	66
Figure 51.	Mode 3: 2,932 Hertz. The front tip bends back and forth. The blade twists slightly.....	66
Figure 52.	Mode 4: 5,197.5 Hertz. The front tip bends back and forth, but less of the tip bends than in mode 3. The blade twists slightly.....	67
Figure 53.	Mode 5: 5,534.2 Hertz. The top of the blade twists and the front edge buckles.	67
Figure 54.	Split Surfaces on Outer Casing and Hub	69
Figure 55.	Fully Intact Outer Casing and Hub	70

LIST OF TABLES

Table 1.	Geometry Comparison of Grid Iterations	15
Table 2.	Comparison of Initial Mesh and Mesh after Three Steps of Adaptation	20
Table 3.	Experimental Throttle Stall Margin, Steam Stall Margin, and Stall Margin Reduction for 70%, 80%, 90%, 95%, and 100% Speeds.....	33
Table 4.	95% Speed Stall Margin Comparisons	41
Table 5.	Physical and Simulation Modal Frequency Comparison.....	65

THIS PAGE INTENTIONALLY LEFT BLANK

ACKNOWLEDGMENTS

I would like to thank all the professors and staff at the NPS Turbopropulsion Lab for providing me with the opportunity and support to conduct this research. In particular, I would like to acknowledge Professor Anthony Gannon, Professor Garth Hobson, John Gibson, Doug Seivwright, Lieutenant Lee Davis, USCG, and Seung Chul Back. I would also like to thank my family and the Class of 2008 Ensigns for their encouragement.

THIS PAGE INTENTIONALLY LEFT BLANK

LIST OF ACRONYMS AND ABBREVIATIONS

ANSYS Workbench	A simulation package that includes a mesh generation program, a modal analysis simulator, and CFX
CFD	Computational fluid dynamics
CFX	The computational fluid dynamics simulation program in ANSYS Workbench. It is divided into CFX-Pre, CFX-Solver, and CFX-Post. It uses an implicit solver and can run both steady-state and transient simulations
CFX-Pre	The module of CFX where boundary conditions and solver settings are selected. The first CFX program used while conducting a simulation
CFX-Post	The module of CFX where post processing on a completed simulation is conducted. It contains tools for calculating turbomachinery performance and creating contours and isosurfaces based on the flow field properties. The last CFX program used while conducting a simulation
CFX-Solver	The module of CFX that runs the solver program set up by CFX-Pre. It displays variable residuals as the simulation reaches convergence. The second CFX program used while conducting a simulation.
D	Hydraulic diameter
IGES file	Geometry file exported from Solid Edge and imported into ANSYS Workbench
\dot{m}	Measured compressor mass flow rate.
$\dot{m}_{\text{peak eff}}$	Compressor mass flow rate at peak efficiency
\dot{m}_{ref}	Corrected mass flow rate based on temperature (θ) and pressure ratio (δ). $\dot{m}_{\text{ref}} = \dot{m} \frac{\sqrt{\theta}}{\delta}$
\dot{m}_{surge}	Compressor mass flow rate at the onset of surge
Mesh Adaptation	A process conducted by CFX during a steady-state simulation where the computational grid is refined or coarsened based on one or many specified flow field parameters.
p	Measured pressure
p_{01}	Inlet stagnation pressure
p_{02}	Outlet stagnation pressure

P_{ref}	Reference pressure. 101.325 kPa (1 atm)
Performance Macro	Tools within CFX-Post to calculate performance characteristics of the rotor. Performance characteristics include total to total isentropic efficiency, mass flow rate, and pressure ratio
Pressure Ratio	Ratio of inlet to outlet stagnation pressures. $\frac{P_{02}}{P_{01}}$
R	Gas constant
Solid Edge	A solid modeling program
Stall Margin	$\frac{(\dot{m}_{peak\ eff} - \dot{m}_{surge})}{\dot{m}_{peak\ eff}}$
Stall Margin Reduction	$\frac{(\text{Throttle Induced Stall Margin} - \text{Steam Induced Stall Margin})}{\text{Throttle Induced Stall Margin}}$
STP file	Geometry file exported from Solid Edge and imported into ANSYS Workbench
T	Measured temperature
T_{01}	Inlet stagnation temperature
T_{ref}	Reference temperature, 288.15 K (518.67 °R)
γ	Specific heat ratio
δ	Non-dimensionalized pressure. $\frac{p}{P_{ref}}$
η_c	Compressor efficiency
θ	Non-dimensionalized temperature. $\frac{T}{T_{ref}}$
ν	kinematic viscosity
Ω	Rotational speed

I. INTRODUCTION

The U.S. Navy's concern with steam-induced jet engine stall has become more pertinent with the introduction of the F-35C Lightning II, carrier variant. During takeoffs on aircraft carriers, steam from aging catapult systems seeps onto the flight deck. When ingested into jet engines, this steam increases the engines' susceptibility to stall. In experiments conducted at Naval Air Station Patuxent River, steam ingestion caused pop stalls in F-18 aircraft. Figure 1 displays an F-18 undergoing steam-induced pop stall. The serpentine air inlet and single engine of the F-35C make it especially vulnerable to this steam-induced stall during takeoff.



Figure 1. F-18 Undergoing Steam-Induced Pop Stall at Naval Station Patuxent River by Hurley [From 6]

In order to investigate this phenomenon, the Naval Postgraduate School's Turbopropulsion Laboratory has conducted multiple studies on a rotor-stator stage of a transonic compressor using the Transonic Compressor Rig. Sanger [1] designed the rotor-stator stage at the NASA Glenn Research Center.

Previous to this study, Levis [2] reestablished steam and throttle-induced stall characteristics of the rig at 70% and 90% of design speed in the rotor-only configuration after the honeycomb air inlet duct was replaced. Payne [3] investigated stall precursors using hot film measurements in the rotor only configuration with throttle-induced stall at

90% and 95% of design speed and steam-induced stall at 70% of design speed. Zarro [4] studied steam-induced stall at 90% and 95% of design speed in the rotor only configuration. Zarro also composed a computational fluid dynamics model, using CFX, to replicate the rotor stage of the rig. Koessler [5] investigated stall precursors, and reestablished a performance map for the rotor only configuration at 70%, 90%, 95% and 100% of design speed. Using steam pressurized to 9 atm, Koessler examined steam-induced stall at 70%, 90%, and 95% of design speed. Using the rig in the stator and rotor configuration, Hurley [6] analyzed both steam and throttle-induced stall at 70%, 80%, 90%, 95%, and 100% of design speed.

The current study has produced a computational fluid dynamic model of a single blade passage of the Sanger transonic compressor rotor stage. This model produced compressor maps with throttle and steam ingestion stall points for 95% and 100% design speeds. In order to verify the model's accuracy, physical rotor only compressor performance was tested at 70%, 80%, 90%, 95%, and 100% design speeds. Throttle stall experiments were conducted for all speeds and steam ingestion experiments were conducted for all but 100% speed. New to these experiments was the partial ingestion of steam into the top half of the upstream throttle valve. By comparing the CFD and physical experimental results to each other, flow, shock, and stall behavior can be better understood and predicted.

II. EXPERIMENTAL FACILITY AND PROCEDURE

To establish the accuracy and validity of the CFD results, physical tests were conducted on the Transonic Compressor Rig. Two different experimental setups were used: a throttle stall setup and a steam-induced stall setup. The Transonic Compressor Rig was run in a rotor only configuration using a new and nearly pristine Sanger Rotor. Figure 2 displays the Sanger Rotor on the Transonic Compressor Rig.

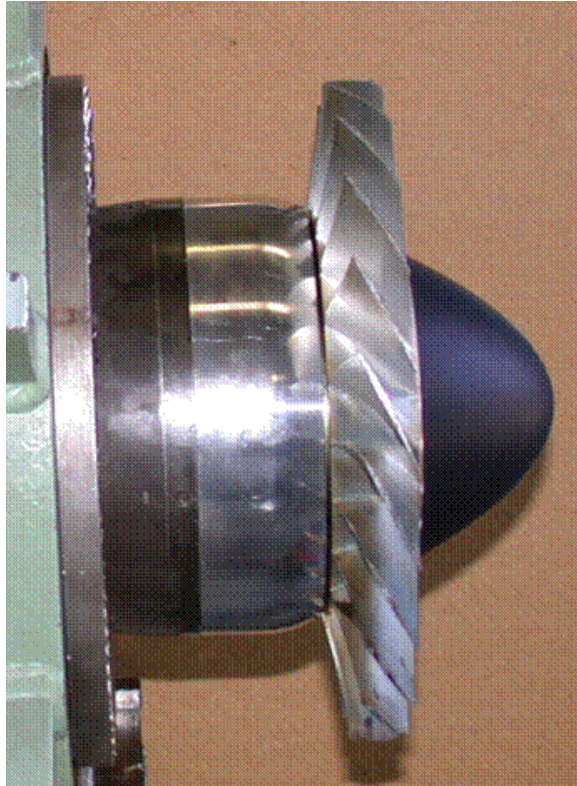


Figure 2. Sanger Rotor on the Transonic Compressor Rig

These experimental runs established compressor maps, throttle stall points, and steam-induced stall points for 70%, 80%, 90%, 95% speeds. At 100% speed the steam ingestion experiment was not conducted because of compressor damage and safety concerns. Payne [3], Zarro [4], and Hurley [6] have previously discussed the experimental setup, sensors, and data acquisition system used on the Transonic Compressor Rig.

A. THROTTLE STALL CASES

This study used the same sensor and data acquisition configuration as Hurley [6], except an additional Kulite sensor has been placed behind the rotor at 104% of the axial chord. Figure 3 shows the current Kulite arrangement.

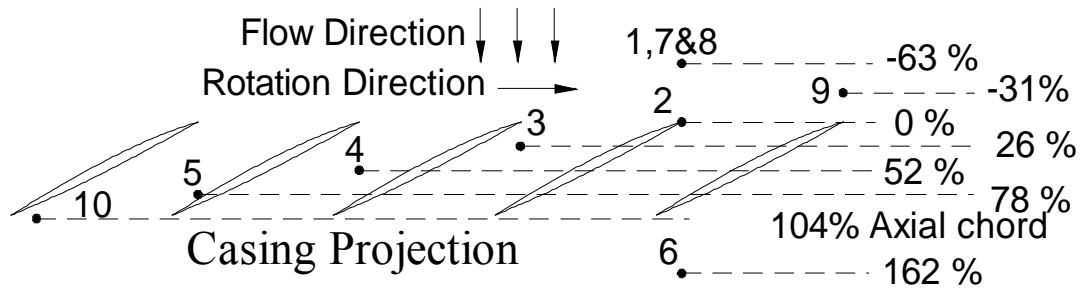


Figure 3. Current Kulite Arrangement

To establish compressor maps and capture high-speed data of the throttle stall event an experimental procedure detailed by [6] was used. The experimental procedure is summarized here. Starting at completely open, the throttle was closed in a series of steps. At each step, high-speed and low-speed data was collected. When the compressor neared stall, high-speed data was collected as the throttle closed in order to capture the entire stall event. The compressor maps for 70%, 80%, 90%, 95%, and 100% speeds with their respective throttle stall points can be found in Figures 22 and 23 of Chapter VI.

B. STEAM INGESTION STALL CASES

For steam ingestion trials, an experimental procedure and sensor array similar to Hurley's [6] was used. Changes from Hurley's work were the addition of six thermocouples placed upstream of the rotor to measure incoming steam-air mixture temperatures in the upper and lower half of the inlet. Figure 4 shows the thermocouple arrangement within the Transonic Compressor Rig in relation to the rotor.

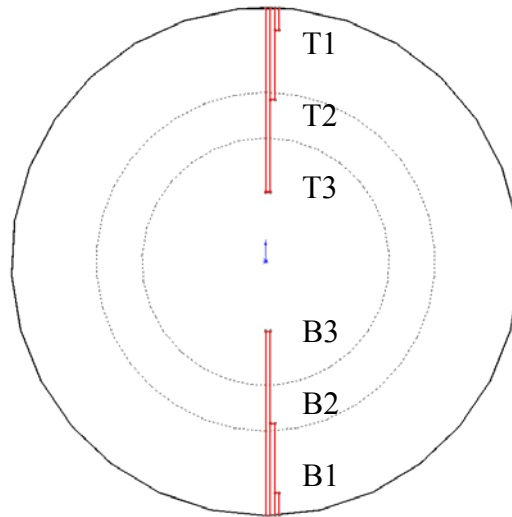


Figure 4. Diagram of Thermocouple Array

Measuring from the bottom of the annulus, thermocouples were placed at 12.7 mm (0.50 in), 50.8 mm (2.0 in), 101.6 mm (4.0 in), 177.8 mm (7.0 inches), 228.6 mm (9.0 inches), and 266.7 mm (10.5 inches). This thermocouple array was designed not only to record more accurate flow temperatures, but also to record the incoming flow temperature profile. Figure 5 displays the inlet flow separator that was positioned within the plenum upstream of the throttle.

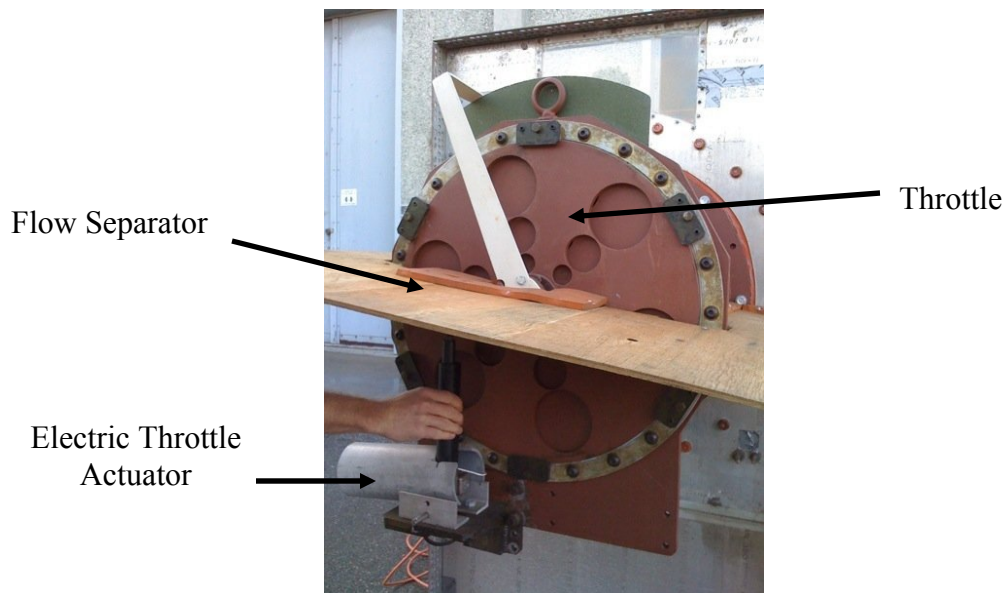


Figure 5. Transonic Compressor Rig Inlet with Flow Separator

Steam and air mixing occurred between the inlet and the rotor. By initially separating the lower half of the inlet from the upper, this steam and air mixing should be reduced. Less mixing should produce more concentrated steam slugs. A higher concentrated steam slug should simulate higher pressured steam ingestion without having to raise the pressure of the steam generator. These less mixed steam slugs should reduce the steam-induced stall margin, with steam-induced stall occurring earlier on the compressor map. Accurate steam ingestion data collected during these experiments will aid in constructing more realistic CFD simulations in future studies. During steam ingestion high speed data was collected to capture the steam-induced stall event. Steam ingestion trials were conducted at 70%, 80%, 90%, 95%, and 100% speeds in separated inlet configuration.

III. MODEL CONSTRUCTION

The transonic compressor rig's rotor had 22 blades, but for this study only a single passage was constructed for the computational fluid dynamic model. Focusing on one passage rather than the entire rotor significantly reduced the computational time required for simulations. Zarro [4] previously created a computational fluid dynamic model of one rotor passage, but Zarro's model was composed of a structured grid and this study's model was composed of an unstructured grid with inflation layers. In order to facilitate the construction of a structured grid, Zarro's passage had considerable curvature, as seen in Figure 6. This curvature may have increased errors in the computation at the periodic side boundaries of the rotor passage. By creating a geometrically simpler rotor passage, the accuracy of the computational fluid dynamic model is expected to increase. An unstructured grid also allows for simpler computational mesh refinement than a structured mesh.

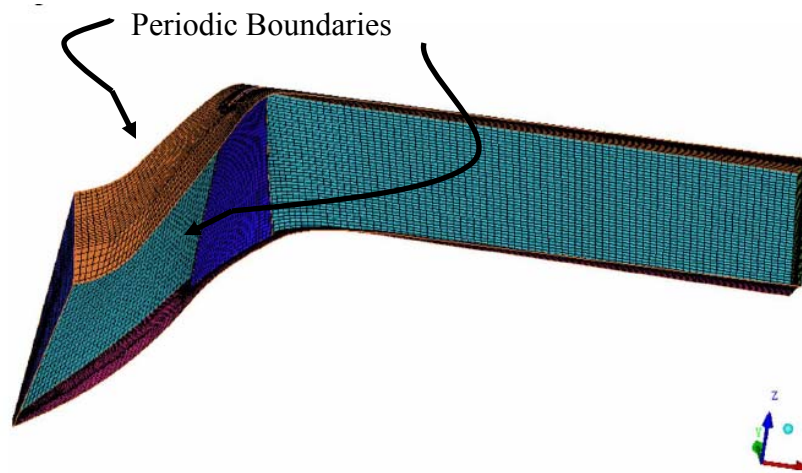


Figure 6. Previous Structured Computational Grid Constructed by Zarro [After 4]

The compressor annulus and blade geometry for this study's model was provided by Zarro [4] and Hurley [6]. Both the annulus and rotor blade geometries have their origin set at the leading edge at the hub of the rotor blade. An axial cross-section of the annulus with one rotor blade is shown in Figure 7.

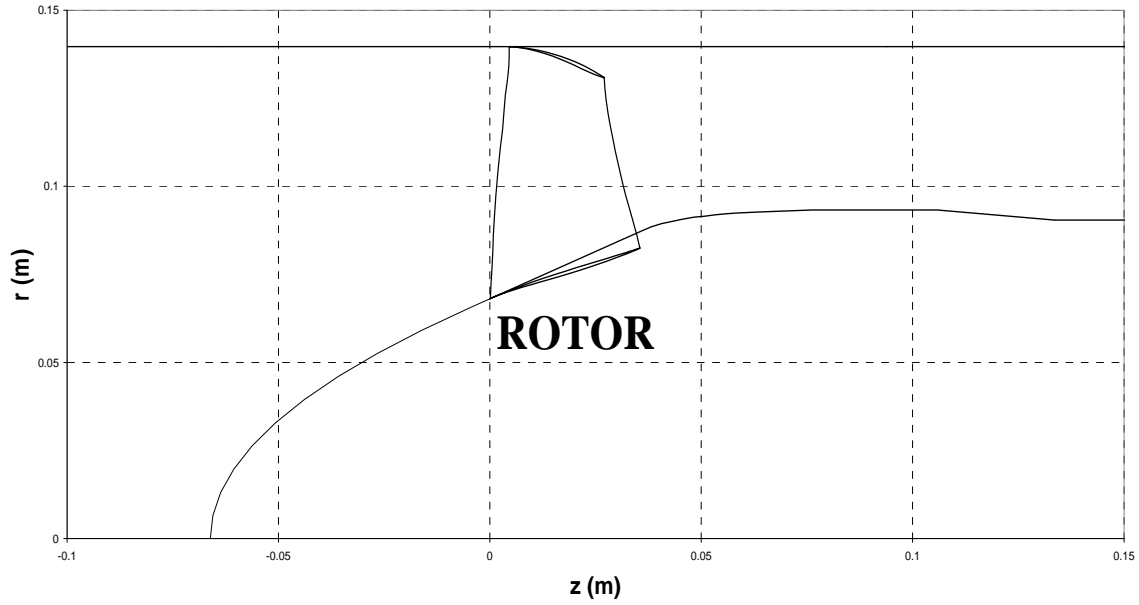


Figure 7. Axial Cross Section of Annulus with one Rotor

The rotor blade and the annulus models were each constructed separately using Solid Edge and then combined into one model using ANSYS Workbench. Figure 8 shows the annulus model and the single rotor passage model. The rotor passage model extended 33.87 mm (1.335 in) in front of the nose cone and 38.00 mm (1.496 in) past the rotor blade. The single rotor passage formed a wedge with an angle of 16.36 degrees ($360/22$), which corresponded to $1/22$ of the entire annulus. The passage began axially, then turned sharply through 16 degrees to include the whole rotor blade, finally returning to axial after passing the blade. By only turning the passage while passing the blade, the model became geometrically simpler than Zarro's. This model was also the first CFD model of the Sanger rotor to include the nose-cone, which may significantly affect the flow into the rotor, thus including it may create more accurate simulations.

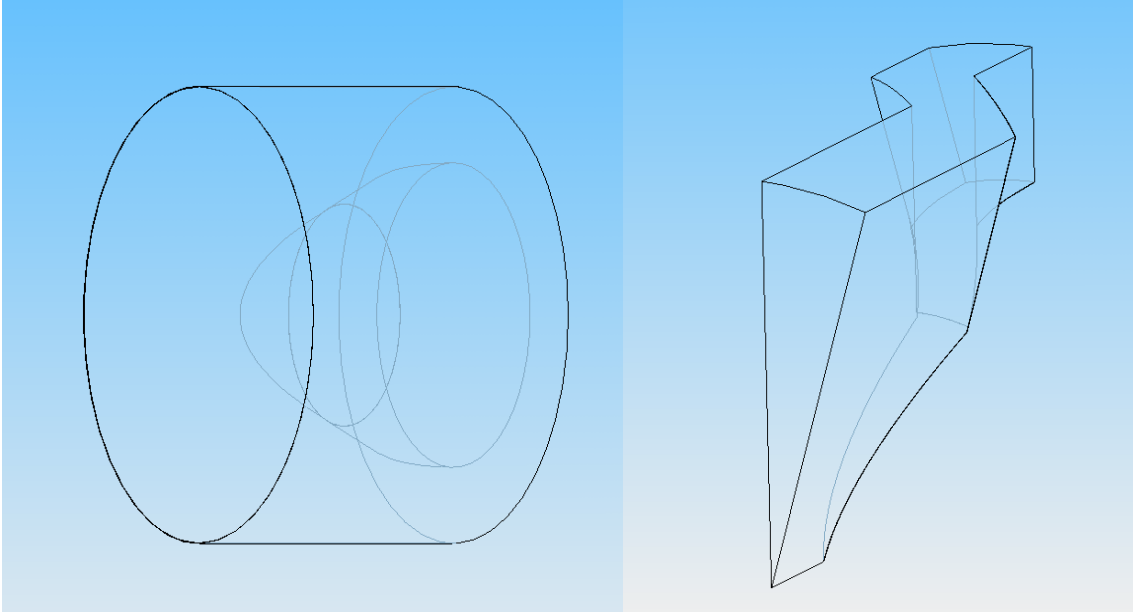


Figure 8. Compressor Annulus (left) and Single Rotor Passage Models (right)

In order to create the blade model, blade profiles at different heights were constructed. Sample blade profiles can be found in Appendix A. These profiles were used to define the two side surfaces of the blade. The top most and bottom most profiles were used to define the bottom and top surfaces of blade. These four surfaces were then stitched together to form the solid model of the blade. For initial blade models only three profiles were used, but the final model used eleven profiles. The rotor blade model was initially made to extend past the outer radius of the annulus. This extension allowed for the construction of a preliminary computational model with no tip gap between the blade and the annulus casing. To introduce a tip gap to the blade model, cuts were made to the solid blade model's tip. The final rotor blade model had a tip gap of 0.12984 mm (5.1118×10^{-3} in). In the actual transonic compressor rig, rotor blade tip gaps between 0.1524 mm (0.006 inches) and 0.3556 mm (0.014 in) have been measured. These tip gap distances were measured when the rotor is stationary and cold. Tip gap distances during operations were much reduced.

Appendix B contains a modal analysis of the final blade model compared to actual violin bow testing on the rotor blades with a microphone-amplifier-spectrum analyzer by O'Brien. The closeness of the modal analysis to the actual modal

frequencies shows the fidelity of the final rotor blade model. Figure 9 displays the final blade model with the eleven blade profiles visible.

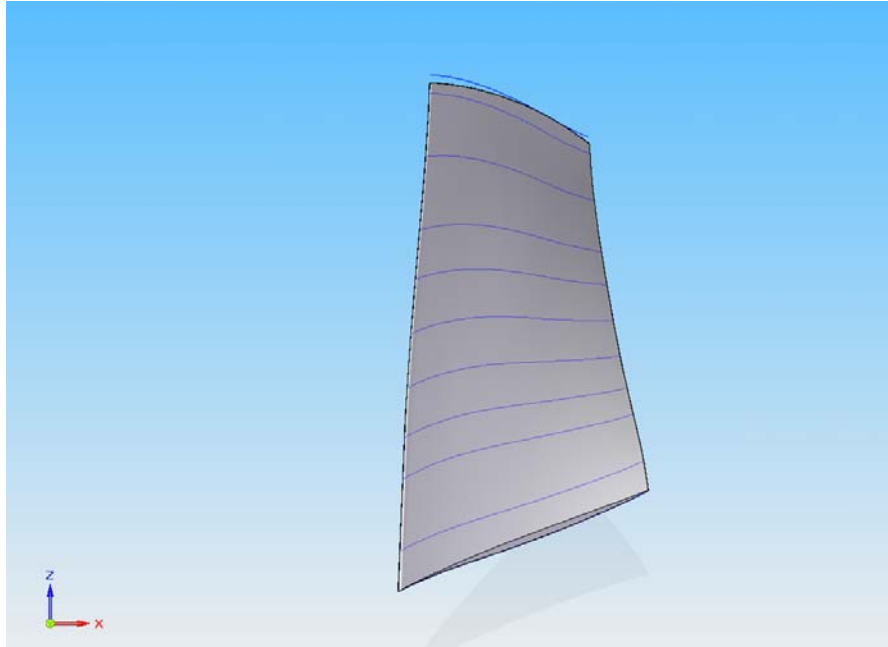


Figure 9. Final Rotor Blade Model with Profiles Shown

To combine the annulus and rotor models into a complete single rotor blade passage model, the geometries of each model were exported from the solid modeling program Solid Edge and loaded into the analysis package ANSYS Workbench. In the final model, the blade was exported as an IGES file and the annulus was exported as a STP file. The blade solid model was subtracted from the annulus solid model, which created the completed single rotor blade passage. Figures 10 through 14 show this model with the periodic boundaries, inlet, outlet, rotor blade and hub, and outer casing surfaces displayed.

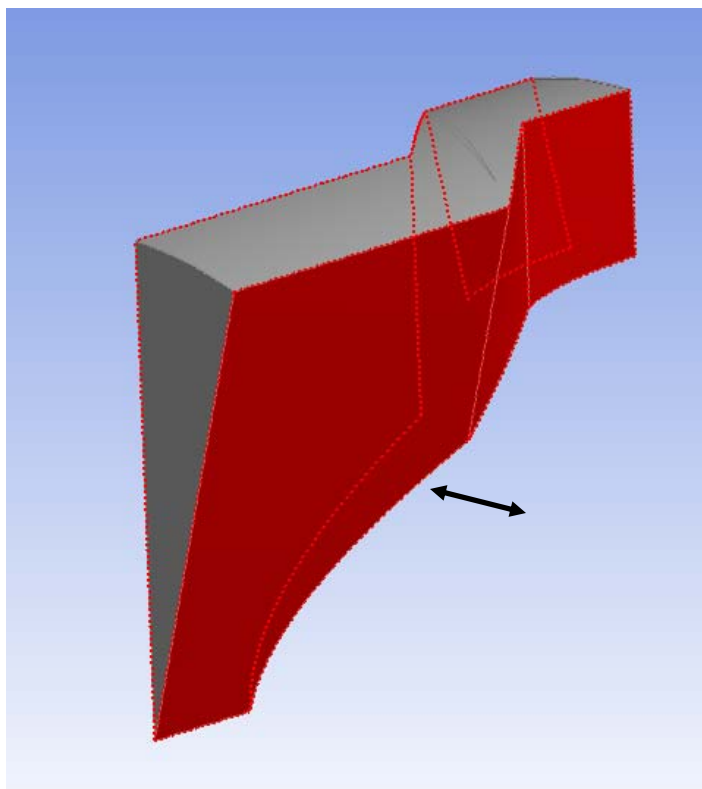


Figure 10. Periodic Boundaries

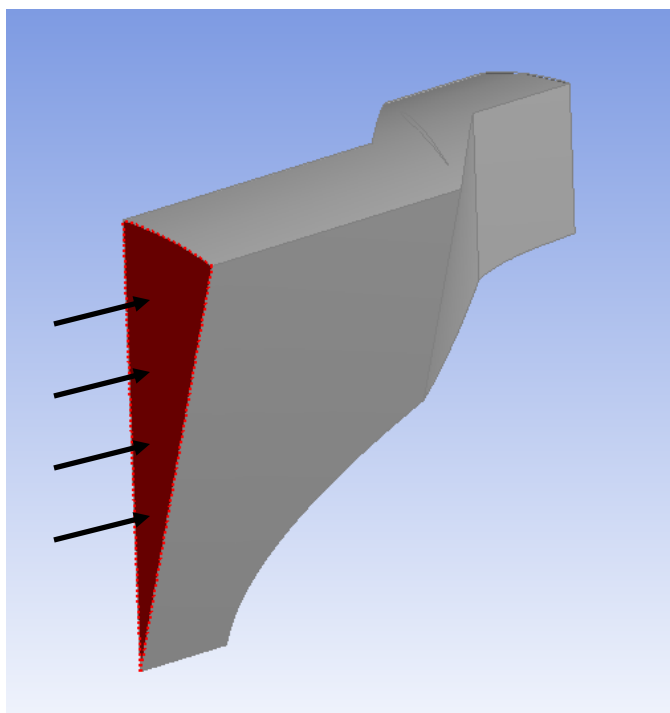


Figure 11. Inlet Boundary

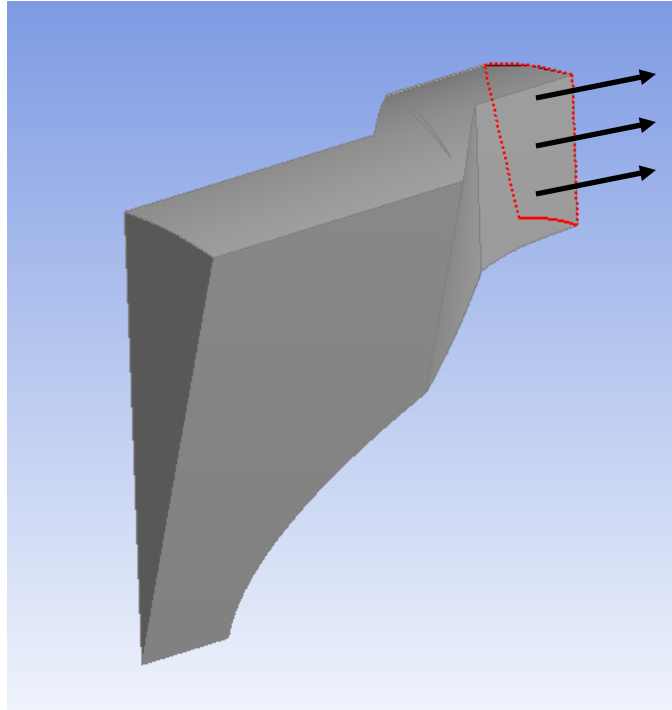


Figure 12. Outlet Boundary

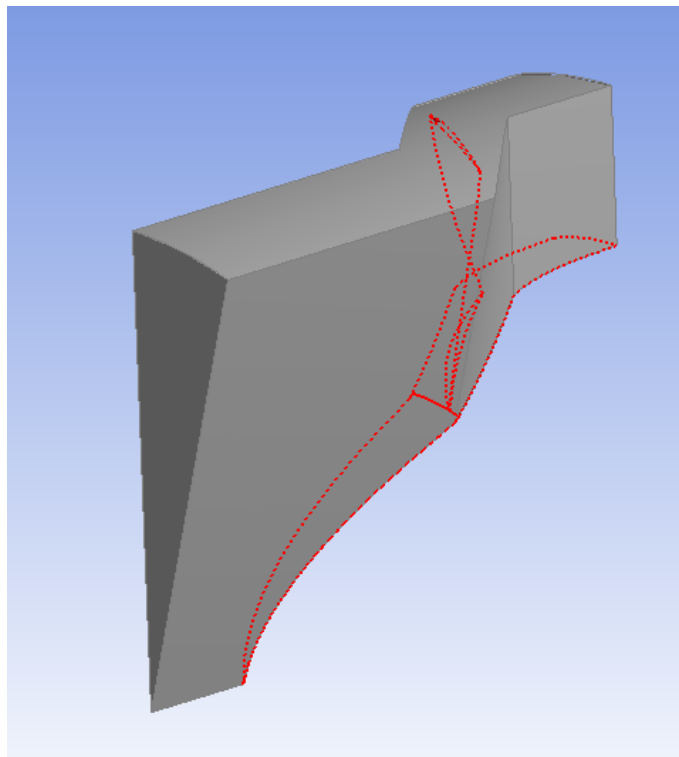


Figure 13. Rotor Blade and Hub Boundary

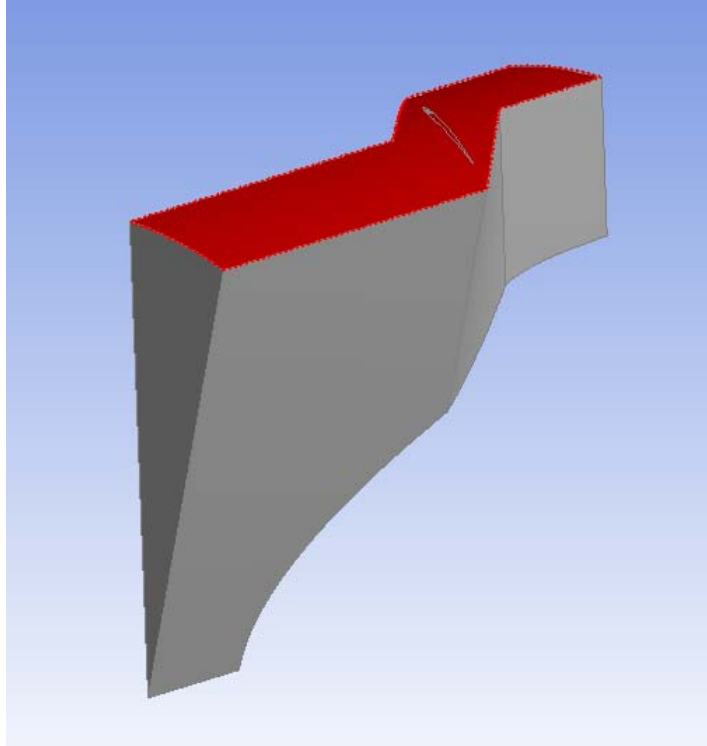


Figure 14. Outer Casing Boundary

The unstructured grid of the rotor passage computational model was created using the CFX mesh model within ANSYS Workbench. To develop a stable model, an iterative process was used to create the computational grid. This iterative grid process is detailed in Appendix C.

The final grid iteration used an eleven profile blade file, narrowed the tip gap, and refined the mesh on the hub nose. The more refined rotor blade model was exported from Solid Works as an IGES file. Like the previous grid, the annulus remained an STP file. A tip gap of 0.12984 mm (5.1118×10^{-3} in) was present in this model. This tip gap more closely matched the actual tip gap in the transonic compressor rig. Surface detection was also turned on and at least four elements were placed between each surface. Like the previous grid, this grid had five layers of inflation boundaries with a maximum thickness of 8.8 mm (0.3465 in) on the outer casing and the rotor blade and hub boundaries. The correct periodic boundary meshing remained from the previous model.

In order to refine the hub nose, the angular resolution on the hub nose surface was reduced from 30 degrees to 5 degrees. Figure 15 shows the surface grid of the previous hub nose and this model's hub nose.

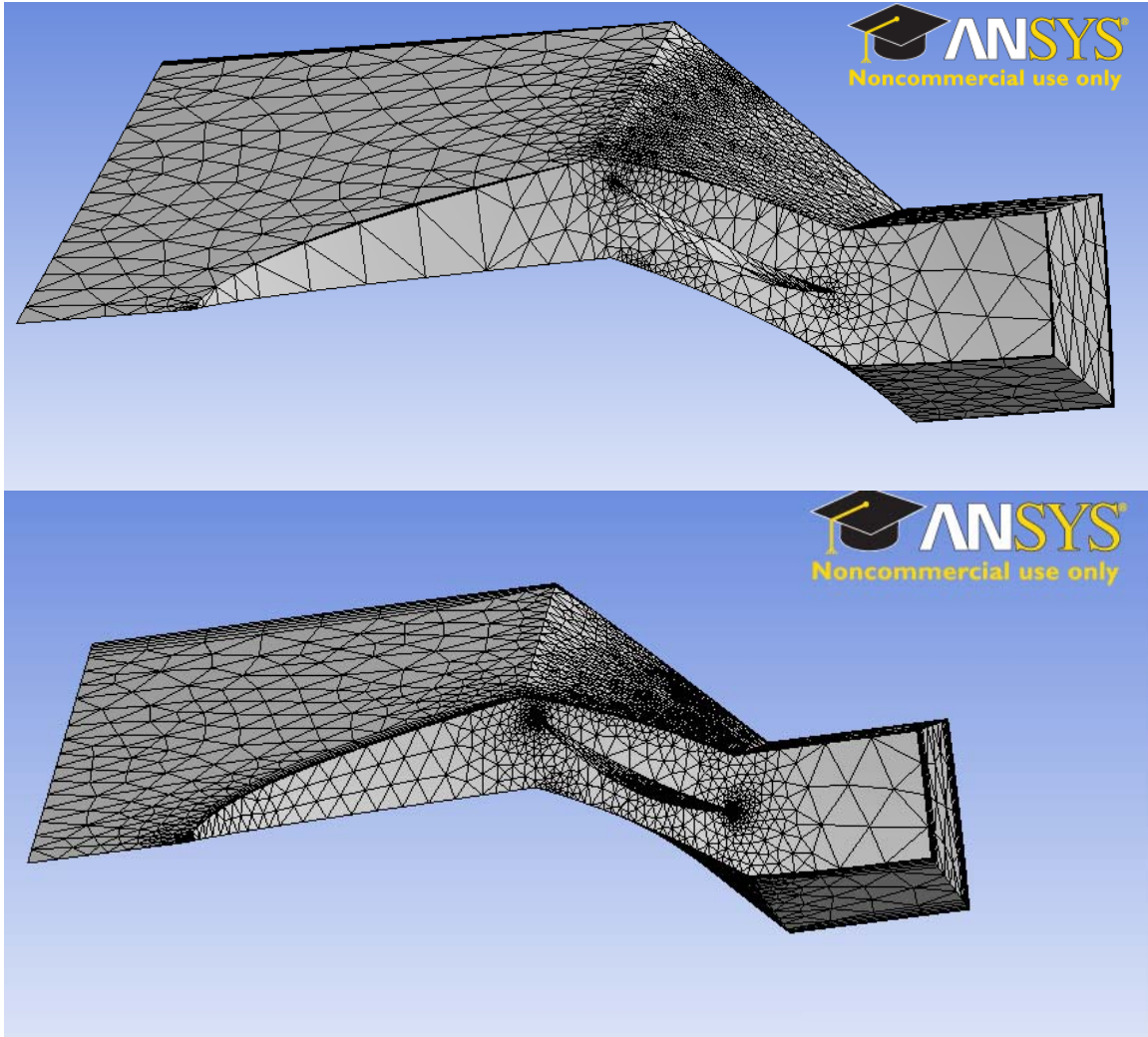


Figure 15. Surface Grid on the Hub Nose Before and After Refinement

The complete listing of meshing options chosen for this grid can be found in Appendix D. This computational grid forms the preliminary grid for the steady state, quasi steady state, and steam ingestion simulations. Table 1 shows a comparison of each iteration's mesh elements. The final grid is shown in Figure 16 with all the boundary surfaces highlighted with various arrow configurations.

Grid Iteration	Elements	Nodes	Tetrahedra	Pyramids	Prisms
1	66,337	15,989	66,337	0	0
2	230,288	44,849	224,929	1,031	4,328
3	817,314	189,311	706,720	1,722	108,872

Table 1. Geometry Comparison of Grid Iterations

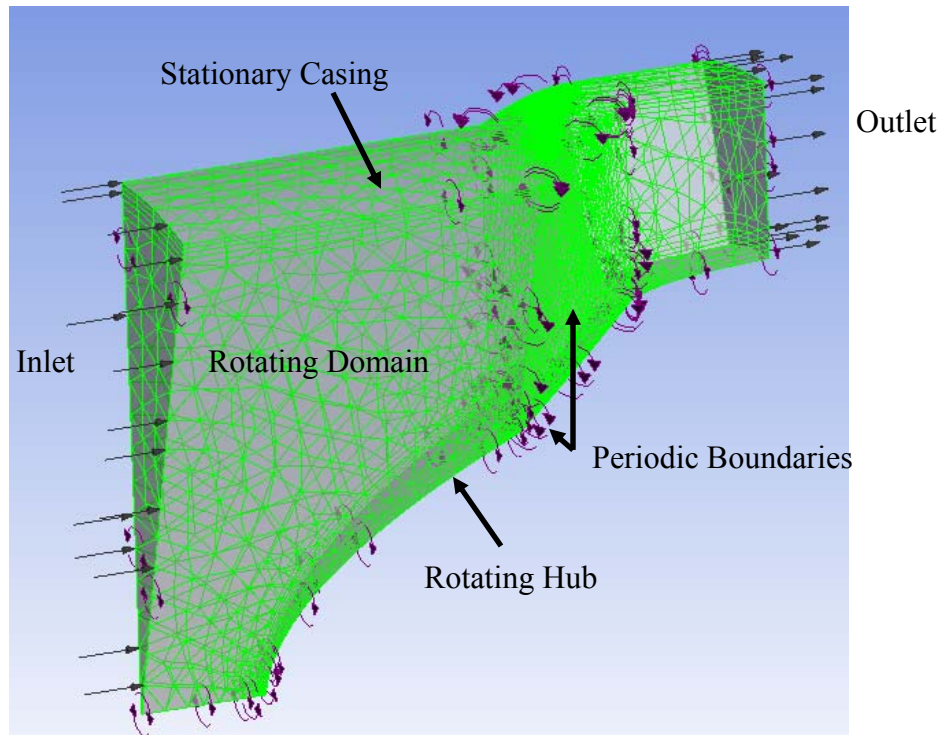


Figure 16. Final Computational Grid

THIS PAGE INTENTIONALLY LEFT BLANK

IV. STEADY-STATE ANALYSIS

All simulations, both steady-state and quasi-steady-state, were conducted using ANSYS CFX. CFX is a commercial computational fluid dynamics (CFD) program that uses an implicit code to solve the momentum and heat transfer equations. Before testing quasi-steady-state steam induction into the rotor passage, a battery of single gas steady-state simulations was conducted. This steady-state analysis was composed of three phases: computational grid iteration testing, refined computational grid experimentation, and final steady-state simulation result generation.

A. COMPUTATIONAL GRID ITERATION TESTING

The goal of computational grid iteration testing was to ensure that each iteration of the computational grid produced grid independent solutions. Once a computational grid iteration was proven stable, refinements and corrections were added until the final computational grid was created. All simulations were conducted at 100% design speed, 27,085 RPM, by using a rotating domain. Air ideal gas was chosen as the domain fluid and k-epsilon was selected for turbulence modeling. The outer casing was set as a smooth, adiabatic, counter rotating wall with no slip, and the rotor blade and hub boundary was set as a smooth, adiabatic wall with no slip. The periodic boundaries were set using rotational periodicity about the x-axis. The inlet was specified to have 0 Pa (0 atm) stationary frame total pressure and 293.15 K (527.67 °R) stationary frame total temperature. The outlet was set to have a static pressure. This outlet static pressure was changed for different simulations to simulate throttling of the compressor. Raising the outlet static pressure decreased the mass flow rate, while setting the pressure to 0 Pa (0 atm) simulated an open throttle run. Throttling by setting a back pressure was found to produce more stable simulations than throttling by setting an inlet mass flow rate. Throttling this way was also more realistic because it mimicked the physical experimental throttling technique. These boundary conditions represent the default setup for all the simulations in this study.

The first grid iteration, no-tip-gap, was tested for stability at various back pressures using root mean squared convergence criteria with a residual target of 1×10^{-4} . Basic compressor maps of these trials and experimental 100% speed data can be found in Figures 17 and 18.

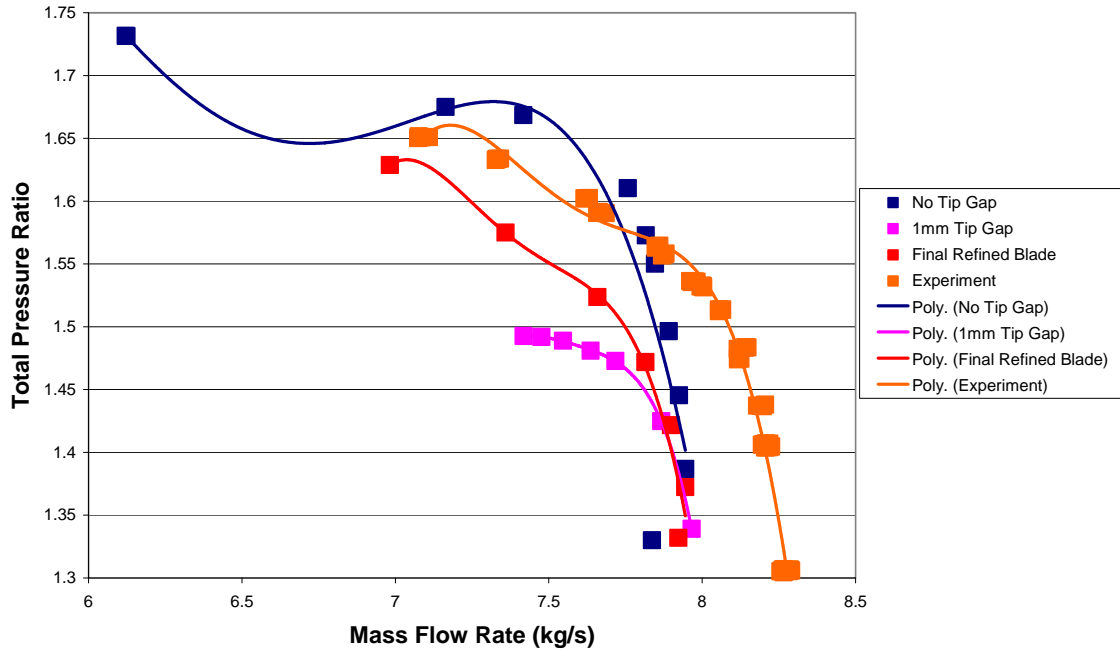


Figure 17. 100% Speed Grid Iteration Total Pressure Ratio vs. Mass Flow Rate Compressor Map

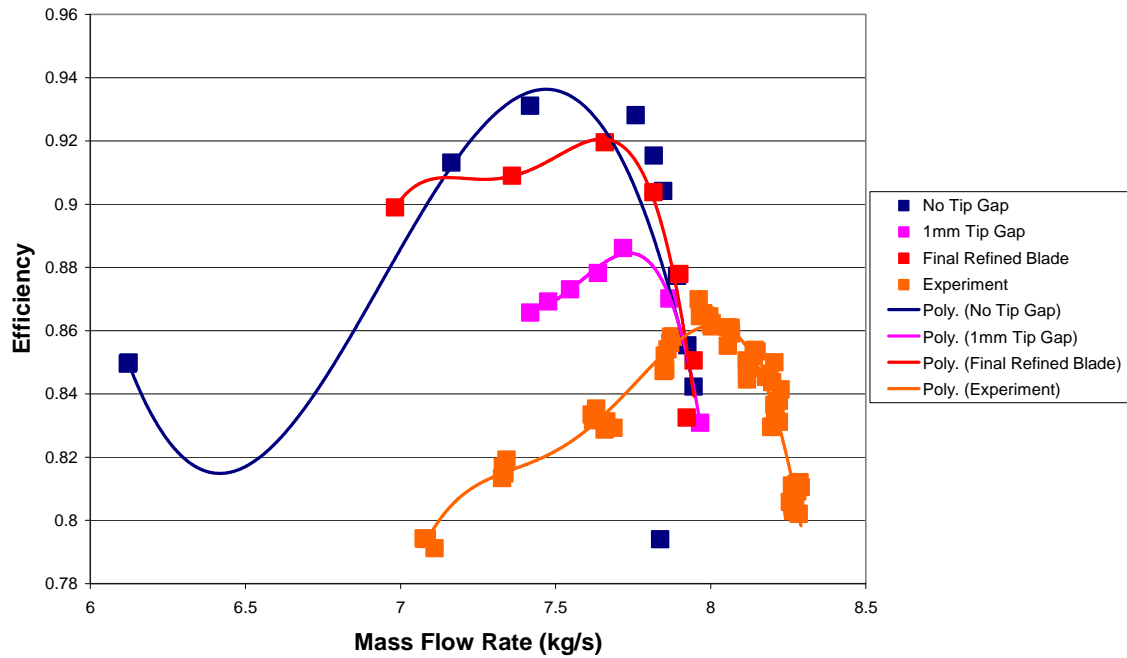


Figure 18. 100% Speed Grid Iteration Total to Total Isentropic Efficiency vs. Mass Flow Rate Compressor Map

With the first grid iteration having been proven stable, the second iteration, 1.00 mm (0.03937 in) tip gap, was created and tested. Using the same boundary conditions and simulation settings, the second grid iteration was tested at various back pressures. After demonstrating the stability of the second iteration, the final computational grid, eleven profile rotor blade and 0.12984 mm (5.1118×10^{-3} in) tip gap, was formed. This grid was also tested and found to be stable under the same conditions as the previous iterations. The completion of the final computational grid's stability testing ended the computational grid iteration testing phase.

B. REFINED COMPUTATIONAL GRID EXPERIMENTATION

In the Refined Computational Grid Experimentation phase, various changes to the solver settings were made in order to find an optimal procedure for generating steady-state simulation results. Different forms of mesh adaptation, convergence criteria, and turbulence modeling were used to determine which settings produce the most stable, accurate, and quickly converging steady-state simulations.

Mesh adaptation was accomplished in CFX by inserting mesh refinement into the solver settings. Mesh adaptation modified the existing computational grid based on one or many chosen parameters after a selected level of convergence had been reached. The process coarsened parts of the mesh with little change and refined parts of the mesh with large changes. Mesh adaptation accomplished this modification by adding and subtracting nodes from the computational grid. Mesh adaptation did not coarsen beyond the original mesh coarseness. By adding and subtracting nodes, higher mesh resolution was obtained while increasing computational efficiency; the solver had fewer nodes to solve around areas of little change in the selected parameter and more nodes around areas of greater change in the selected parameter. One solution run could have multiple mesh adaptations set to further refine the computational grid. After each mesh adaptation, CFX restarted the solution process using the newly generated mesh. Mesh adaptation could not add extra levels to the inflation boundary layers, but rather it added and subtracted nodes within the plane of each layer. Because mesh adaptation did not change the initial models' number of inflation layers, it did not correct the model's low y^+ resolution.

Three steps of mesh adaptation around absolute pressure were tested during this phase. Shock behavior and placement are crucial for determining the performance of the rotor, so obtaining high grid resolution around the shocks was sought. Across shocks large pressure differences occur. By setting mesh adaptation to refine around absolute pressure; these large shock pressure differences received more nodes. More nodes about the shocks increased the shock resolution and reduced shock smearing. Table 2 displays the computational grid differences between the initial model and the model after undergoing three steps of mesh adaptation. Since mesh adaptation increased shock resolution and solver efficiency without destabilizing the model, it was included in the final phase of steady-state simulations.

Model	Nodes	Elements	Tetrahedra	Wedges	Pyramids
Initial Mesh	189,311	817,314	706,720	108,872	1,722
After Mesh Refinement	384,882	1,407,855	1,064,801	340,980	2,074

Table 2. Comparison of Initial Mesh and Mesh after Three Steps of Adaptation

Initially root mean squared residual (RMS) convergence criteria was used in the steady-state simulations, but the maximum residual (MAX) convergence criteria was also tested. RMS convergence was set to 1.0×10^{-5} , which is considered good convergence, and MAX convergence was set to 1.0×10^{-4} , also considered good convergence. Using the MAX convergence criteria decreased the stability of simulations. Certain simulations that converged while using RMS did not when using MAX. This instability may have been caused by a region of unstable flow. During certain MAX simulations, the solver would converge for the first two mesh adaptations, but would not converge after the third. The mesh adaptations may have been refining the grid around an unstable portion of the flow. As this unstable region became more refined, the MAX solver could not reach a solution for this flow region. In order to more fully investigate this inability to converge, the locations of high mesh refinement should be examined. The solutions after each individual mesh refinement were not saved so this investigation was not conducted in this study. Figure 19 shows the maximum residual plots of a RMS convergent run and a MAX convergent run under the same boundary conditions. The RMS run produced tighter convergence. When both methods reached solutions, similar results were produced. Since RMS convergence reached solutions more reliably than MAX convergence, RMS convergence was chosen for use in the final phase.

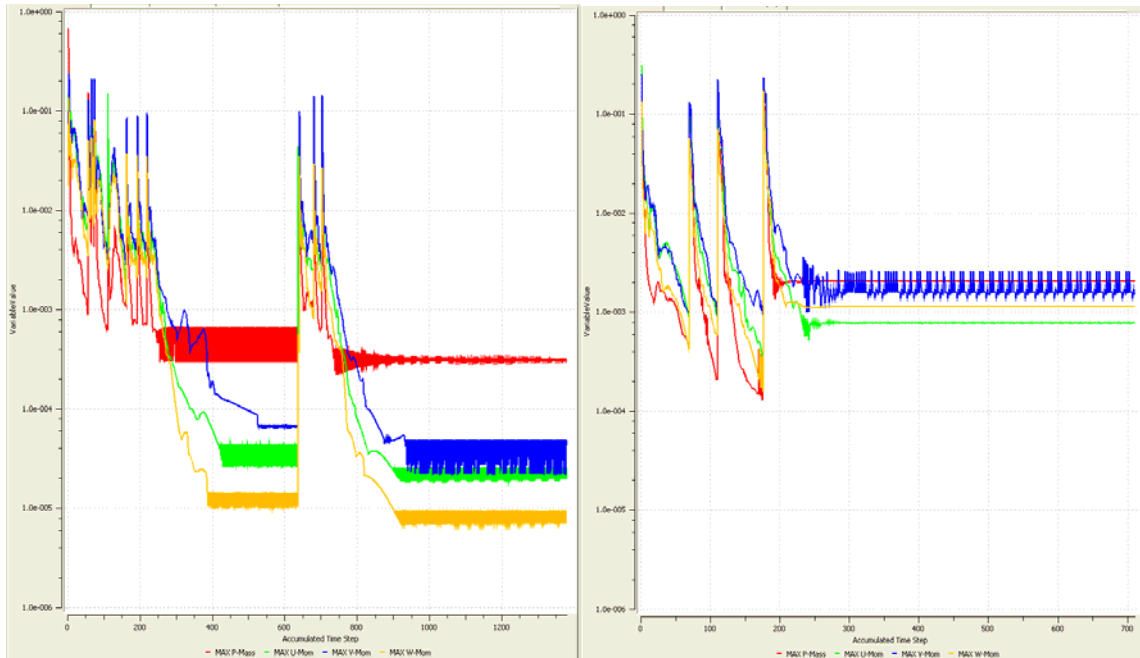


Figure 19. Maximum Residuals from RMS Convergent Simulation (left) and MAX Convergent Simulation (right)

In an attempt to improve the accuracy of the steady-state simulations, alternate turbulence models were tested. In order to include transition from laminar to turbulent flow, the shear stress transport turbulence model was used with a gamma theta transitional turbulence model. These SST simulations proved much less stable than the k-epsilon simulations: the SST simulations often would not converge when given boundary conditions that produced convergence with the k-epsilon model. The eddy viscosity transport equation option of turbulence modeling was also tested. Like the SST simulations, the eddy viscosity simulations were less stable than the k-epsilon simulations. When the eddy viscosity simulations did converge, they gave nonsensical results, such as total to total isentropic efficiencies greater than one or exceedingly high total pressure ratios. The eddy viscosity simulations took much longer to converge than the k-epsilon simulations; one eddy viscosity simulation took over four days to converge whereas the k-epsilon simulation with the same boundary conditions converged in less than four hours. The poor y^+ resolution of the computational grid may have caused the convergence and accuracy problems of the alternate turbulence model simulations. The computational grid had a y^+ resolution greater than one, and a y^+ resolution of at least

one is recommended for good results with these turbulence models. Mesh adaptation about y^+ was used during the simulations to increase the y^+ resolution, but even with mesh adaptation the smallest y^+ present on the model was greater than one. Also, the mesh adaptation about y^+ may have been coarsening the grid about the shocks, as it attempted to refine the y^+ resolution. This coarsening about the shocks would have decreased the accuracy of the simulations. Creating a much finer initial computational grid, with more and smaller inflation boundaries may solve these difficulties with alternate turbulence models, but the computational cost of the simulations would increase. Because of its computational inexpensiveness and its reliable convergence behavior, the k-epsilon turbulence model was used in the final phase of steady-state simulations.

C. FINAL STEADY-STATE SIMULATION RESULT GENERATION

The final phase of steady-state simulations was used to create total pressure ratio vs. mass flow rate and total to total isentropic efficiency vs. mass flow rate compressor maps, and initial values for the quasi-steady-state simulations. These simulations used three steps of mesh adaptation using absolute pressure as the refinement criteria, 1.0×10^{-5} RMS convergence, and the k-epsilon turbulence model. Simulations were conducted at 95% and 100% rotor speeds, 27,085 RPM and 25,730.8 RPM, respectively.

A mixture of two fluids, air ideal gas and water ideal gas, was selected as the domain fluid, but the mass fraction of air was set to one. A mixture must be chosen so that the steady-state simulations could be used as initial values for the quasi-steady-state simulations. The quasi-steady-state simulations used a mixture of air ideal gas and water ideal gas to simulate steam ingestion and CFX required that the domain fluids of the initial conditions and the quasi-steady-state simulations match. Because the mass fraction of air ideal gas was set to one, only air was present in the steady-state simulations. To reduce shock smearing the Max Continuity Loops option in Expert Parameters was set to two and Compressibility Control and High Speed Numerics were turned on under Solver Control. Appendix E lists the solver option settings of a typical simulation.

To generate the compressor maps, a simulation was first conducted with the outlet pressure equal to zero. The outlet pressure was then raised for the next simulation. Raising the outlet pressure reduced the mass flow rate which simulated a closing throttle. Each successive simulation used the previous simulation's final computational grid and solution as its initial computational grid and initial values. During post-processing, the compressor performance macro and mass flow function tools of CFX were used to find the total pressure ratio, total to total isentropic efficiency, and mass flow rate of each simulation. The mass flow rate was multiplied by 22 to get the total mass flow rate through the compressor. These simulations set the compressor inlet temperature at 293.15 K (527.67 °R), which is three degrees higher than the reference temperature of 288.15 K (518.67 °R). To normalize the simulation results, the mass flow rate was corrected using the following relationship given by O'Brien [7]

$$\dot{m}_{ref} = \dot{m} \frac{\sqrt{\theta}}{\delta}$$

where $\theta = \frac{T}{T_{ref}}$ and $\delta = \frac{p}{p_{ref}}$. $\theta = 1.0174$ and $\delta = 1$ for the simulations since the pressures were identical between the reference and the simulations.

V. QUASI-STEADY-STATE ANALYSIS

Whereas the goal of the steady-state simulations was to develop compressor maps for 95% and 100% speeds, the goal of the quasi-steady-state simulations was to determine the location of throttle stall and steam-induced stall on those compressor maps and to observe compressor and flow behaviors prior to stall events. Because both stall events are highly unsteady, a steady-state simulation would not accurately capture them. Though the steady-state simulations are not adequate, fully transient simulations of the stall events would be computationally expensive and therefore time consuming. A quasi-steady-state simulation method was developed to allow the propagation of the stall events' unsteady features while mitigating computational costs. The quasi-steady-state method used CFX's transient simulation settings with large time steps, many coefficient loops, and initial values from steady-state simulation solutions. For these simulations, time steps occurred every ten rotor revolutions. Assigning ten rotor revolutions between time steps simplified simulation post processing. Since the model's domain rotates, having an integer number of rotations per time step ensured that the model is in the same location at every time step. By fixing the model in space, quick comparisons of flow characteristics between time steps could be made. A ten revolution time step also allowed for a simulation to be conducted in a moderate amount of time. A maximum of 100 coefficient loops per time step was assigned. RMS residual convergence with a target of 1×10^{-4} was used for the coefficient loops. Since CFX used an implicit solver, the simulation remained stable even with these large time steps. By using many coefficient loops, each time step acted like its own steady-state simulation. The previous time step solution provided initial values for the next time step steady-state simulation, and the boundary conditions were controlled in the simulation options. Since the previous time step affected the current time step, unsteady flow features remained in the simulation. This series of linked steady-state simulations captured unsteady effects and was relatively inexpensive computationally.

For quasi-steady-state simulations, a failure of a time step's coefficient loop to converge within 100 iterations indicated stall. To ensure that the simulation was in a stall mode and not just reaching convergence on the 100th iteration, a second 100 iteration time step was completed before terminating the simulation. If a quasi-steady-state run completed without having a 100 iteration time step, no stall had occurred in that simulation. Non-stalling simulations normally reached convergence between time steps in fewer than 10 coefficient loops.

A. THROTTLE QUASI-STEADY-STATE SIMULATIONS

Steady-state simulations cannot accurately predict the location of throttle stall on the compressor maps, because the steady-state simulations damp out the unsteady regions of the flow. This forced stability resulted in compressor map points that extended far beyond the physical throttle stall points. In order to model the flow's instability at near stall points, quasi-steady-state simulations were conducted. These simulations produced more realistic throttle stall points.

Throttle stall simulations were conducted by choosing a likely compressor map point, and its steady-state simulation solution was used as an initial value for a quasi-steady-state run. The quasi-steady-state simulation's boundary conditions matched the steady-state simulation's boundary conditions. These simulations had a time step every ten rotor revolutions and the entire simulation lasted for four seconds. To implement these time step settings, the Simulation Type options are set to have 172 time steps of 0.0233184 seconds for 95% speed and 181 time steps of 0.0221525 seconds for 100% speed. Though these time steps seemed small, they were actually quite large and the RMS Courant number quickly exceeded a thousand. This large Courant number would be problematic in a fully transient simulation, but in quasi-steady-state simulation the large Courant number was anticipated. Appendix F gives a complete list of options set for the throttle stall simulations.

If stall occurred during a simulation, the next highest mass flow rate point was tested. If stall did not occur during that higher mass flow rate simulation, the throttle stall point was set at the initial point. If stall did not occur during the initial simulation the next lowest mass flow point was tested. This process was repeated until stall occurred during a simulation.

B. STEAM INGESTION STALL

Simulating steam ingestion during a quasi-steady-state simulation required that the inlet temperature and air ideal gas mass fraction boundary conditions change while the simulation ran. These inlet conditions were based on data collected from a previous steam ingestion experiment. This experiment occurred at 95% speed. 100% speed steam-induced stall had not been physically conducted because the event would highly stress the rotor. Because no 100% speed steam ingestion data exists, the 100% steam ingestion simulations were conducted with the 95% speed inlet transient data due to steam ingestion. The CFX expression language was utilized to model inlet temperature and air mass fraction. A series of step functions was written which generated a two-second steady inlet condition followed by a two-second ramp to maximum temperature and minimum air mass fraction, followed by another ramp function to initial conditions. The second ramp function lasted for ten seconds for temperature and seven seconds for air mass fraction. These temperature and mass fraction expressions were set as the inlet boundary conditions of the simulation. Figures 20 and 21 display the temperature and air mass fraction vs. time plot of the inlet expressions and an actual steam-induced stall event measured by Gannon et al. [8].

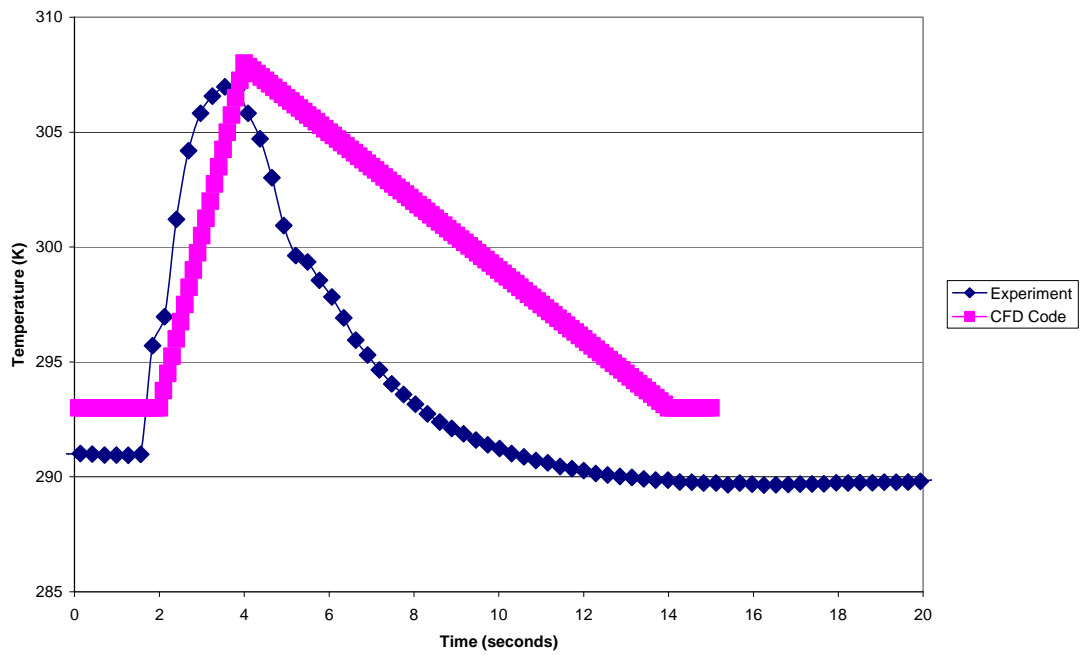


Figure 20. 95% Speed Experimental and CFD Inlet Temperature Plots

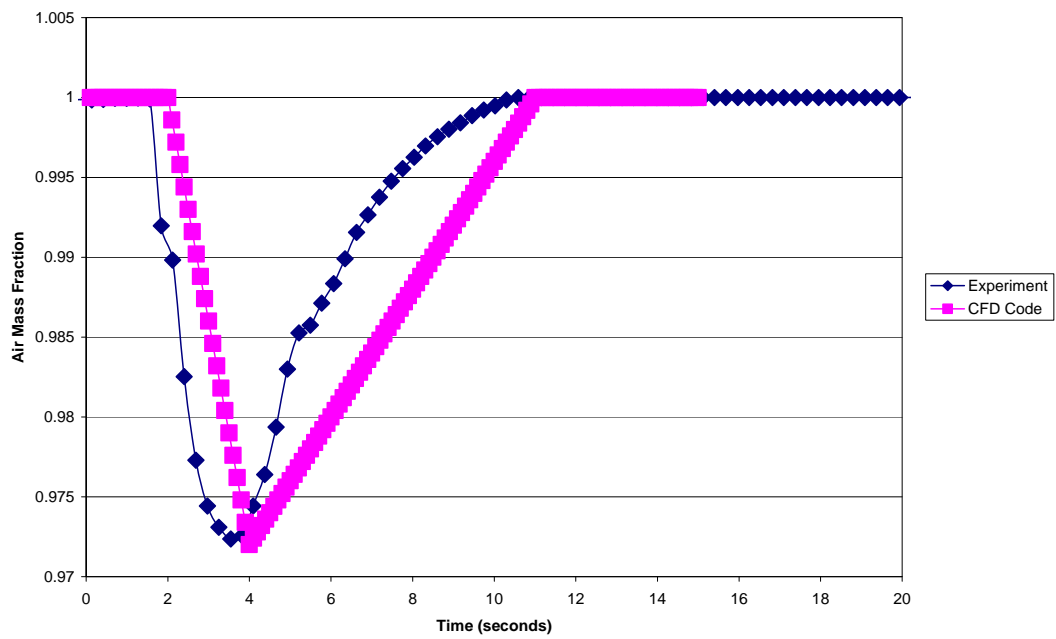


Figure 21. 95% Speed Experimental and CFD Air Mass Fraction Plots

The CFD Code temperature started at a slightly higher value of 293.15 K (527.67 °R) to match the steady-state simulation inlet boundary condition. It also had a maximum temperature 2 K (3.6 °R) higher than the experimental value. By increasing the maximum temperature value, both the CFD Code and Experimental temperatures had the same change in temperature. Appendix G lists the solver settings for steam ingestion simulations and the code for the inlet expressions.

A similar procedure to locating the throttle stall point was used to find the steam ingestion stall point. Likely locations were tested and then outlet pressure was raised or lowered to adjust the mass flow rate in order to find the point where steam ingestion stall first occurred. Like the throttle stall cases, the steam ingestion stall cases used the steady-state solutions as initial values. Once a steam ingestion stall point was located, a quasi-steady-state simulation at the same outlet pressure with constant inlet conditions was conducted. These simulations were carried out to verify that the steam ingestion modeling was the factor causing stall. All the steam ingestion stall points remained stable when tested with constant inlet conditions. Stall occurring during those constant inlet simulations would have indicated that the quasi-steady-state method is inherently unstable and therefore invalid.

In addition to finding the locations of steam ingestion stall, flow conditions were recorded after every five time steps of every quasi-steady-state steam ingestion simulation. By saving the flow data from these simulations, compressor and flow behaviors prior to stall can be observed. Because the lack of solver convergence indicates stall, compressor and flow behavior cannot be observed during or after a stall has occurred. The results just prior to stall behaviors are presented and discussed in Chapter VI.

After locating the steam-induced stall point at 95% speed, the initial ramp function was modified to investigate the effect of ramp function slope on steam-induced stall. These trials were conducted to determine whether ramp function steepness or final property magnitude had the greatest effect on steam-induced stall in the model. Ninety-five percent speed was chosen over 100% speed because the steam conditions used in the model were derived from a 95% speed physical experiment. Two new ramp functions

were generated: one took twice as long to reach maximum temperature and minimum air mass fraction, four seconds, and the other took half as long, one second. These new ramp function simulations were conducted at steam ingestion stall boundary conditions and boundary conditions one point before stall. Any change in stall behavior would indicate that ramp function steepness plays a role in steam-induced stall; whereas no change in stall behavior would indicate that the final property values are the prominent stall consideration. These simulations results indicated that steam function slope does not affect simulation steam-induced stall. Detailed results of these simulations are presented in Chapter VI.

VI. RESULTS AND DISCUSSION

By comparing the CFD and experimental results, the accuracy and relevance of the computational model could be evaluated. The physical experimental results are presented first, followed by the CFD results. The CFD results presentation and discussion is divided into overall performance trends, and individual simulation observations. In addition to presenting the physical and CFD data, a discussion is conducted on the influence of steam ingestion ramp function slope.

A. PHYSICAL EXPERIMENTAL COMPRESSOR MAPS

Figures 22 and 23 display the compressor maps for 70%, 80%, 90%, 95%, and 100% speeds generated during this study. These results are also tabulated in Appendix H. The throttle surge line and steam surge line are indicated on the figures. Green circles indicate throttle stall points, and red circles represent steam stall points.

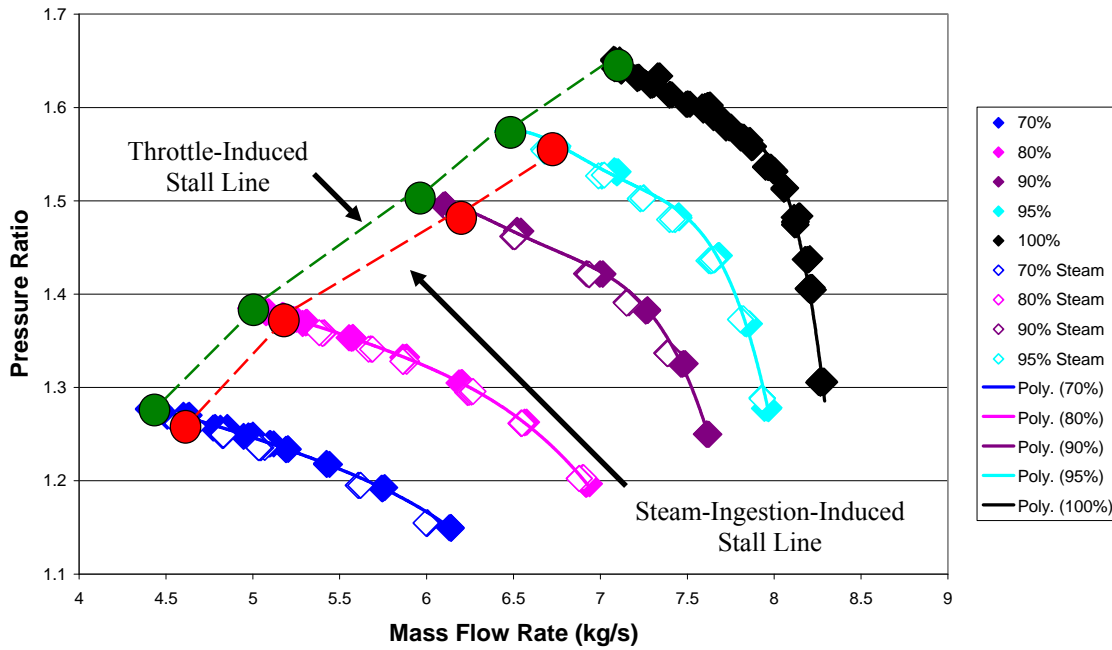


Figure 22. Pressure Ratio vs. Mass Flow Rate Compressor

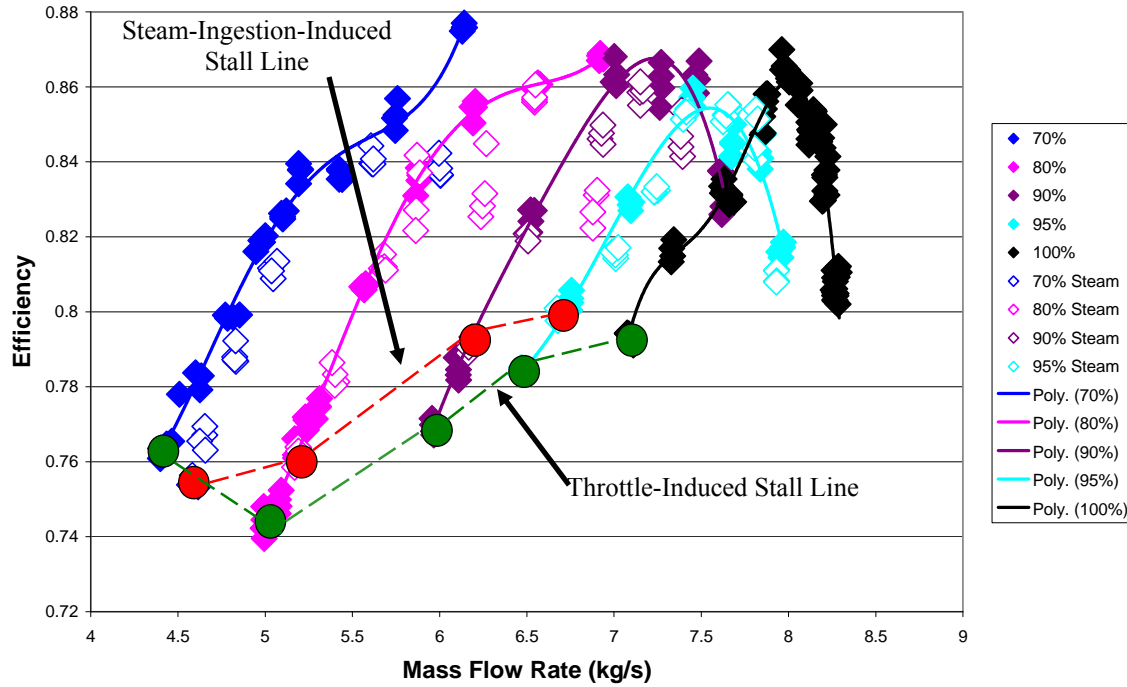


Figure 23. Efficiency vs. Mass Flow Rate Compressor Map

Differences in the efficiencies were observed between the throttle-induced stall data and the steam-induced stall data at high mass flow rates for 70% and 80% speeds. The throttle-induced stall data displayed higher efficiencies than the steam-induced stall data, though almost identical throttle settings were used for both tests. The lower efficiencies of the steam-induced stall data may be due to the rotor blades having a wider tip-gap than the initial tip gaps during the throttle-induced stall tests. The steam-induced stall trials were conducted after the entire set of throttle-induced stall trials. Because the rotor had stalled during these throttle-induced stall trials, the tip-gap was widened. So during the steam-induced stall trials the rotor had a wider tip-gap than during the throttle-induced stall trials. This wider tip-gap would lower the efficiency of the rotor. In future research, a steam-induced stall trial should be conducted directly following a throttle-induced stall trial at a specific speed. This method would enable more consistent tip gaps between steam-induced stall trials and throttle-induced stall trials.

The stall margin was calculated for each speed in both throttle-induced and steam-induced stall modes. By comparing the steam-induced stall and throttle-induced stall margins, the reduction in stall margin can be found for each speed line. Hill and Peterson [9] define the stall margin based on mass flow rate as

$$\text{Stall Margin} = \frac{(\dot{m}_{peak\ eff} - \dot{m}_{surge})}{\dot{m}_{peak\ eff}}$$

Table 3 displays these throttle and steam-induced stall margins and stall margin reductions.

	70% Speed	80% Speed	90% Speed	95% Speed	100% Speed
Throttle Stall Margin	0.2481	0.2375	0.1693	0.1331	0.1090
Steam Stall Margin	0.2196	0.2079	0.1396	0.1031	
Stall Margin Reduction	0.1149	0.1244	0.1754	0.2252	

Table 3. Experimental Throttle Stall Margin, Steam Stall Margin, and Stall Margin Reduction for 70%, 80%, 90%, 95%, and 100% Speeds

This table shows that as rotational speed increased stall margin reduction also increased. The table also shows that about a 3% decrease in stall margin exists between throttle and steam for all speeds. The peak efficiency mass flow rates were found by fitting 4th degree polynomial curves to the efficiency vs. mass flow rate data. The steam stall margin for 100% was not found, because no 100% speed steam-ingestion trials were conducted.

B. NEW STEAM INGESTION DATA

While conducting the 95% speed steam ingestion experiments, temperature data was taken using the new array of thermocouples preceding the rotor. Figure 24 displays a plot of temperature and rotational speed vs. time during a steam-induced stall. See Figure 4 for the probe layout.

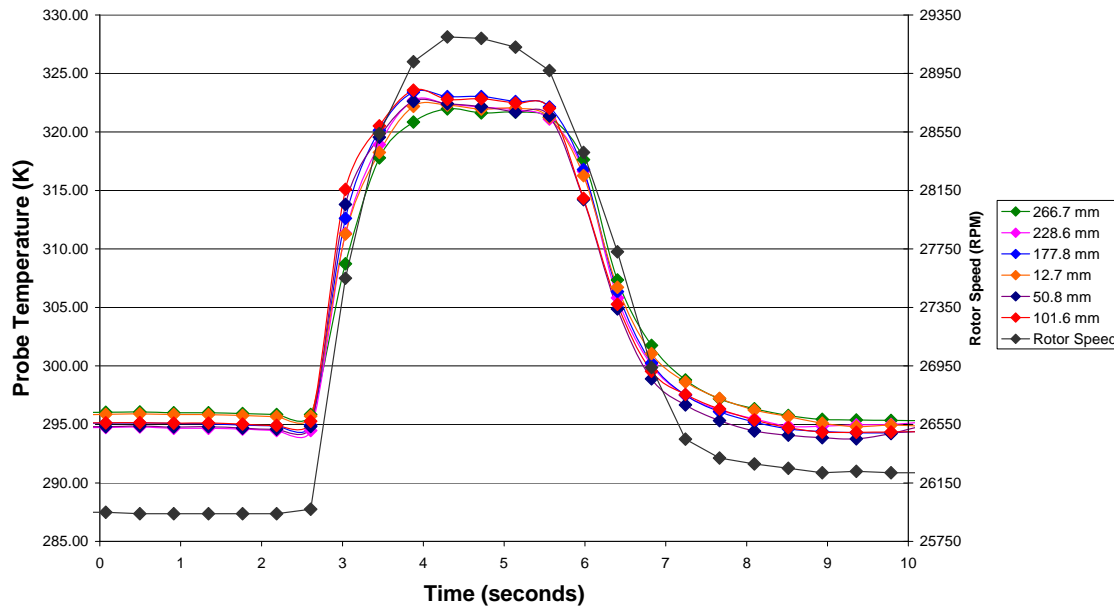


Figure 24. 95% Speed Physical Steam Ingestion Event Probe Temperature and Rotor Speed vs. Time Plot

This new temperature plot displays significant differences to the simulation steam ingestion function. The new plot reaches a higher temperature maximum, 324 K (583.2 °R), in less time, one second, than the previous experiments [8]. The new panel allowing more steam to be ingested into the inlet caused this faster ramp and higher maximum temperature. The mass fraction of air was not computed during these trials, but it should be investigated to confirm that more steam is entering the transonic compressor rig.

As steam was ingested into the physical rotor, the rotor rotational speed increased. The CFD simulations did not account for this acceleration. Because the CFD model's rotational speed remained constant during the modeling of the steam ingestion, its performance would be different than the experiment. The steam ingestion function and the rotor speed acceleration differences may contribute to the discrepancies in steam-induced stall locations on the compressor maps. Figure 25 shows the measured instantaneous temperature distribution vertically across the inlet during the 95% speed test. The red arrow indicates that steam entered the upper portion of the transonic compressor rig inlet.

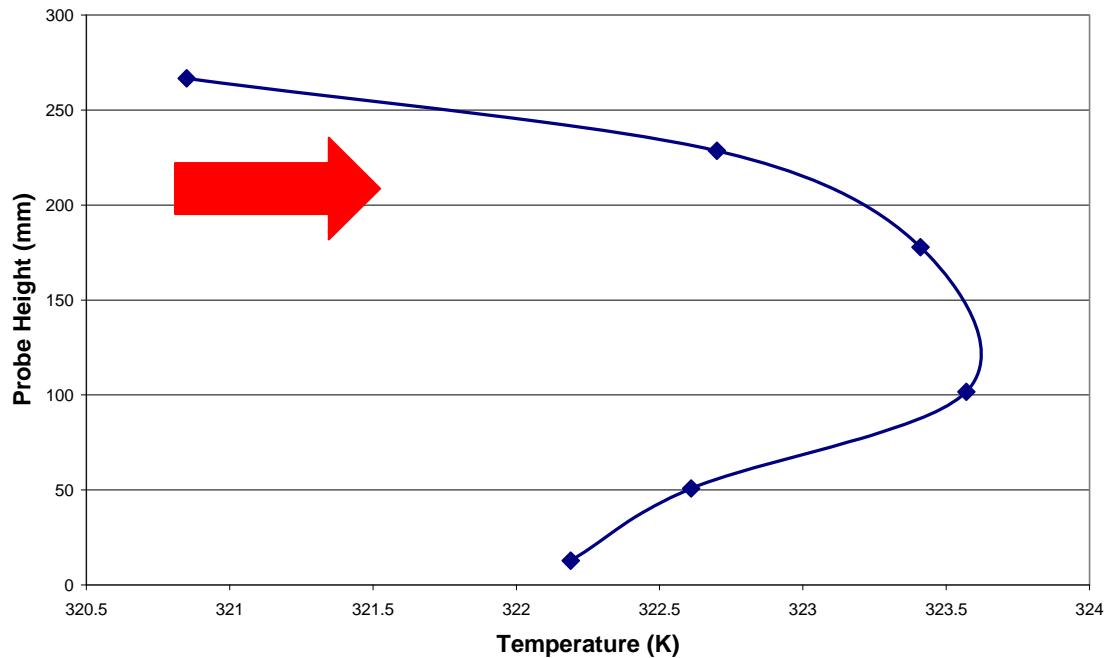


Figure 25. Spatial Temperature Distribution during 95% Speed Steam-Induced Stall

The temperature distribution had a maximum occurring near the center of the annulus, which indicates that a large amount of flow mixing occurred as the steam was ingested. The CFD simulations modeled uniform temperatures across the entire inlet at an instantaneous time. Though this discrepancy may contribute to simulation error, the physical temperature difference between the minimum and maximum were only around 2.5 degrees K (4.5 °R). This temperature difference may be small enough to be inconsequential. This plot indicates that the steam mixed rapidly with air within the inlet duct.

C. TRANSONIC COMPRESSOR RIG MODIFICATIONS

The initial flow separator design did not produce large enough spatial temperature gradients. Figure 26 displays the spatial temperature distribution at the temperature zenith of a steam ingestion event during a 70% speed experiment. The red arrow represents steam entering the lower section of the inlet. While the temperatures were not uniform, there was not a considerable difference between the lower and upper sections.

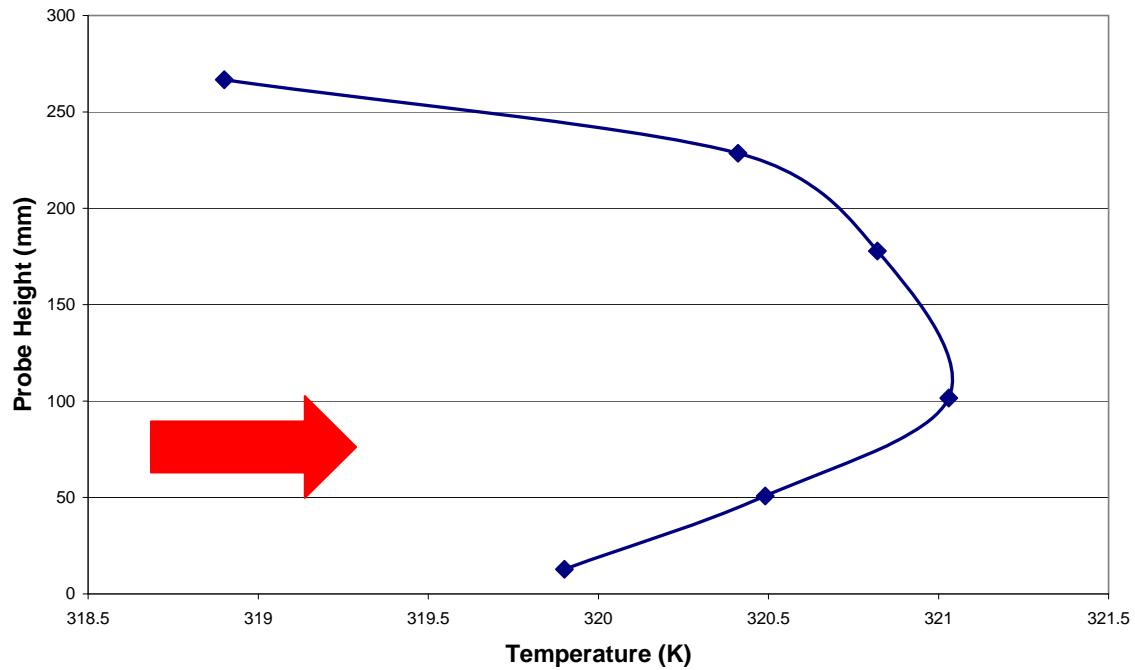


Figure 26. Probe Height vs. Temperature Plot at 70% Speed with Flow Separator

Too much steam was expelled from the inlet plenum during the solenoid valve activation which opened the steam pipe. In order to accelerate the flow at the point of steam injection, while not throttling the flow, a panel was placed over the inlet with two square openings that had the same combined area as the full open throttling holes. Figure 27 displays this panel on the transonic compressor rig inlet.



Figure 27. Panel Covering Inlet of Transonic Compressor Rig with Upper Section Steam Injection Pipe Location

The steam injector pipe was also modified to inject steam into the upper inlet section rather than the lower section. By injecting steam into the upper section, flow mixing due to buoyancy forces would be reduced. The panel and pipe location change did produce more complete steam ingestion, but they did not produce high temperature section differences. Figure 28 shows a spatial temperature plot at the temperature zenith of steam ingestion experiment at 90% speed.

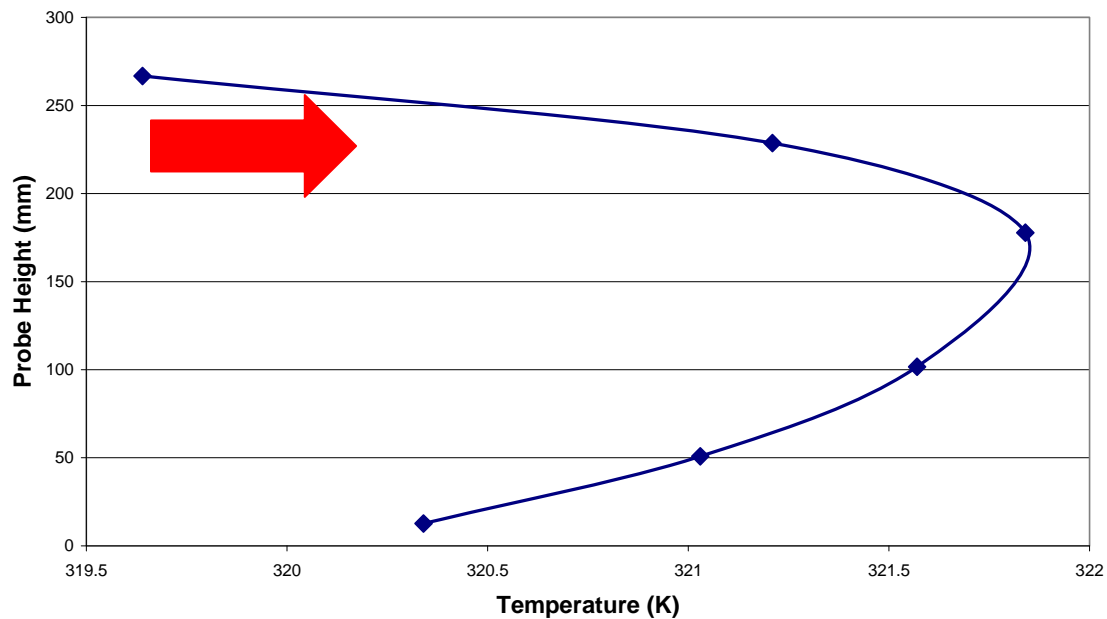


Figure 28. Probe Height vs. Temperature Plot at 90% Speed with Separator, Panel, and Steam Pipe Location Change

The red arrow represents steam entering the upper section of the inlet. This experiment had the separator, panel, and upper section steam injector. A large amount of flow mixing still occurred after the transonic compressor inlet, so modifications to the steam injector system at the inlet seemed to have little effect. If the inlet was shortened to a length comparable to an aircraft inlet, mixing may be reduced.

D. OVERALL CFD PERFORMANCE TRENDS

1. 95 Percent Speed

While discovering the 100% speed steam ingestion stall point, observations were made on the computational behavior of the onset of steam ingestion stall. If a stall occurred, it happened during the initial ramp function to the maximum temperature and minimum air mass fraction. Stall never occurred during the second ramp function back to initial conditions. Simulations were then conducted using only the constant inlet condition period followed by the initial ramp function period. Steam ingestion stall

occurred at the same location as before. Because of this behavior, the 95% speed steam ingestion simulations were shortened to four seconds instead of 14. Shortening the simulations reduced computational costs without affecting the simulation results.

Figures 29 and 30 show the compressor maps for both CFD simulations and physical experimentation at 95% speed.

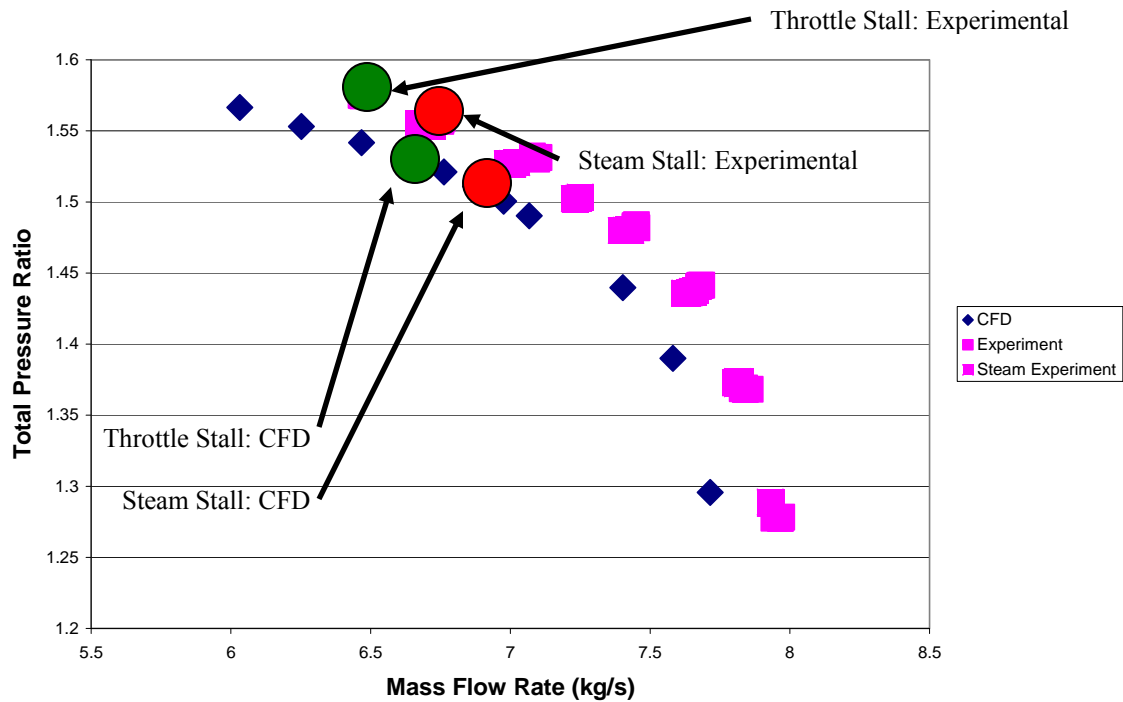


Figure 29. 95% Speed CFD and Physical Experiment Total Pressure Ratio vs. Mass Flow Rate Plot

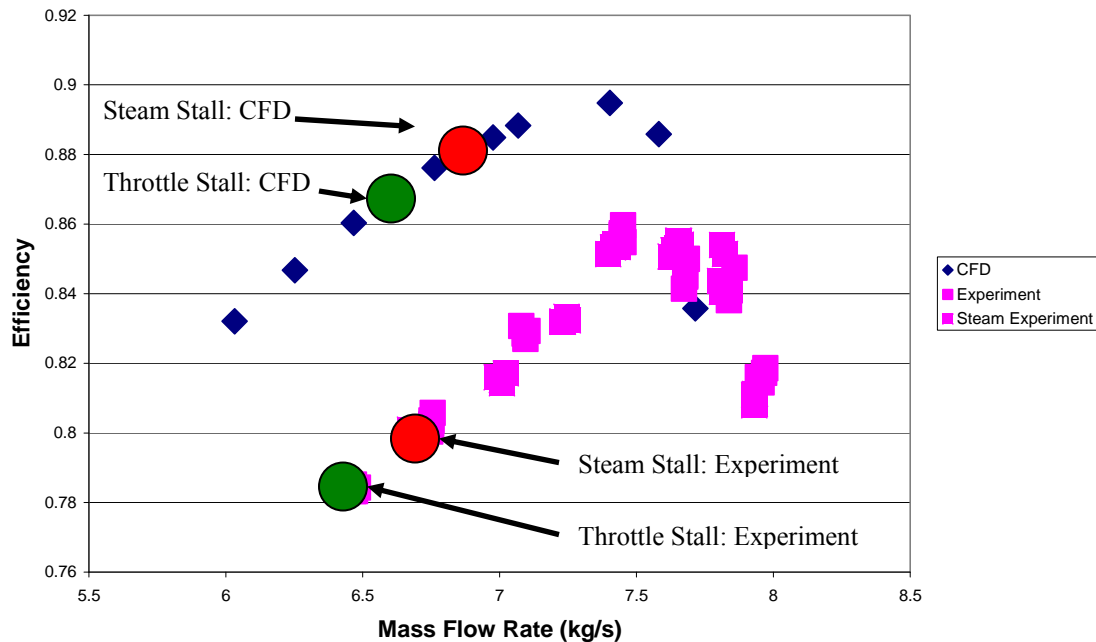


Figure 30. 95% Speed CFD and Physical Experiment Total to Total Isentropic Efficiency vs. Mass Flow Rate Plot

Throttle stall points are marked with green circles, and steam stall points are marked with red circles. The simulation results and the physical experimentation results did not exactly match, but many key similarities existed. Both CFD pressure and efficiency curves' shapes matched the physical experimentation curves' shapes. This shape matching indicates that the CFD model performed in a similar manner to the physical rotor. Though their shapes matched, the CFD model under predicted the mass flow rate and over predicted the efficiency through the rotor. The differences in mass flow rate may be a recurring discrepancy with the CFD program, or the CFD model's rotor blade shape may not have exactly matched the physical rotor blade during operations. When the rotor is run at speed, the rotor blades undergo an untwisting due to some heat but mainly due to centripetal forces. As the blades untwist to their so called 'hot' shapes, they allow for more mass flow. If the physical rotor blade was more untwisted than the CFD model blade, then the CFD simulations would under predict mass flow rate. The over prediction of efficiency through the rotor most likely occurred from the CFD

simulation not accurately modeling all the various losses through the physical rotor. Though the CFD model predicted much higher efficiencies than the experimental results, it did closely predict the point of maximum efficiency.

The stall points of the CFD model and the physical experimentation revealed significant trends. The throttle-induced stall points of the CFD simulations occurred with more mass flow rate than the physical experiment. This under prediction of the stall points may have been caused by the high Courant number of the quasi-steady-state simulations. In the 95% speed simulations the high Courant number may have amplified instabilities within the flow field causing earlier stall. This instability amplification may have overcome the various stabilizing forces, such as periodicity, acting upon the model. Though the stall points occurred earlier in the CFD simulations, the difference in mass flow rate between the throttle and steam-induced stall points of the CFD simulations and physical are close. Table 4 summarizes the stall margin comparisons between the CFD simulation and physical experiments. Both the CFD simulations and the physical experiments had similar stall margins and stall margin reductions. The simulation's prediction of around 3% stall margin difference between throttle and steam closely matched the physical experiment. This agreement in stall margin difference indicated that CFD can be used to estimate the location of steam-induced stall at 95% speed.

	Difference in Mass Flow Rate (kg/s)	Throttle- Induced Stall Margin	Steam- Induced Stall Margin	Difference in Stall Margin	Stall Margin Reduction
CFD Simulation	0.2549	0.1268	0.0932	0.0336	0.2650
Physical Experiment	0.2238	0.1331	0.1031	0.0300	0.2252

Table 4. 95% Speed Stall Margin Comparisons

2. 100 Percent Speed

Figures 31 and 32 display the compressor maps for both the CFD simulations and the physical experiments at 100% speed.

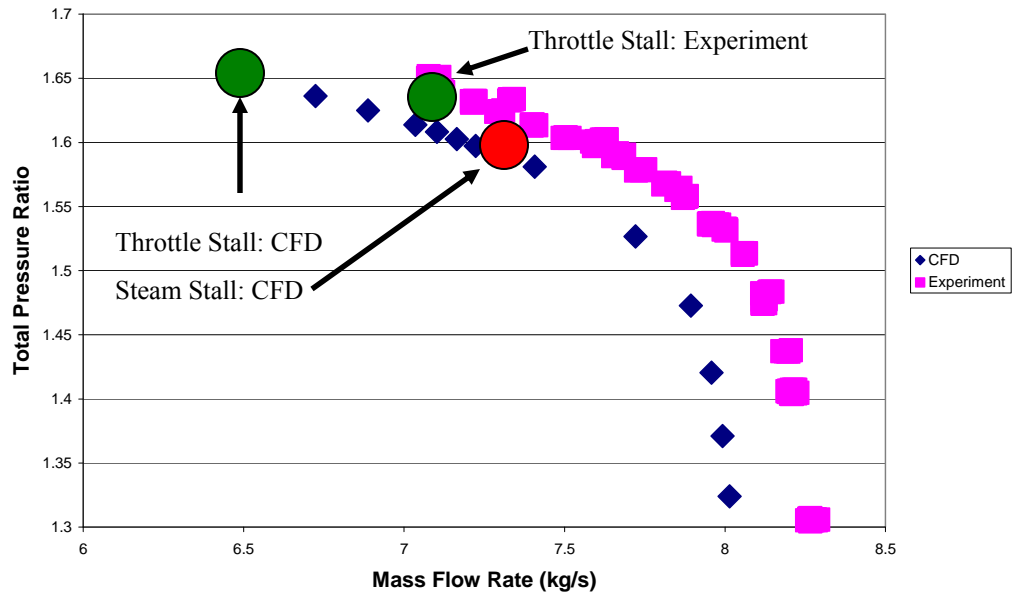


Figure 31. 100% Speed CFD and Physical Experiment Total Pressure Ratio vs. Mass Flow Rate Plot

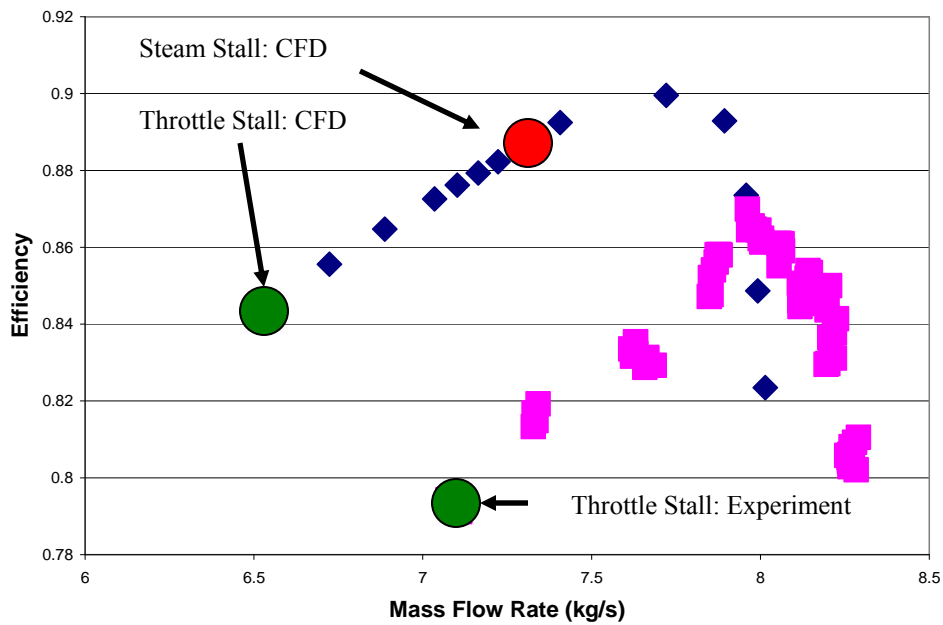


Figure 32. 100% Speed CFD and Physical Experiment Total to Total Isentropic Efficiency vs. Mass Flow Rate Plot

Like the 95% speed maps, throttle stall points are marked with green circles and steam stall points are marked with red circles. Similar trends occurred in the 100% speed results that occurred in the 95% results: the CFD simulations produced curves with matching shapes, but the CFD model under predicts mass flow rate and over predicts efficiency. These trends mostly likely occur for the same reasons discussed in the 95% speed results.

Considerable differences existed between the locations of 100% speed stall points and the 95% speed ones. Unlike the 95% speed simulations, the 100% speed simulations predicted throttle stall occurring with less mass flow rate than the physical experiment. This under prediction may be caused by less instability amplification occurring during 100% speed simulations. The rotor was designed with the aid of CFD programs to operate at 100% speed, thus the CFD model may be more computationally stable at 100% speed than at 95% speed. The model's unblemished blade shape, perfect axi-symmetric blade placement, and periodic boundary conditions may also increase the simulations' ability to operate with less mass flow rate than the physical rotor.

The physical steam-induced stall point was not found for 100% speed, so no comparison was made between it and the CFD prediction. Though the CFD model and experimental results were not compared, the differences between the steam-induced stall margin reductions of the 95% speed CFD model and 100% speed CFD model can be examined. The 95% speed CFD model had a stall margin reduction of 26.50% and the 100% speed CFD model had 66.88%. The 100% speed stall margin reduction is considerably larger than the 95% speed stall margin reduction. This increase in steam stall margin may have been caused by the functions used to model steam ingestion. Since no 100% speed steam ingestion trial has ever been conducted, there is no data regarding air mass fraction and mixture temperature at 100% speed. Because there was no data available, the 95% speed steam ingestion functions were also used for 100% speed simulations. Entirely different slopes, temperature maximums, and air mass fraction minimums may occur at 100% speed steam ingestion. 100% speed steam ingestion is expected to have a smaller mass fraction of steam than the 95% speed steam ingestion since a constant amount of steam is ingested regardless of rotor speed and 100% speed

trials have greater mass flow rates. If those correct values are used for the 100% speed steam ingestion modeling, the 100% speed steam-induced stall point may occur with a smaller mass flow rate. This smaller mass flow rate steam-induced stall point would produce a more reasonable stall margin reduction. Conversely, the stall reduction margin of 100% speed may indeed be as large as the CFD model indicates, but no physical testing occurred to verify its prediction.

3. The Effects of Periodicity

Since only one rotor blade passage was modeled, periodic boundary conditions were set on the passage's sides. These periodic boundary conditions introduced specific behavior into the computational fluid dynamic model that affected the performance of the simulations. Because the periodic boundary conditions forced identical fluid properties at the sides of the model, the simulations produced axis symmetric solutions. In these cases the simulations acted like every blade of the rotor had identical flow fields. In an actual rotor, flow field differences and instabilities exist between blades. These differences and instabilities begin to form stall cells, which rotate around the compressor at speeds less than rotational speed [10]. Because the simulations are axis symmetric, they did not capture these stall precursor cells. So when the CFD program simulated either throttle or steam-induced stall, it stimulated the entire compressor stalling simultaneously. Stalling an entire axi-symmetric compressor simultaneously requires more throttling than stalling a complete compressor where individual passages may be more highly loaded. In addition to misrepresenting stall mechanics, the periodic boundary conditions actively introduced stability into the flow field. The forcing of identical fluid properties at the sides of the passage tends to damp out flow instabilities that form during quasi-steady-state runs. In throttle stall runs, these instabilities are inherent to the compressor operating at a low mass flow rate and in steam ingestion runs the changing inlet boundary conditions introduce instability into the flow field. The periodic boundary conditions partially moderated these flow instabilities. This moderation produced simulation results that stay stable beyond operating conditions where a full rotor simulation would have stalled. This increased stability and the differences in stall mechanics may contribute to the CFD simulations predicting stall with less mass flow rate than actually occurred

during physical experimentation. This phenomenon occurred during the 100% Speed simulations but not during the 95% speed simulations. As previously discussed, the 95% speed simulations may have greater instability amplification than the 100% speed simulations.

E. INDIVIDUAL CFD SIMULATION OBSERVATIONS

1. Throttle Simulations

Only the simulations from 95% speed are considered for discussion. The 100% speed simulations follow the 95% speed simulations' trends, but as mentioned previously the 100% speed steam ingestion simulations use 95% speed steam data. Figures 33, 34, 35, and 36 display the pressure distributions on the outer casing of each rotor passage as mass flow decreases. Each figure's corrected mass flow rate is listed in the figure title, and mass flow and blade movement direction are noted.

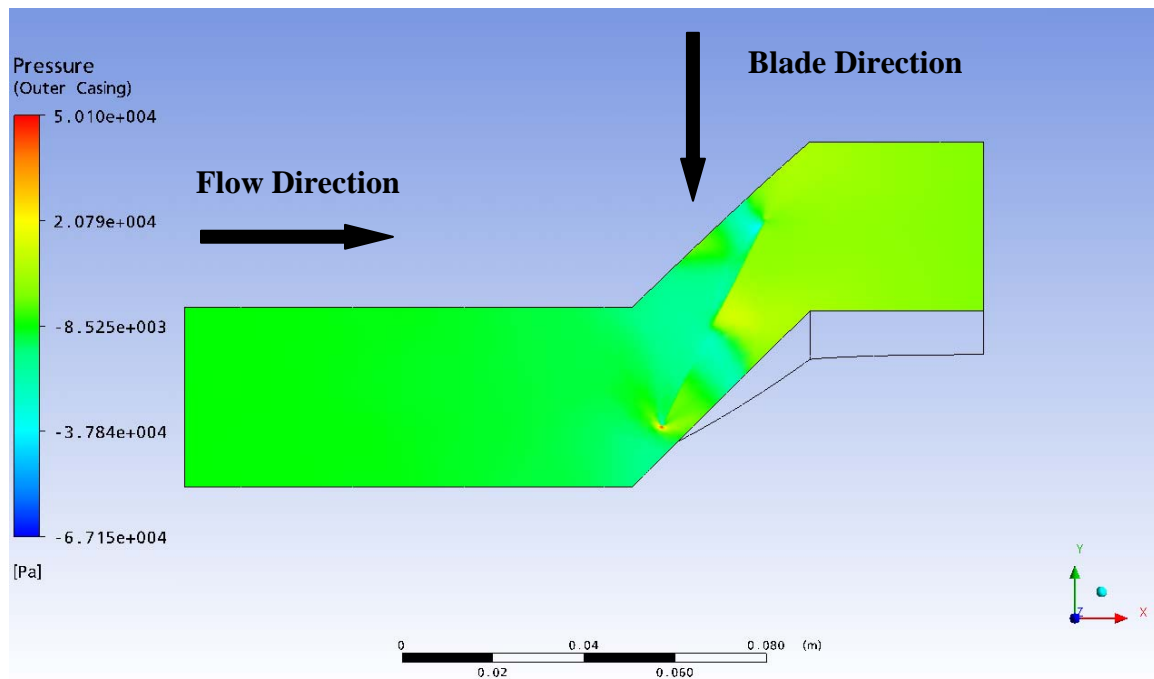


Figure 33. 95% Speed Outer Casing Pressure Distribution at Open Throttle, 7.715 kg/s (3.500 lbm/s)

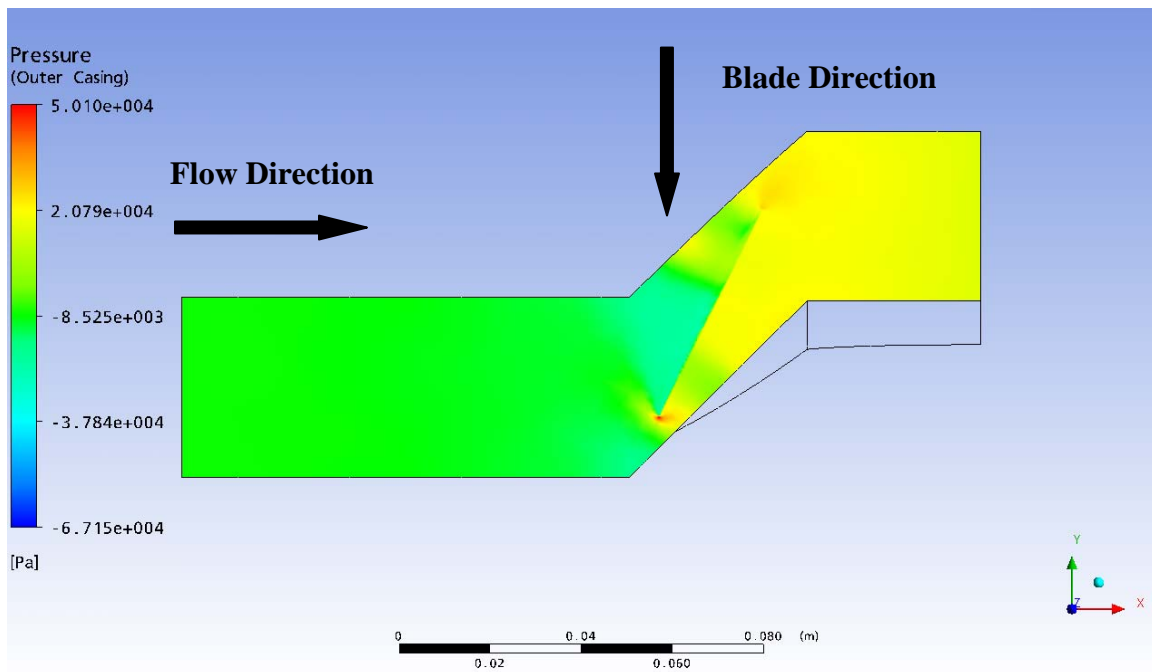


Figure 34. 95% Speed Outer Casing Pressure Distribution Near Maximum Efficiency, 7.402 kg/s (3.358 lbm/s)

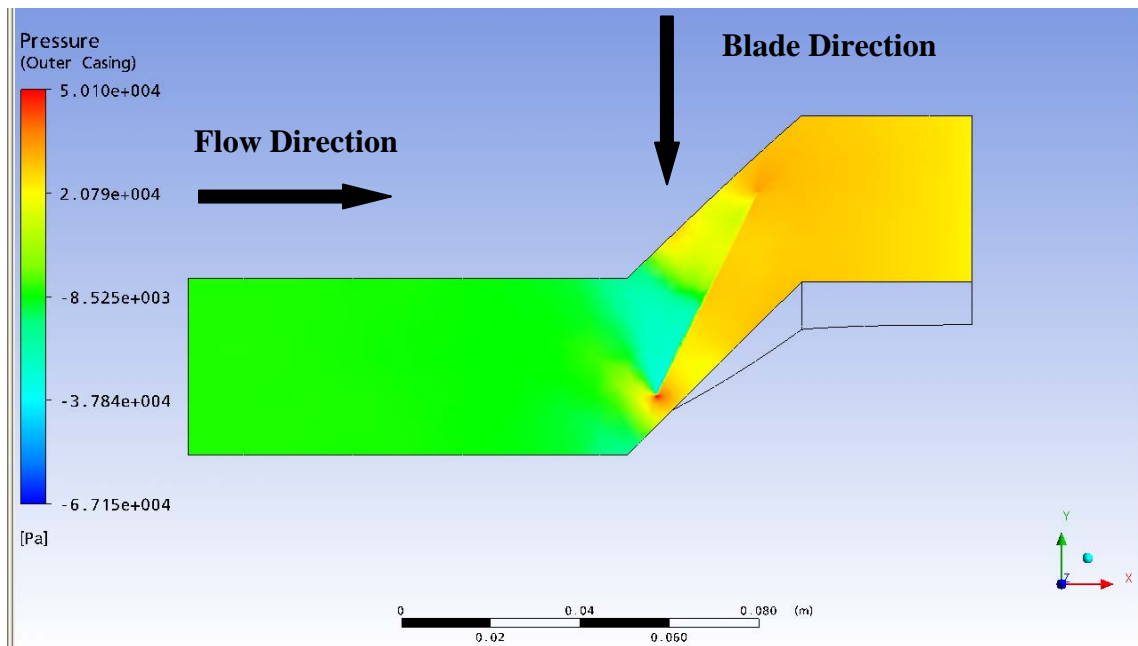


Figure 35. 95% Speed Outer Casing Pressure Distribution at the Steam Stall Point, 6.875 kg/s (3.118 lbm/s)

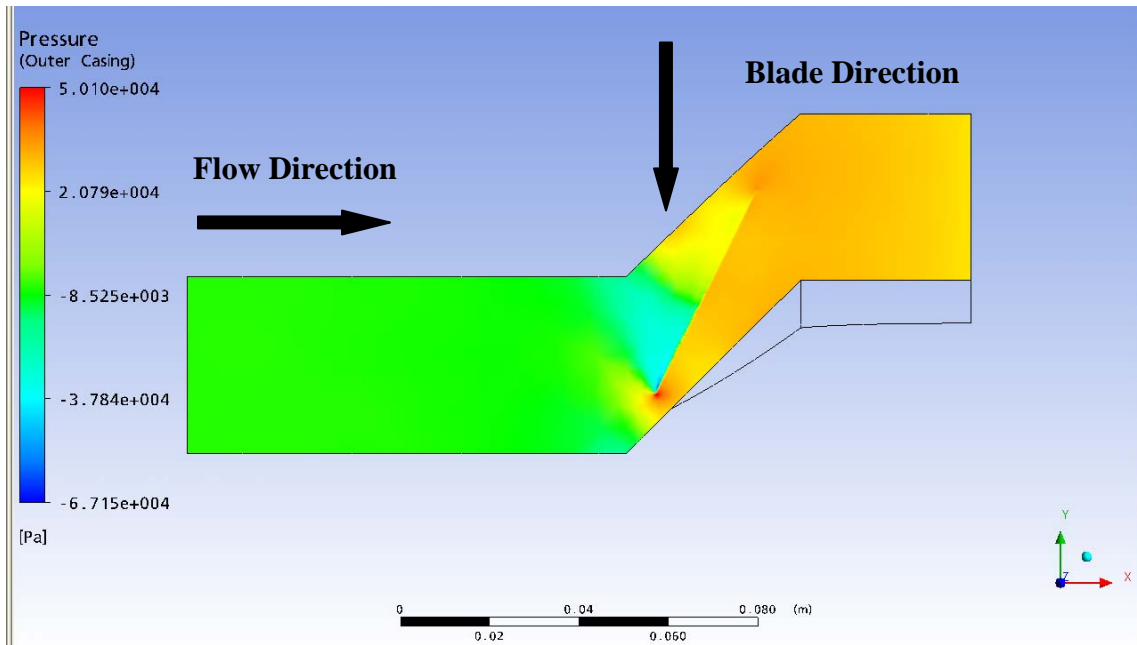


Figure 36. 95% Speed Outer Casing Pressure Distribution Near Stall, 6.620 kg/s (3.005 lbm/s)

Since ANYS CFX did not have a shock detection function for rotating computational domains, the shocks had to be observed by examining the pressure plots. The shocks can be detected by large sudden changes in pressure. These figures indicate that as mass flow decreased the shocks moved closer to the passage inlet. This general shock behavior was also observed by Gannon and Hobson [11] and Davis [12] in the physical compressor using Kulite pressure sensors placed on the outer casing.

2. Steam Ingestion Simulations

Figures 37, 38, 39, and 40 display the pressure distribution on the outer casing as the rotor undergoes steam ingestion. Each figure is labeled with simulation time and inlet temperature. Mass flow and blade movement direction are noted on the figures. Like the throttle cases, shocks can be detected by locating large sudden changes in pressure.

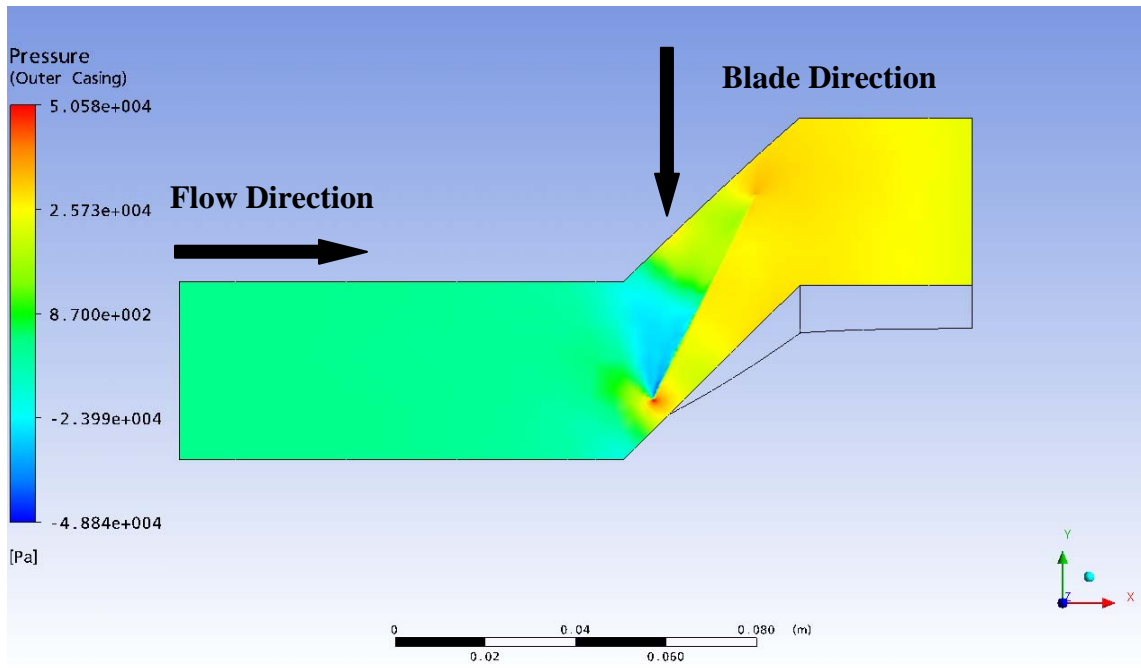


Figure 37. 95% Speed Outer Casing Pressure Distribution, Time = 0 seconds, Inlet Temperature = 293.15 K (527.67 °R)

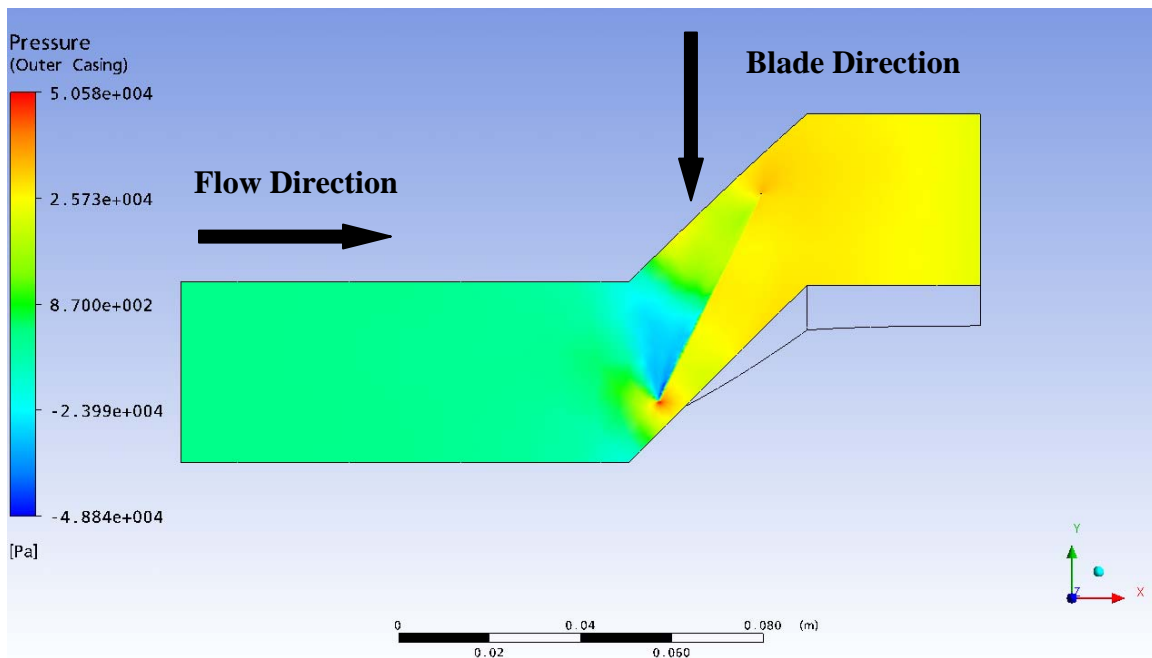


Figure 38. 95% Speed Outer Casing Pressure Distribution After a Half Second of Steam Ingestion, Time = 2.5 seconds, Inlet Temperature = 296.75 K (534.15 °R)

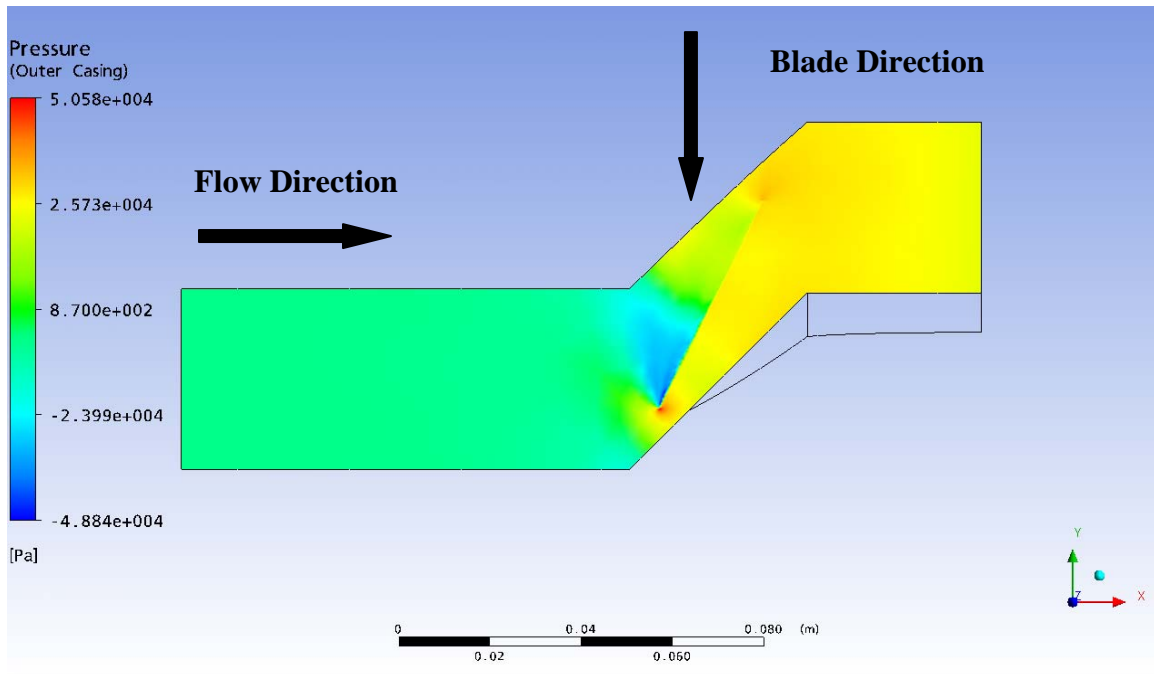


Figure 39. 95% Speed Outer Casing Pressure Distribution After One Second of Steam Ingestion, Time = 3 seconds, Inlet Temperature = 300.5 K (540.9 °R)

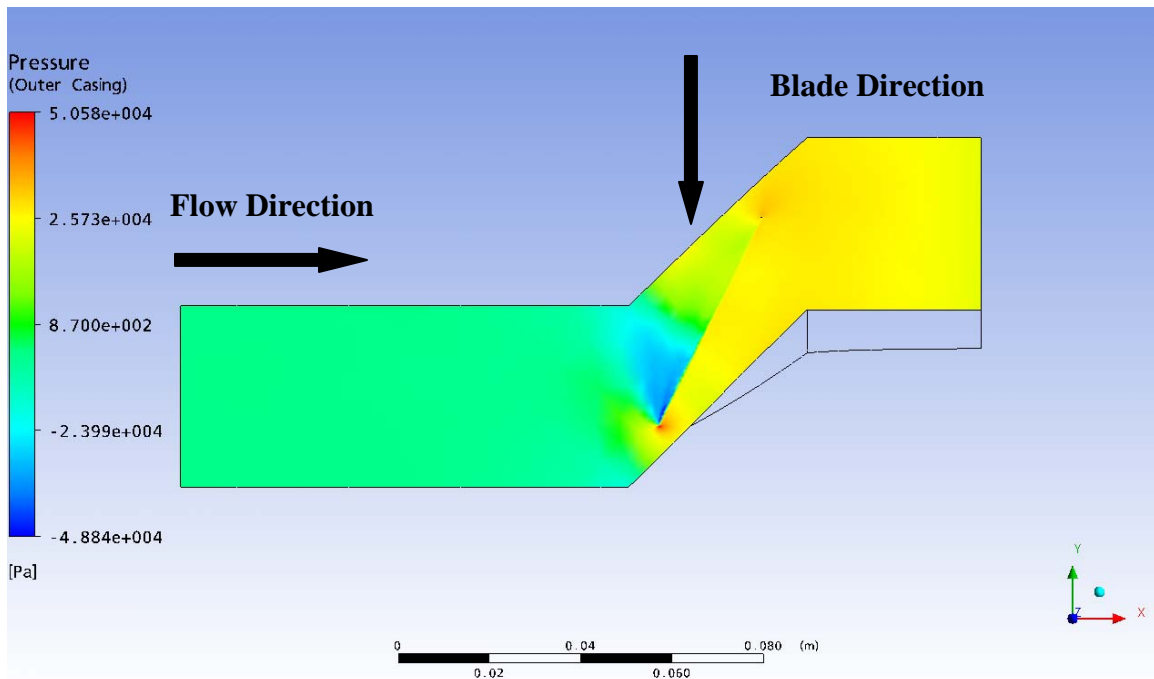


Figure 40. 95% Speed Outer Casing Pressure Distribution After 1.5 Seconds of Steam Ingestion, Time = 3.5 seconds, Inlet Temperature = 304.25 K (547.65 °R)

These figures show that as the steam ingestion simulation continue the shocks moved slightly towards the compressor inlet. Also the low pressure and high speed zone intensified as steam ingestion occurs. The shock movement towards the inlet that occurred during steam ingestion resembled shock behavior during throttling. Mass flow rate and density also decreased during the simulated steam ingestion event. Figure 41 plots mass flow rate vs. time for the simulated steam ingestion event, and Figure 42 plots the average inlet density vs. time.

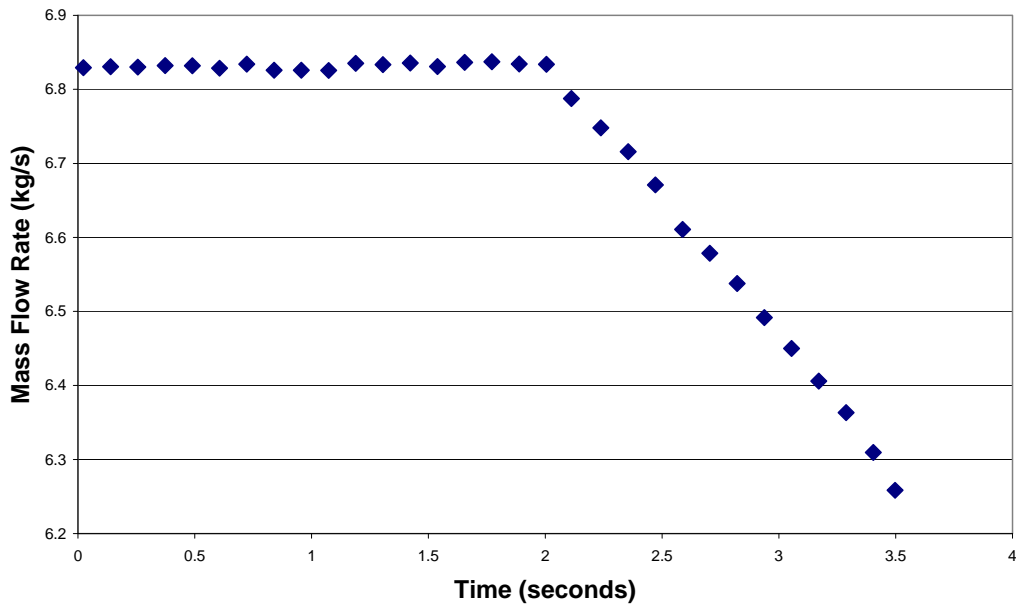


Figure 41. 95% Speed Mass Flow Rate Plot as Steam Ingestion Occurs

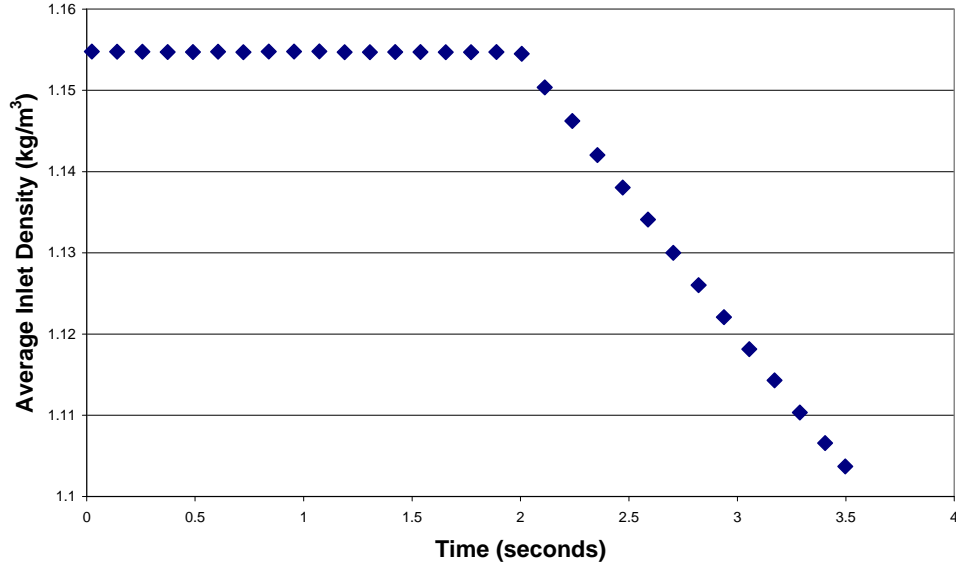


Figure 42. 95% Speed Average Inlet Density Plot as Steam Ingestion Occurs

The linear change in mass flow rate and density seemed directly related to the linear changes in temperature and mass fraction. The final steam ingestion mass flow rate at 95% speed of 6.258 kg/s (2.841 lbm/s) was less than the throttle stall mass flow rate of 6.620 kg/s (3.005 lbm/s). The changing simulation gas properties may have reduced the mass flow rate to a throttle stall point. These properties would be difficult to be properly non-dimensionalized and compared to the CFD compressor maps because the performance variables are dependent on specific heat ratio, γ . The specific heat ratio changes as steam is ingested. This dependency is given by Hill and Peterson [9] as,

$$\frac{p_{02}}{p_{01}}, \eta_c = f \left(\frac{\dot{m} \sqrt{\gamma R T_{01}}}{p_{01} D^2}, \frac{\Omega D}{\sqrt{R T_{01}}}, \frac{\Omega D^2}{\nu}, \gamma, design \right)$$

Though this steam stall point cannot be accurately placed on the compressor maps as a throttle point, the simulation may be undergoing a throttle like stall.

In order to more fully grasp simulated shock behavior during a steam ingestion event, a Mach one isosurface was generated within the passage. This isosurface was colored to display local temperature distribution. Figures 43, 44, 45, and 46 display the isosurface, as time advanced within the simulation. Each figure is labeled with time and inlet temperature.

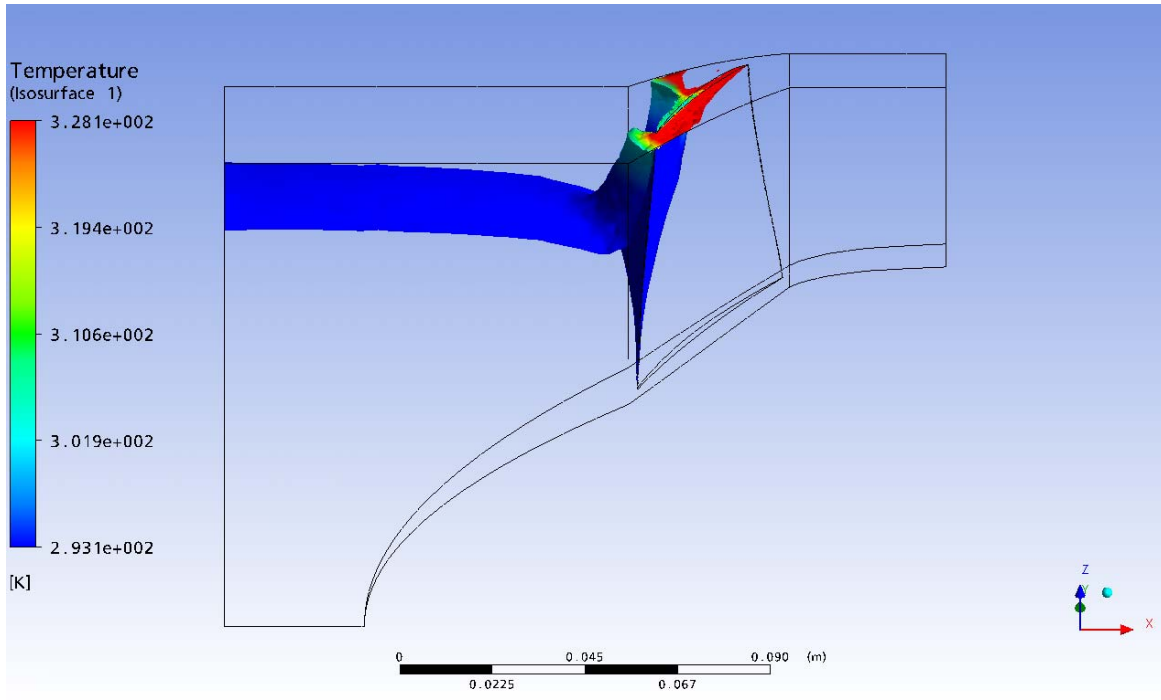


Figure 43. 95% Speed Mach One Isosurface, Time = 0 seconds, Inlet Temperature = 293.15 K (518.67 °R)

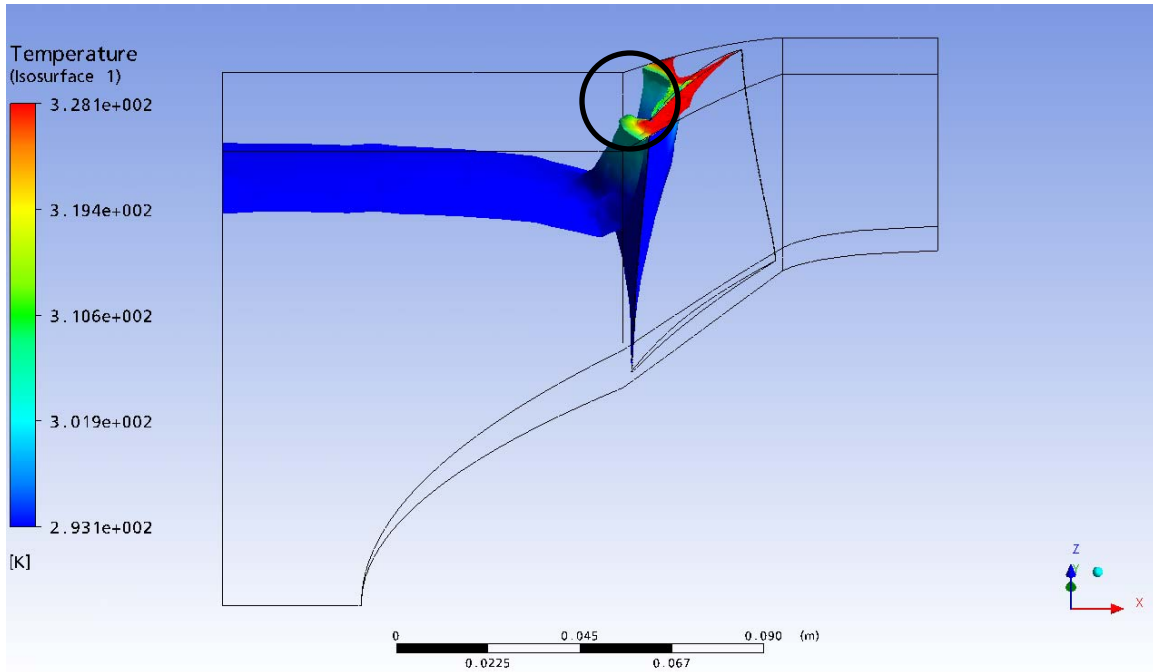


Figure 44. 95% Speed Mach One Isosurface After a Half Second of Steam Ingestion, Time = 2.5 seconds, Inlet Temperature = 296.75 K (527.67 °R)

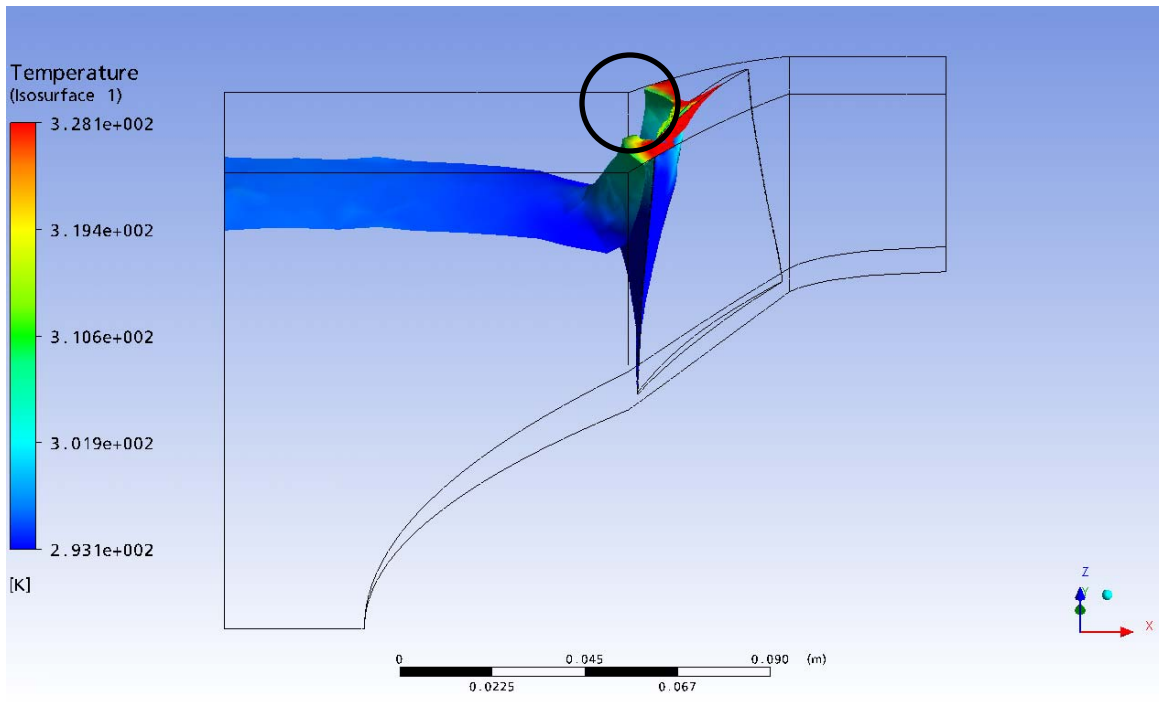


Figure 45. 95% Speed Mach One Isosurface After One Second of Steam Ingestion, Time = 3 seconds, Inlet Temperature = 300.5 K (534.15 °R)

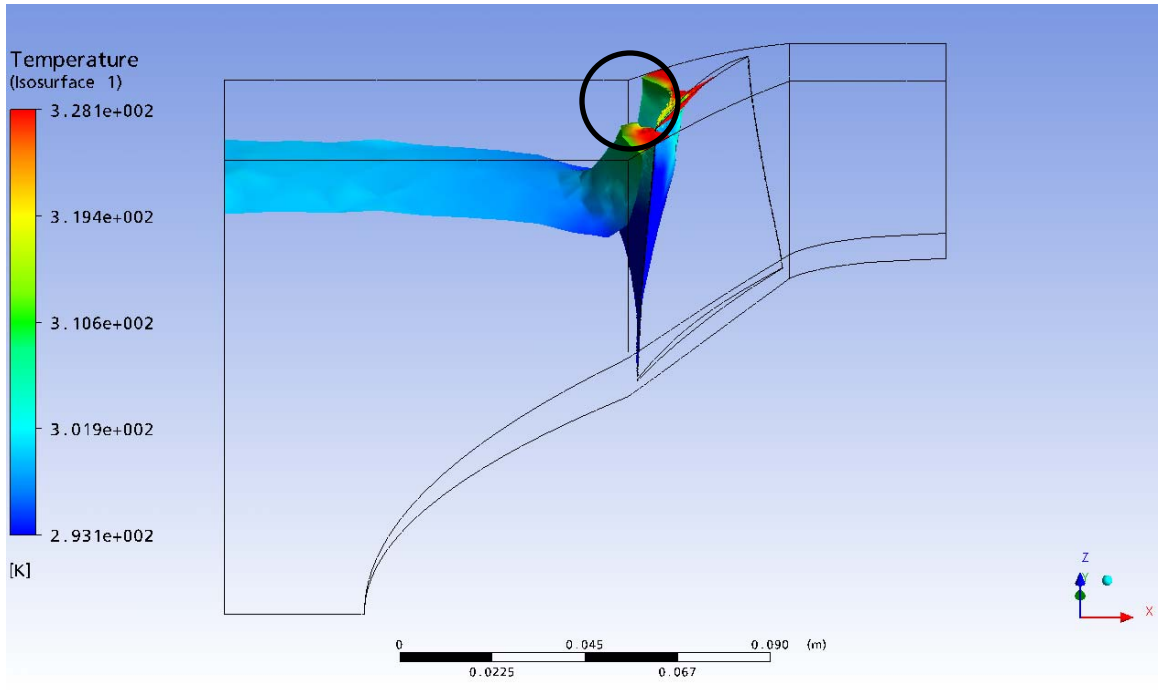


Figure 46. 95% Speed Mach One Isosurface After 1.5 Seconds of Steam Ingestion, Time = 3.5 Seconds, Inlet Temperature = 304.25 K (540.9 °R)

The Mach one surface approximates the location of the shocks within the passage. The extended isosurface flat section near the inlet of the passage is not a shock, but it indicates the location where the compressor rotates at Mach one. As steam is ingested into the passage, the temperature of the isosurface along the rotational section increases and the isosurface shock approximations move towards the inlet as seen in comparison of Figure 44 to Figures 45 and 46. The circles on the figures indicate a section of the isosurface that demonstrated this forward shock movement. This behavior resembles the changes that occur while throttling.

F. STEAM INGESTION RAMP FUNCTION SLOPE

In order to determine the effect of varying the ramp function slope on the steam stall point location, two new ramp functions were created. Figure 47 and Figure 48 display the new temperature and air mass fraction ramp functions with the original ramp functions.

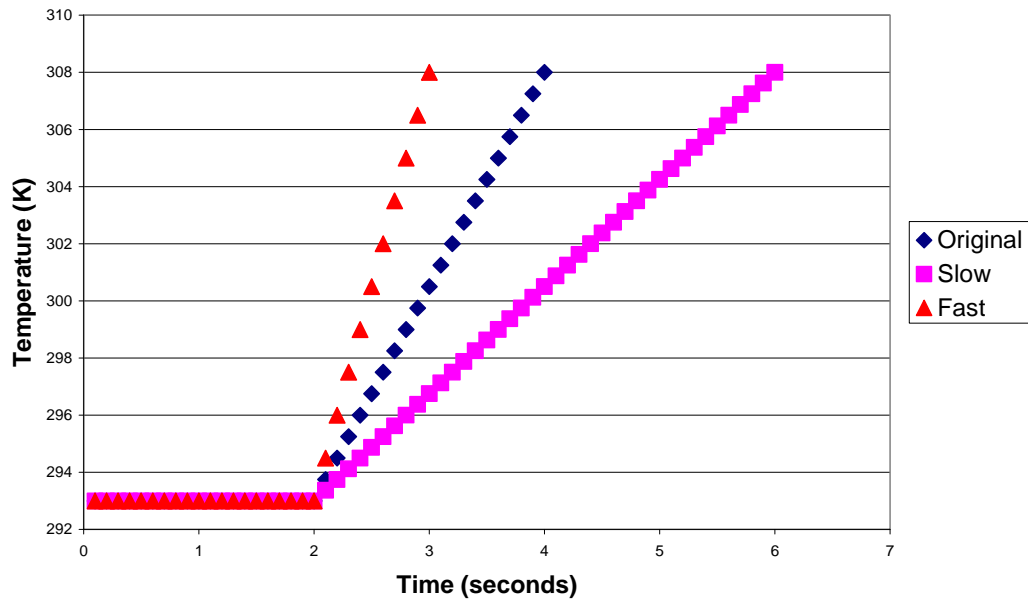


Figure 47. 95% Speed Various Temperature Ramp Functions

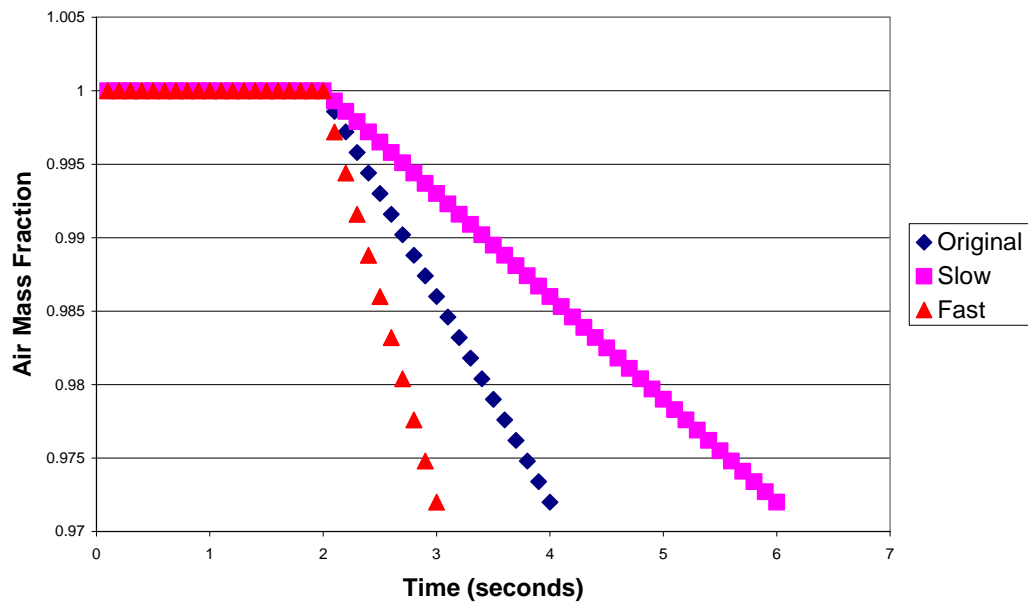


Figure 48. 95% Speed Various Air Mass Fraction Ramp Functions

Changing the ramp function had no effect on the steam stall point: with all three ramp functions steam-induced stall occurred using the same outlet pressure conditions. Steam-induced stall did not occur when lower back pressures, and therefore higher mass

flow rates, were set. These results indicate that final gas properties determined the steam-induced stall point in the model rather than ramp function slope. This ramp independence also supports the CFD rotor reaching a throttle stall point during steam ingestion. While ramp function slope did not affect the model's steam-induced stall point, the physical rotor may react differently. The physical rotor's steam stall mechanics differ from the CFD models, and, therefore, the ramp function slope may still have an effect on the physical steam-induced stall point.

VII. CONCLUSIONS

The objective of this study to develop a CFD simulation to predict and model the performance of Sanger Rotor in both normal and steam ingestion operations was achieved. Though the simulation results did not precisely match the physical experimental results, they did generate performance maps that matched the shape of the physical compressor maps. Quasi-steady-state simulations were shown to retain flow instabilities that steady-state simulations damped out, while being computationally cheaper than fully transient simulations. By maintaining these flow instabilities, more realistic simulation throttle-induced stall points were found. Simulation steam-induced stall points were also found by using quasi-steady-state simulations combined with changing inlet conditions. These simulation throttle points acted like their physical counterparts with steam-induced stall occurring at a higher mass flow rates than throttle-induced stall. The simulations' ability to replicate these performance trends adds confidence to their predictions. The 95% speed simulations had similar differences in stall margin between throttle and steam-induced stall as the physical experiment, which showed that CFD techniques can be used to estimate the stall reduction between throttle and steam-induced stall. Though relatively basic simulations were conducted using only one blade passage, the CFD model created compressor maps and performance trends that approximated the physical Sanger rotor's performance.

THIS PAGE INTENTIONALLY LEFT BLANK

VIII. RECOMMENDATIONS

Though the model did display considerable potential to simulate operating conditions on the Sanger rotor, additional modifications and research are needed to achieve higher levels of fidelity. The next computational grid created should have a finer y^+ resolution, which may allow for additional turbulence models to be tested as well as an increase in simulation accuracy. The physical hot shape of the rotor blade should be examined to insure that it and the computer blade model match. Simulation inlet temperature should be set at 288.15 K (518.67 °R) for non-steam ingestion simulations so that post-process mass flow rate normalization will be not required. The steam ingestion functions should be changed to reflect the new physical temperature slopes and maximums. The air mass fraction of this new steam ingestion data should also be examined in order to update the air mass fraction function. A rotor over-speed should also be included in the simulation during steam ingestion. Full rotor simulations should be conducted to investigate their performance versus the single blade passage model. Then a temperature distribution should be placed over the inlet that reflects the physical data. Fully transient simulations with appropriate Courant numbers should be conducted at throttle stall. A series of fully transient simulations should be run that have constant inlet conditions that are derived from specific times on the steam ingestion function. By keeping inlet conditions constant but conducting multiple simulations along the steam ingestion function, fully transient steam ingestion simulations can be made without running for the entire steam ingestion event duration. Fully transient simulations may provide more accurate flow field results than quasi-steady-state simulations. By implementing and testing these changes, a more accurate CFD model may be constructed.

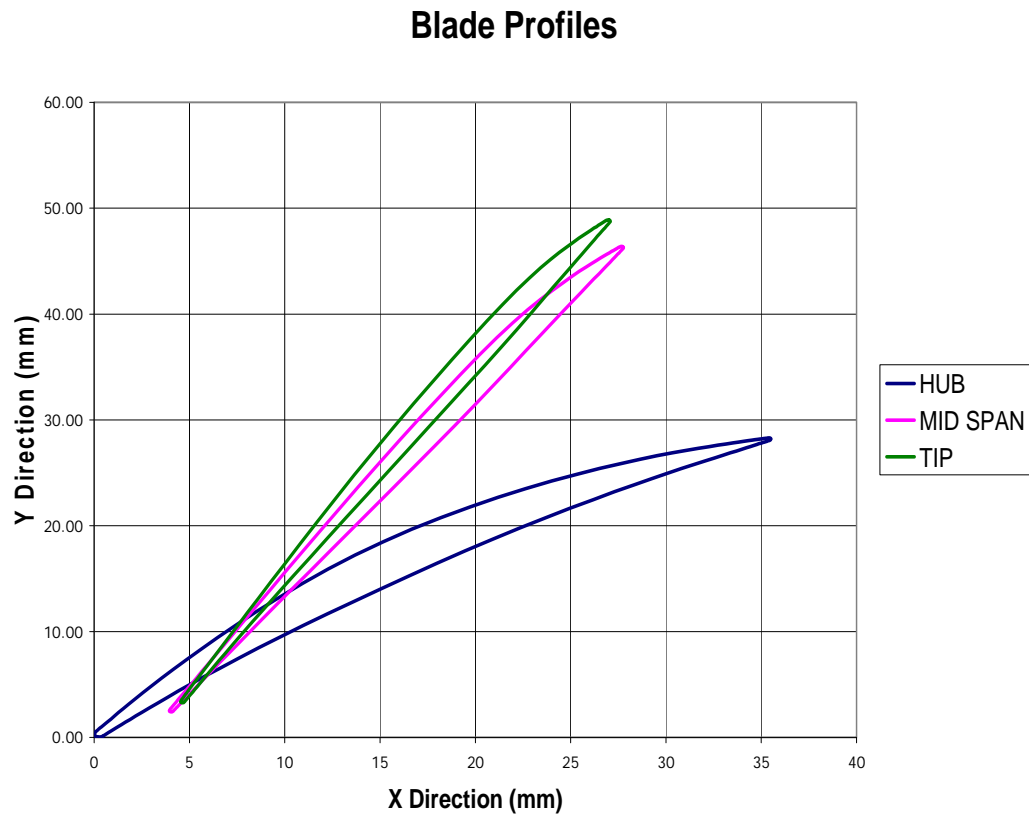
THIS PAGE INTENTIONALLY LEFT BLANK

LIST OF REFERENCES

- [1] N.I. Sanger, "Design of a low aspect ratio transonic compressor stage using CFD techniques." *ASME Journal of Turbomachinery*. Vol. 118. July, 1996, pp. 479–491
- [2] W. R. Levis, "Unsteady Casewall Pressure Measurements in a Transonic Compressor During Steam Induced Stall." M.S. thesis. Naval Postgraduate School, Monterey, California, June 2006.
- [3] T. A. Payne, "Inlet Flow-Field Measurements of a Transonic Compressor Rotor Prior to and During Steam-Induced Rotating Stall." M.S. thesis. Naval Postgraduate School, Monterey, California, December 2005.
- [4] S. E. Zarro, "Steady State and Transient Measurements Within a Compressor Rotor During Steam-Induced Stall at Transonic Operational Speeds." M.S. thesis. Naval Postgraduate School, Monterey, California, September 2006.
- [5] J.J. Koessler, "Experimental Investigation of High-Pressure Steam Induced Stall of a Transonic Rotor." M.S. thesis. Naval Postgraduate School, Monterey, California, June 2007.
- [6] A. M. Hurley, "Experimental Investigation of High-Pressure Steam-Induced Surge in a Transonic Compressor Stage." M.S. thesis. Naval Postgraduate School, Monterey, California, June 2008.
- [7] J. M. O'Brien, "Transonic Compressor Test Rig Rebuild and Initial Results with the Sanger Stage." M.S. thesis. Naval Postgraduate School, Monterey, California, June 2000.
- [8] A.J. Gannon, G.V. Hobson, T.A. Payne, and S.E. Zarro, "The Effect of Steam Ingestion on Transonic Rotor Stall Margin," *ASME GT2007–28068. Proceedings of TURBO EXPO*. Montreal, Canada, May 2007.
- [9] P. Hill and C. Peterson, *Mechanics and Thermodynamics of Propulsion*. Massachusetts: Addison-Wesley Publishing Company, Inc., 1992.
- [10] N.A. Cumpsty. *Compressor Aerodynamics*, New York: Longman Scientific & Technical, 1989.
- [11] A.J. Gannon and G.V. Hobson, "Pre-Stall Instability Distribution Over a Transonic Compressor Rotor." *ASME GT2008-51512. Proceedings of TURBO EXPO*. Berlin, Germany, June 2008.
- [12] W. L. Davis, "Stall Analysis in a Transonic Compressor Stage and Rotor." M.S. thesis. Naval Postgraduate School, Monterey, California, June 2009.

THIS PAGE INTENTIONALLY LEFT BLANK

APPENDIX A: SAMPLE BLADE PROFILES



THIS PAGE INTENTIONALLY LEFT BLANK

APPENDIX B: MODAL ANALYSIS ON A ROTOR BLADE

A modal analysis was conducted on the rotor blade geometry using the ANSYS modal simulation. The 11 profile final blade geometry was used in the simulation, and the bottom of the blade was fixed. The following table displays the first three physical modal frequencies and the first five simulation frequencies. The physical frequencies were found by O'Brien [7].

	Mode 1	Mode 2	Mode 3	Mode 4	Mode 5
Physical Frequencies (Hz)	750	2,700	3,000		
Simulation Frequencies (Hz)	757	2,719	2,932	5,198	5,534

Table 5. Physical and Simulation Modal Frequency Comparison

The first three simulation modal frequencies are close to the actual rotor blade frequencies. The simulation only modeled one blade but the physical blades were tested on the full rotor. The full rotor does have an effect on the individual blades' modal frequencies, which would result in differences between the physical results and the simulation results. The following five figures display the first five simulation modal frequencies' total deformation. The frequencies are given with a brief description of their movement characteristics.

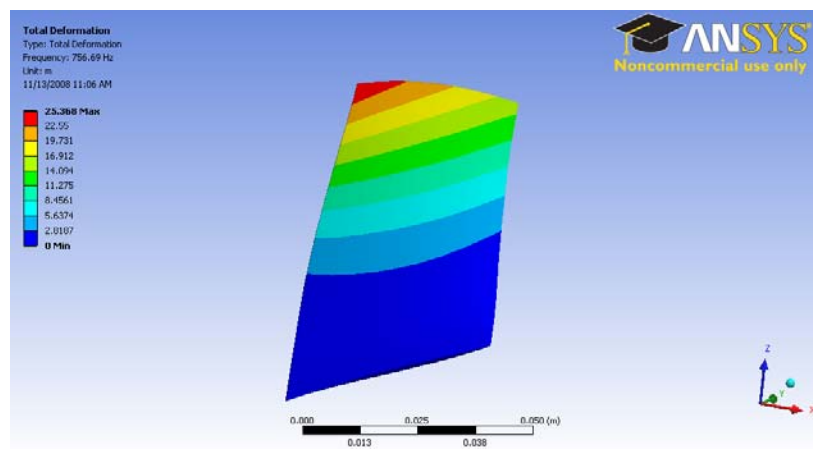


Figure 49. Mode 1: 756.69 Hertz. The top of the blade moves back and forth. Not much twisting occurs in the blade.

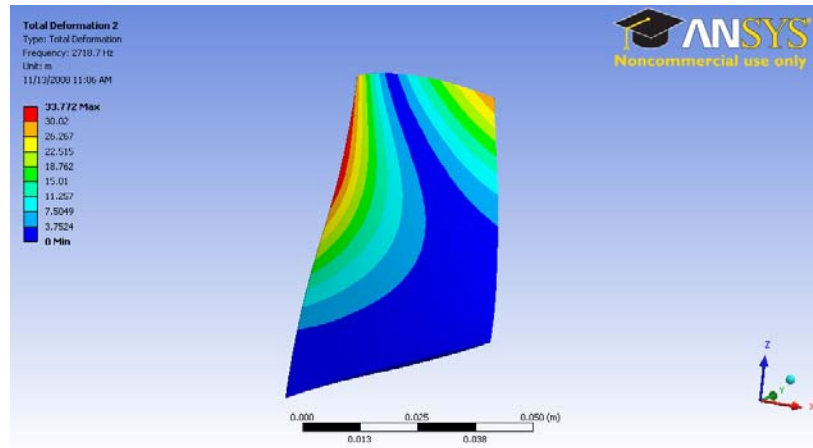


Figure 50. Mode 2: 2,718.7 Hertz. The top of the blade twists. The front edge buckles.

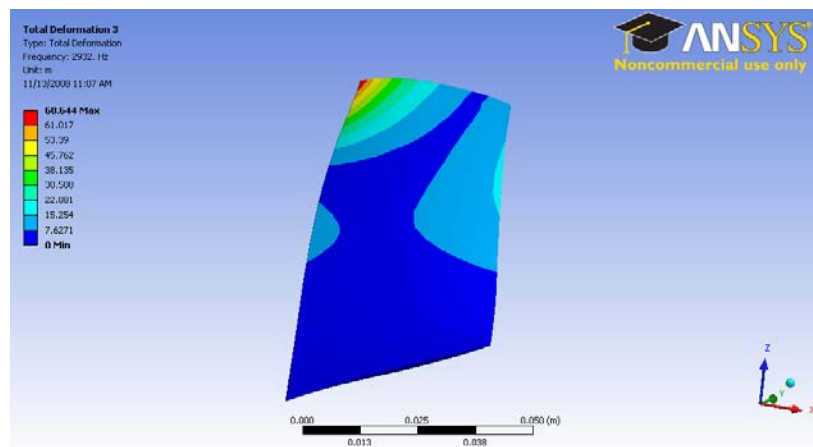


Figure 51. Mode 3: 2,932 Hertz. The front tip bends back and forth. The blade twists slightly.

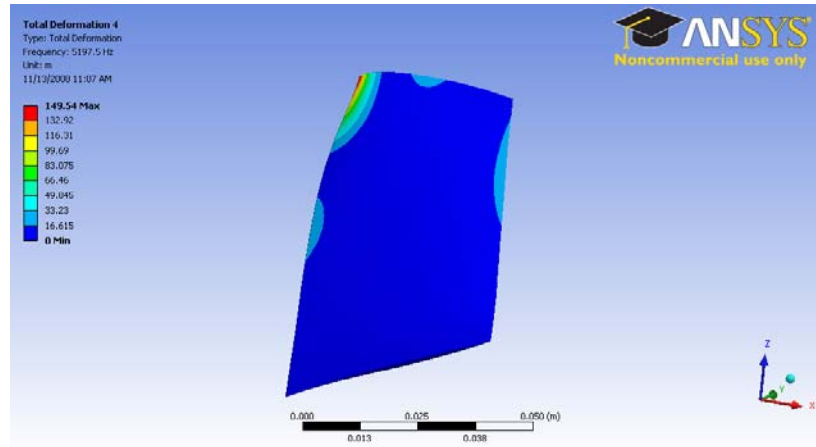


Figure 52. Mode 4: 5,197.5 Hertz. The front tip bends back and forth, but less of the tip bends than in mode 3. The blade twists slightly.

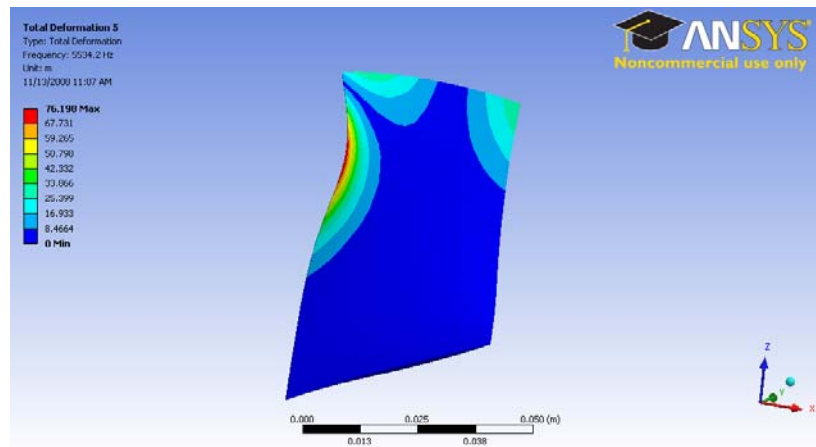


Figure 53. Mode 5: 5,534.2 Hertz. The top of the blade twists and the front edge buckles.

THIS PAGE INTENTIONALLY LEFT BLANK

APPENDIX C: GRID ITERATION PROCESS

A coarse model was first created and tested, and then refinements to that model were added and tested until the final grid was achieved. The first grid used a blade model composed of only three profiles and no tip gap. This model used an annulus geometry file exported from Solid Works as an IGES file. The use of an IGES file for the annulus created several geometric complications in the model. In the process of exportation and importation, the outer casing surface of the annulus was divided into two surfaces, and the hub nose section was split into several surfaces. Figure 54 displays these surfaces splits.

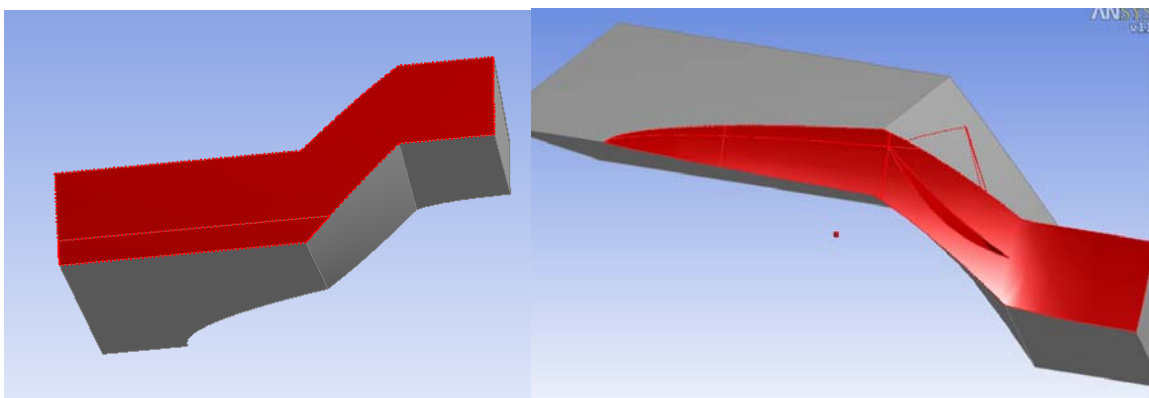


Figure 54. Split Surfaces on Outer Casing and Hub

In addition to splitting surfaces, the annulus's periodic sides had slightly different areas. This difference in area prevented the construction of a one to one periodic grid on both periodic sides. A periodic grid was established between the forward and rear periodic boundary sections, but the middle section was meshed without the periodic condition. In order to create a periodic boundary condition on the periodic sides for the simulation, the entire periodic sides were set as periodic boundaries in CFX-Pre while defining the simulation. On the middle sections, interpolation between sides was used since a one to one grid was not created. This interpolation added error to the simulation and increased computational costs. The meshing tool produced several warnings concerning small interior angles on the hub nose section surface grid. These warnings were noted, but the warnings did not prevent the generation of a surface and a volume

grid. This computational grid was then tested using CFX to check for stability and convergence. The testing boundary conditions and methods was elaborated on in the Steady State Simulations section.

The second computational grid iteration still used a three profile blade model, but it contained various improvements to the initial grid such as a tip gap between the rotor blade and outer casing. This tip gap was set at 1.00 mm (0.03937 in). This tip gap was significantly larger than the actual tip gap of the transonic compressor rig, but the tip gap did test the model's ability to include a space between rotor blade and outer casing. In order to place computational grid node points between the rotor blade and outer casing, the detect faces option of the proximity detection setting was turned on. At least four elements were placed between each surface. In addition to including a tip gap, this model exported the annulus from Solid Works as an STP file rather than an IGES file. The use of an STP file resolved many of the initial model's geometric problems. The outer casing surface and hub nose surfaces were imported as complete surfaces. Figure 55 displays these surfaces fully intact.

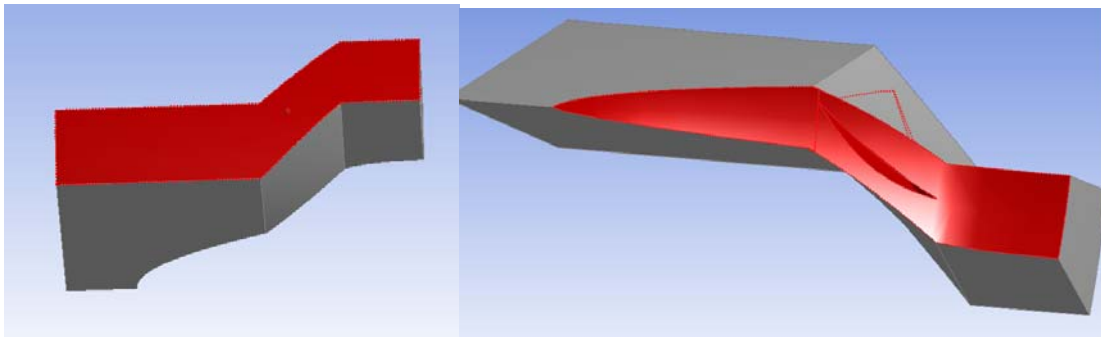


Figure 55. Fully Intact Outer Casing and Hub

Because the hub nose was one surface, fewer warnings about small interior angles occurred while meshing. Unlike the IGES export file, the STP export file had periodic sides with identical areas. This agreement in area allowed for the construction of one to one periodic boundary grids on the entire periodic sides. This grid construction eliminated interpolation on the periodic sides, and created more accurate and computationally cheaper simulations. Because of the improvements gained from changing the annulus file from IGES to STP, changing the rotor blade file to an STP file

was attempted. The blade STP file would not load into the ANSYS mesh program, so the original IGES file was used instead. This model also incorporated inflation boundaries on the outer casing and rotor blade and hub boundaries. Inflation boundaries were included to increase the simulation's boundary layer resolution. Five layers of inflation boundaries were set with a maximum thickness of 2.0 mm (0.07874 in). Like the first grid iteration, this grid was tested in CFX for stability and convergence.

THIS PAGE INTENTIONALLY LEFT BLANK

APPENDIX D: FINAL REFINED BLADE GRID MESH OPTIONS

Geometry

- Length Units: mm
- Transparency (%): 0
- Shine (%): 30

Verify Options

- Short Edge Limit [mm]: 0.18
- Sliver Factor Limit: 25

Fix Options

- Remove Short Edges: No

Solid

- Location: 1 Body

Virtual Topology

Virtual Topology

- Automatic Merge Strategy: Low

Automatic Merge Option

- Option: Entire Model

Regions

Default 2D Region

Outlet

Inlet

Rotor Casing

Outer Casing

Mesh

- Default Mesh Scale [mm]: 8.8
- Default Mesh Scale Factor [mm]: 1

Spacing

Default Body Spacing

- Maximum Spacing [mm]: 8.8

Default Face Spacing

- Option: Angular Resolution
- Angular Resolution [Degrees]: 30
- Minimum Edge Length [mm]: 0.44
- Maximum Edge Length [mm]: 8.8
- Radius of Influence [mm]: 0
- Expansion Factor: 1.2

Face Spacing 1

- Option: Angular Resolution
- Angular Resolution [Degrees]: 5
- Minimum Edge Length [mm]: 0.44
- Maximum Edge Length [mm]: 8.8
- Radius of Influence [mm]: 0

- Expansion Factor: 1.2
- Location: 1 2D Region (Nose)

Controls

Periodicity

Periodic Pairs 1

- Location 1: 3 2D Regions
- Location 2: 3 2D Regions

Periodic Type

- Option: Rotational
- Point: 0 [mm], 0 [mm], 0 [mm]
- Point: 1 [mm], 0 [mm], 0 [mm]

Inflation

Inflation

- Number of Inflated Layers: 5
- Expansion Factor: 1.2
- Number of Spreading Iterations: 4
- Minimum Internal Angle [Degrees]: 2.5
- Minimum External Angle [Degrees]: 10.0

Inflation Option

- Option: Total Thickness
- Thickness Multiplier: 1

Inflated Boundary 1

- Location: 6 2D Regions
- Maximum Thickness [mm]: 8.8

Stretch

- Stretch in X: 1
- Stretch in Y: 1
- Stretch in Z: 1

Proximity

- Edge Proximity: Yes
- Surface Proximity: Yes
- Elements Across Gap: 4
- Maximum Number of Passes 5

Options

Options

- Global Mesh Scale: 1

Surface Meshing

- Option: Delaunay

Meshing Strategy

- Option: Advancing Front and Inflation 3D

Volume Meshing

- Option: Advancing Front

APPENDIX E: STEADY-STATE SIMULATION SOLVER SETTINGS

Simulation

Simulation Type

Basic Settings

External Solver Coupling

- Option: None

Simulation Type

- Option: Steady State

Default Domain

General Options

Basic Settings

- Location: B40
- Domain Type: Fluid Domain
- Fluid List: mixture
- Coord Frame: Coord 0
- Particle Tracking: unselected

Domain Models

Pressure

- Reference Pressure: 1 [atm]

Buoyancy

- Option: Non Buoyant

Domain Motion

- Option: Rotating
- Angular Velocity: 25730.8 [rev min⁻¹]
- Alternate Rotational Model: unselected

Axis Definition

- Option: Coordinate Axis
- Rotation Axis: Global X

Mesh Deformation

- Option: None

Fluid Models

Heat Transfer

- Option: Total Energy
- Incl. Viscous Work Term: selected

Turbulence

- Option: k-Epsilon
- Wall Function: Scalable

Reaction or Combustion

- Option: None

Thermal Radiation Model

- Option: None

Component Details

- Air Ideal Gas
- Water Ideal Gas

Air Ideal Gas

- Option: Transport Equation
- Kinematic Diffusivity: unselected

Initialization

- Domain Initialization: unselected

Inlet

Basic Settings

- Boundary Type: Inlet
- Location: Inlet
- Coord Frame: unselected
- Frame Type: Stationary

Boundary Details

Flow Regime

- Option: Subsonic

Mass and Momentum

- Option: Stat. Frame Tot. Press.
- Relative Pressure: 0 [Pa]

Flow Direction

- Option: Normal to Boundary Condition

Turbulence

- Option: Medium (Intensity = 5%)

Heat Transfer

- Option: Stat. Frame Total Temp.
- Stat. Frame Tot. Temp: 20 [C]

Component Details

- Air Ideal Gas

Air Ideal Gas

- Option: Mass Fraction
- Mass Fraction: 1

Sources

- Boundary Source: unselected

Plot Options

- Boundary Contour: unselected
- Boundary Vector: unselected

Outer Casing

Basic Settings

- Boundary Type: Wall
- Location: Outer Casing
- Coord Frame: unselected
- Frame Type: Rotating

Thin Surfaces

- Create Thin Surface Partner: unselected

Boundary Details

Wall Influence On Flow

- Option: No Slip
- Wall Velocity: selected
 - Option: Counter Rotating Wall

Wall Roughness

- Option Smooth Wall

Heat Transfer

- Option: Adiabatic

Sources

- Boundary Source: unselected

Plot Options

- Boundary Contour: unselected
- Boundary Vector: unselected

Outlet

Basic Settings

- Boundary Type: Outlet
- Location Outlet
- Coord Frame: unselected
- Frame Type: Stationary

Boundary Details

Flow Regime

- Option: Subsonic

Mass and Momentum

- Option: Static Pressure
- Relative Pressure: .15 [atm]

Sources

- Boundary Source: unselected

Plot Options

- Boundary Contour: unselected
- Boundary Vector: unselected

Periodic Side 1

Basic Settings

- Boundary Type: Interface
- Location: F47.40,F51.40,F41.40
- Coord Frame: unselected

Boundary Details

Mass and Momentum

- Option: Conservative Interface Flux

Turbulence

- Option: Conservative Interface Flux

Heat Transfer

- Option: Conservative Interface Flux

Component Details

- Air Ideal Gas
- Air Ideal Gas
- Option: Conservative Interface Flux
 - Nonoverlap Conditions: unselected

Sources

- Boundary Source: unselected

Plot Options

- Boundary Contour: unselected
- Boundary Vector: unselected

Periodic Side 2

Basic Settings

- Boundary Type: Interface
- Location: F44.40,F43.40,F46.40
- Coord Frame: unselected

Boundary Details

Mass and Momentum

- Option: Conservative Interface Flux

Turbulence

- Option: Conservative Interface Flux

Heat Transfer

- Option: Conservative Interface Flux

Component Details

- Air Ideal Gas
- Air Ideal Gas
- Option: Conservative Interface Flux
 - Nonoverlap Conditions: unselected

Sources

- Boundary Source: unselected

Plot Options

- Boundary Contour: unselected
- Boundary Vector: unselected

Rotor Casing

Basic Settings

- Boundary Type: Wall
- Location: Rotor Casing
- Coord Frame: unselected
- Frame Type: Rotating

Thin Surfaces

- Create Thin Surface Partner: unselected

Boundary Details

Wall Influence On Flow

- Option: No Slip
- Wall Velocity: unselected

Wall Roughness

- Option Smooth Wall

Heat Transfer

- Option: Adiabatic

Sources

- Boundary Source: unselected

Plot Options

- Boundary Contour: unselected
- Boundary Vector: unselected

Periodic

Basic Settings

- Interface Type: Fluid Fluid

Interface Side 1

- Domain (Filter): Default Domain
- Region List: F41.40,F47.40,F51.40

Interface Side 2

- Domain (Filter): Default Domain
- Region List: F43.40,F44.40,F46.40

Interface Models

- Option: Rotational Periodicity

Axis Definition

- Option: Coordinate Axis
- Rotation Axis: Global Axis

Mesh Connection Method

- Option: 1:1

Solver

Solution Units

Basic Settings

- Mass Units: [kg]
- Length Units: [m]
- Time Units: [s]
- Temperature Units [K]
- Angle Units: selected
- Angle Units: [rad]
- Solid Angle Units: selected
- Solid Angle Units: [sr]

Solver Control

Basic Settings

Advection Scheme

- Option: High Resolution

Convergence Control

- Minimum Number of Iterations: unselected
- Max. Iterations: 10000

Fluid Timescale Control

- Timescale Control: Auto Timescale
- Length Scale Option: Conservative
- Timescale Factor: 1.0
- Maximum Timescale: unselected

Convergence Criteria

- Residual Type: RMS
- Residual Target: 0.00001
- Conservation Target: unselected
- Elapsed Time Control: unselected

Equation Class Settings

Equation Class

- Continuity
- Continuity: unselected

Advanced Options

Dynamic Model Control

- Global Dynamic Model Control: selected

Compressibility Control: selected

- High Speed Numerics: selected

Output Control

Results

- Option: Standard
- File Compression: Default
- Output Variable Operators: unselected
- Output Boundary Flows: unselected
- Output Equation Residuals: unselected

Backup

- None

Monitor

- Monitor Options: unselected

Export

- Efficiency Output: unselected

Mesh Adaptation

Basic Settings

- Activated Adaptation: selected
- Region List: Assembly
- Save Intermediate Files: selected

Adaptation Criteria

- Variables List: Absolute Pressure
- Max. Num. Steps: 3
- Option: Multiple of Initial Mesh
- Node Factor: 2.0

Adaptation Method

- Option: Solution Variation
- Minimum Edge Length: 0.0

Adaptation Convergence Criteria

- Max. Iter. Per Step: 500
- Residual Type: RMS
- Target Residual: 0.0001

Advanced Options

- Node Alloc. Param.: 0.0
- Number of Levels: 3

Expert Parameters

Convergence Control

High Speed Models

- Max continuity loops: selected
- Max continuity loops: 2

Materials

Air Ideal Gas

Water Ideal Gas

mixture

Basic Settings

- Option: Variable Composition Mixture
- Material Group: User
- Materials List: Air Ideal Gas, Water Ideal Gas
- Material Description: unselected
- Thermodynamic State: selected
- Thermodynamic State: Gas
- Coord Frame: unselected

Mixture Properties

- Mixture Properties: selected
- Option: Ideal Mixture

Thermodynamic Properties

- Equation of State: selected
- Option: Ideal Mixture

Specific Heat Capacity

- Option Ideal Mixture

Transport Properties: all unselected

Radiation Properties: all unselected

THIS PAGE INTENTIONALLY LEFT BLANK

APPENDIX F: THROTTLE STALL SIMULATION SOLVER SETTINGS

Simulation

Simulation Type

Basic Settings

External Solver Coupling

- Option: None

Simulation Type

- Option: Transient

Time Duration

- Option: Total Time
- Total Time: 4.01076 [s]

Time Steps

- Option: Timesteps
- Timesteps: 172*.0233184 [s]

Initial Time

- Option: Automatic with Value
- Time: 0 [s]

Default Domain

General Options

Basic Settings

- Location: B40
- Domain Type: Fluid Domain
- Fluid List: mixture
- Coord Frame: Coord 0
- Particle Tracking: unselected

Domain Models

Pressure

- Reference Pressure: 1 [atm]

Buoyancy

- Option: Non Buoyant

Domain Motion

- Option: Rotating
- Angular Velocity: 25730.8 [rev min⁻¹]
- Alternate Rotational Model: unselected

Axis Definition

- Option: Coordinate Axis
- Rotation Axis: Global X

Mesh Deformation

- Option: None

Fluid Models

Heat Transfer

- Option: Total Energy
- Incl. Viscous Work Term: selected

Turbulence

- Option: k-Epsilon
- Wall Function: Scalable

Reaction or Combustion

- Option: None

Thermal Radiation Model

- Option: None

Component Details

- Air Ideal Gas
- Water Ideal Gas

Air Ideal Gas

- Option: Transport Equation
- Kinematic Diffusivity: unselected

Initialization

- Domain Initialization: unselected

Inlet

Basic Settings

- Boundary Type: Inlet
- Location: Inlet
- Coord Frame: unselected
- Frame Type: Stationary

Boundary Details

Flow Regime

- Option: Subsonic

Mass and Momentum

- Option: Stat. Frame Tot. Press.
- Relative Pressure: 0 [Pa]

Flow Direction

- Option: Normal to Boundary Condition

Turbulence

- Option: Medium (Intensity = 5%)

Heat Transfer

- Option: Stat. Frame Total Temp.
- Stat. Frame Tot. Temp: 20 [C]

Component Details

- Air Ideal Gas

Air Ideal Gas

- Option: Mass Fraction
- Mass Fraction: 1

Sources

- Boundary Source: unselected

Plot Options

- Boundary Contour: unselected
- Boundary Vector: unselected

Outer Casing

Basic Settings

- Boundary Type: Wall
- Location: Outer Casing
- Coord Frame: unselected
- Frame Type: Rotating

Thin Surfaces

- Create Thin Surface Partner: unselected

Boundary Details

Wall Influence On Flow

- Option: No Slip
- Wall Velocity: selected
 - Option: Counter Rotating Wall

Wall Roughness

- Option Smooth Wall

Heat Transfer

- Option: Adiabatic

Sources

- Boundary Source: unselected

Plot Options

- Boundary Contour: unselected
- Boundary Vector: unselected

Outlet

Basic Settings

- Boundary Type: Outlet
- Location Outlet
- Coord Frame: unselected
- Frame Type: Stationary

Boundary Details

Flow Regime

- Option: Subsonic

Mass and Momentum

- Option: Static Pressure
- Relative Pressure: .15 [atm]

Sources

- Boundary Source: unselected

Plot Options

- Boundary Contour: unselected
- Boundary Vector: unselected

Periodic Side 1

Basic Settings

- Boundary Type: Interface

- Location: F47.40,F51.40,F41.40
- Coord Frame: unselected

Boundary Details

Mass and Momentum

- Option: Conservative Interface Flux

Turbulence

- Option: Conservative Interface Flux

Heat Transfer

- Option: Conservative Interface Flux

Component Details

- Air Ideal Gas

Air Ideal Gas

- Option: Conservative Interface Flux
- Nonoverlap Conditions: unselected

Sources

- Boundary Source: unselected

Plot Options

- Boundary Contour: unselected
- Boundary Vector: unselected

Periodic Side 2

Basic Settings

- Boundary Type: Interface
- Location: F44.40,F43.40,F46.40
- Coord Frame: unselected

Boundary Details

Mass and Momentum

- Option: Conservative Interface Flux

Turbulence

- Option: Conservative Interface Flux

Heat Transfer

- Option: Conservative Interface Flux

Component Details

- Air Ideal Gas

Air Ideal Gas

- Option: Conservative Interface Flux
- Nonoverlap Conditions: unselected

Sources

- Boundary Source: unselected

Plot Options

- Boundary Contour: unselected
- Boundary Vector: unselected

Rotor Casing

Basic Settings

- Boundary Type: Wall

- Location: Rotor Casing
- Coord Frame: unselected
- Frame Type: Rotating

Thin Surfaces

- Create Thin Surface Partner: unselected

Boundary Details

Wall Influence On Flow

- Option: No Slip
- Wall Velocity: unselected

Wall Roughness

- Option Smooth Wall

Heat Transfer

- Option: Adiabatic

Sources

- Boundary Source: unselected

Plot Options

- Boundary Contour: unselected
- Boundary Vector: unselected

Periodic

Basic Settings

- Interface Type: Fluid Fluid

Interface Side 1

- Domain (Filter): Default Domain
- Region List: F41.40,F47.40,F51.40

Interface Side 2

- Domain (Filter): Default Domain
- Region List: F43.40,F44.40,F46.40

Interface Models

- Option: Rotational Periodicity

Axis Definition

- Option: Coordinate Axis
- Rotation Axis: Global Axis

Mesh Connection Method

- Option: 1:1

Solver

Solution Units

Basic Settings

- Mass Units: [kg]
- Length Units: [m]
- Time Units: [s]
- Temperature Units [K]
- Angle Units: selected
- Angle Units: [rad]
- Solid Angle Units: selected

- Solid Angle Units: [sr]

Solver Control

Basic Settings

Advection Scheme

- Option: High Resolution

Transient Scheme

- Option: Second Order Backward Euler

Timestep Initialization

- Option: Automatic
- Lower Courant Number: unselected
- Upper Courant Number: unselected

Convergence Control

- Minimum Number of Coefficient Loops: unselected
- Max. Coeff. Loops: 100

Fluid Timescale Control

- Timescale Control: Coefficient Loops

Convergence Criteria

- Residual Type: RMS
- Residual Target: 0.0001
- Conservation Target: unselected
- Elapsed Time Control: unselected

Equation Class Settings

Equation Class

- Continuity
- Continuity: unselected

Advanced Options

Dynamic Model Control

- Global Dynamic Model Control: selected

Compressibility Control: selected

- High Speed Numerics: selected

Output Control

Results

- Option: Standard
- File Compression: Default
- Output Variable Operators: unselected
- Output Boundary Flows: unselected
- Output Equation Residuals: unselected

Backup

- None

Trn Results

Transient Results 1

- Option Standard
- File Compression: Default
- Output Boundary Flows: selected

- Boundary Flows: All
- Output Boundary Residuals: unselected

Output Frequency

- Option: Timestep Interval
- Timestep Interval: 5

Trn Stats

none

Monitor

- Monitor Options: unselected

Export

- Efficiency Output: unselected

Expert Parameters

Convergence Control

High Speed Models

- Max continuity loops: selected
- Max continuity loops: 2

Materials

Air Ideal Gas

Water Ideal Gas

mixture

Basic Settings

- Option: Variable Composition Mixture
- Material Group: User
- Materials List: Air Ideal Gas, Water Ideal Gas
- Material Description: unselected
- Thermodynamic State: selected
- Thermodynamic State: Gas
- Coord Frame: unselected

Mixture Properties

- Mixture Properties: selected
- Option: Ideal Mixture

Thermodynamic Properties

- Equation of State: selected
- Option: Ideal Mixture

Specific Heat Capacity

- Option Ideal Mixture

Transport Properties: all unselected

Radiation Properties: all unselected

THIS PAGE INTENTIONALLY LEFT BLANK

APPENDIX G: STEAM INGESTION SIMULATION SOLVER SETTINGS

Simulation

Simulation Type

Basic Settings

External Solver Coupling

- Option: None

Simulation Type

- Option: Transient

Time Duration

- Option: Total Time
- Total Time: 4.01076 [s]

Time Steps

- Option: Timesteps
- Timesteps: 172*.0233184 [s]

Initial Time

- Option: Automatic with Value
- Time: 0 [s]

Default Domain

General Options

Basic Settings

- Location: B40
- Domain Type: Fluid Domain
- Fluid List: mixture
- Coord Frame: Coord 0
- Particle Tracking: unselected

Domain Models

Pressure

- Reference Pressure: 1 [atm]

Buoyancy

- Option: Non Buoyant

Domain Motion

- Option: Rotating
- Angular Velocity: 25730.8 [rev min⁻¹]
- Alternate Rotational Model: unselected

Axis Definition

- Option: Coordinate Axis
- Rotation Axis: Global X

Mesh Deformation

- Option: None

Fluid Models

Heat Transfer

- Option: Total Energy
- Incl. Viscous Work Term: selected

Turbulence

- Option: k-Epsilon
- Wall Function: Scalable

Reaction or Combustion

- Option: None

Thermal Radiation Model

- Option: None

Component Details

- Air Ideal Gas
- Water Ideal Gas

Air Ideal Gas

- Option: Transport Equation
- Kinematic Diffusivity: unselected

Initialisation

- Domain Initialisation: unselected

Inlet

Basic Settings

- Boundary Type: Inlet
- Location: Inlet
- Coord Frame: unselected
- Frame Type: Stationary

Boundary Details

Flow Regime

- Option: Subsonic

Mass and Momentum

- Option: Stat. Frame Tot. Press.
- Relative Pressure: 0 [Pa]

Flow Direction

- Option: Normal to Boundary Condition

Turbulence

- Option: Medium (Intensity = 5%)

Heat Transfer

- Option: Stat. Frame Total Temp.
- Stat. Frame Tot. Temp: Statements

Component Details

- Air Ideal Gas

Air Ideal Gas

- Option: Mass Fraction
- Mass Fraction: mass fraction

Sources

- Boundary Source: unselected

Plot Options

- Boundary Contour: unselected
- Boundary Vector: unselected

Outer Casing

Basic Settings

- Boundary Type: Wall
- Location: Outer Casing
- Coord Frame: unselected
- Frame Type: Rotating

Thin Surfaces

- Create Thin Surface Partner: unselected

Boundary Details

Wall Influence On Flow

- Option: No Slip
- Wall Velocity: selected
 - Option: Counter Rotating Wall

Wall Roughness

- Option Smooth Wall

Heat Transfer

- Option: Adiabatic

Sources

- Boundary Source: unselected

Plot Options

- Boundary Contour: unselected
- Boundary Vector: unselected

Outlet

Basic Settings

- Boundary Type: Outlet
- Location Outlet
- Coord Frame: unselected
- Frame Type: Stationary

Boundary Details

Flow Regime

- Option: Subsonic

Mass and Momentum

- Option: Static Pressure
- Relative Pressure: .15 [atm]

Sources

- Boundary Source: unselected

Plot Options

- Boundary Contour: unselected
- Boundary Vector: unselected

Periodic Side 1

Basic Settings

- Boundary Type: Interface

- Location: F47.40,F51.40,F41.40
- Coord Frame: unselected

Boundary Details

Mass and Momentum

- Option: Conservative Interface Flux

Turbulence

- Option: Conservative Interface Flux

Heat Transfer

- Option: Conservative Interface Flux

Component Details

- Air Ideal Gas

Air Ideal Gas

- Option: Conservative Interface Flux
- Nonoverlap Conditions: unselected

Sources

- Boundary Source: unselected

Plot Options

- Boundary Contour: unselected
- Boundary Vector: unselected

Periodic Side 2

Basic Settings

- Boundary Type: Interface
- Location: F44.40,F43.40,F46.40
- Coord Frame: unselected

Boundary Details

Mass and Momentum

- Option: Conservative Interface Flux

Turbulence

- Option: Conservative Interface Flux

Heat Transfer

- Option: Conservative Interface Flux

Component Details

- Air Ideal Gas

Air Ideal Gas

- Option: Conservative Interface Flux
- Nonoverlap Conditions: unselected

Sources

- Boundary Source: unselected

Plot Options

- Boundary Contour: unselected
- Boundary Vector: unselected

Rotor Casing

Basic Settings

- Boundary Type: Wall

- Location: Rotor Casing
- Coord Frame: unselected
- Frame Type: Rotating

Thin Surfaces

- Create Thin Surface Partner: unselected

Boundary Details

Wall Influence On Flow

- Option: No Slip
- Wall Velocity: unselected

Wall Roughness

- Option Smooth Wall

Heat Transfer

- Option: Adiabatic

Sources

- Boundary Source: unselected

Plot Options

- Boundary Contour: unselected
- Boundary Vector: unselected

Periodic

Basic Settings

- Interface Type: Fluid Fluid

Interface Side 1

- Domain (Filter): Default Domain
- Region List: F41.40,F47.40,F51.40

Interface Side 2

- Domain (Filter): Default Domain
- Region List: F43.40,F44.40,F46.40

Interface Models

- Option: Rotational Periodicity

Axis Definition

- Option: Coordinate Axis
- Rotation Axis: Global Axis

Mesh Connection Method

- Option: 1:1

Solver

Solution Units

Basic Settings

- Mass Units: [kg]
- Length Units: [m]
- Time Units: [s]
- Temperature Units [K]
- Angle Units: selected
- Angle Units: [rad]
- Solid Angle Units: selected

- Solid Angle Units: [sr]
- Solver Control
- Basic Settings
- Advection Scheme
- Option: High Resolution
- Transient Scheme
- Option: Second Order Backward Euler
- Timestep Initialization
- Option: Automatic
 - Lower Courant Number: unselected
 - Upper Courant Number: unselected
- Convergence Control
- Minimum Number of Coefficient Loops: unselected
 - Max. Coeff. Loops: 100
- Fluid Timescale Control
- Timescale Control: Coefficient Loops
- Convergence Criteria
- Residual Type: RMS
 - Residual Target: 0.0001
 - Conservation Target: unselected
 - Elapsed Time Control: unselected
- Equation Class Settings
- Equation Class
- Continuity
 - Continuity: unselected
- Advanced Options
- Dynamic Model Control
- Global Dynamic Model Control: selected
- Compressibility Control: selected
- High Speed Numerics: selected
- Output Control
- Results
- Option: Standard
 - File Compression: Default
 - Output Variable Operators: unselected
 - Output Boundary Flows: unselected
 - Output Equation Residuals: unselected
- Backup
- None
- Trn Results
- Transient Results 1
- Option Standard
 - File Compression: Default
 - Output Boundary Flows: selected

- Boundary Flows: All
- Output Boundary Residuals: unselected

Output Frequency

- Option: Timestep Interval
- Timestep Interval: 5

Trn Stats

none

Monitor

- Monitor Options: unselected

Export

- Efficiency Output: unselected

Expert Parameters

Convergence Control

High Speed Models

- Max continuity loops: selected
- Max continuity loops: 2

Materials

Air Ideal Gas

Water Ideal Gas

mixture

Basic Settings

- Option: Variable Composition Mixture
- Material Group: User
- Materials List: Air Ideal Gas, Water Ideal Gas
- Material Description: unselected
- Thermodynamic State: selected
- Thermodynamic State: Gas
- Coord Frame: unselected

Mixture Properties

- Mixture Properties: selected
- Option: Ideal Mixture

Thermodynamic Properties

- Equation of State: selected
- Option: Ideal Mixture

Specific Heat Capacity

- Option Ideal Mixture

Transport Properties: all unselected

Radiation Properties: all unselected

Expressions

Expres

- 20[C]

Expres2

- 5[C]+7.5[C/s]*t

Expres3

- $-1.5[C/s]*t+41[C]$

Statements

- $\text{Expres}*\text{step}((t+.01[s])/(1[s]))- \text{Expres}*\text{step}((t-2[s])/(1[s]))+\text{Expres2}*\text{step}((t-2[s])/(1[s]))- \text{Expres2}*\text{step}((t-4[s])/(1[s]))+ \text{Expres3}*\text{step}((t-4[s])/(1[s]))- \text{Expres3}*\text{step}((t-14[s])/(1[s]))+ \text{Expres}*\text{step}((t-14[s])/(1[s]))$

massfrac1

- $.014[s^{-1}]*t-.028$

massfrac2

- $-.004[s^{-1}]*t+.44$

mass fraction

- $1-(\text{step}(t*1[s^{-1}]-2)*\text{massfrac1}- \text{step}(t*1[s^{-1}]-4)*\text{massfrac1}+ \text{step}(t*1[s^{-1}]-4)*\text{massfrac2}- \text{step}(t*1[s^{-1}]-11)*\text{massfrac2})$

APPENDIX H: TABULATED EXPERIMENTAL RESULTS

Throttle-Induced Stall Tests

70% Speed

Mass Flow Rate (kg/s)	Efficiency	Pressure Ratio
6.1412	0.8758	1.1490
6.1397	0.8770	1.1499
6.1411	0.8759	1.1495
6.1301	0.8749	1.1496
5.7587	0.8569	1.1927
5.7497	0.8525	1.1919
5.7450	0.8484	1.1913
5.7403	0.8516	1.1919
5.4409	0.8354	1.2175
5.4242	0.8354	1.2175
5.4238	0.8380	1.2187
5.4258	0.8376	1.2179
5.1908	0.8342	1.2336
5.2017	0.8378	1.2342
5.1914	0.8395	1.2335
5.2033	0.8380	1.2336
5.0930	0.8263	1.2393
5.1005	0.8248	1.2397
5.0993	0.8253	1.2400
5.1199	0.8269	1.2395
4.9748	0.8190	1.2480
5.0007	0.8203	1.2488
4.9468	0.8161	1.2475
4.9849	0.8186	1.2475
4.8134	0.7986	1.2563
4.7834	0.7983	1.2572
4.8528	0.7992	1.2572
4.7714	0.7991	1.2564
4.6337	0.7829	1.2702
4.6010	0.7837	1.2702
4.6248	0.7792	1.2693
4.5078	0.7780	1.2690
4.3989	0.7636	1.2773
4.4632	0.7654	1.2775
4.4347	0.7647	1.2775
4.3984	0.7608	1.2766

80% Speed

Mass Flow Rate (kg/s)	Efficiency	Pressure Ratio
6.9373	0.8675	1.1967
6.9167	0.8683	1.1963
6.9205	0.8689	1.1965
6.9149	0.8671	1.1967
6.5633	0.8610	1.2627
6.5761	0.8607	1.2628
6.5481	0.8593	1.2619
6.5639	0.8603	1.2621
6.1917	0.8504	1.3044
6.1858	0.8547	1.3048
6.1999	0.8546	1.3050
6.2048	0.8561	1.3051
5.8776	0.8384	1.3321
5.8803	0.8350	1.3319
5.8857	0.8364	1.3326
5.8634	0.8310	1.3323
5.5760	0.8075	1.3537
5.5763	0.8070	1.3530
5.5677	0.8059	1.3527
5.5536	0.8067	1.3533
5.3050	0.7746	1.3696
5.3108	0.7768	1.3699
5.3047	0.7748	1.3691
5.2865	0.7714	1.3686
5.2293	0.7719	1.3729
5.2365	0.7685	1.3725
5.2506	0.7703	1.3731
5.2334	0.7711	1.3729
5.1789	0.7609	1.3765
5.1729	0.7619	1.3768
5.1732	0.7610	1.3764
5.1694	0.7661	1.3773
5.0915	0.7524	1.3812
5.0751	0.7462	1.3801
5.0756	0.7499	1.3812
5.0798	0.7481	1.3808
4.9941	0.7395	1.3850
4.9876	0.7422	1.3848
4.9919	0.7445	1.3846
4.9908	0.7480	1.3856

90% Speed

Mass Flow Rate (kg/s)	Efficiency	Pressure Ratio
7.6132	0.8374	1.2501
7.6097	0.8376	1.2500
7.6242	0.8281	1.2497
7.6178	0.8260	1.2497
7.4720	0.8584	1.3250
7.4871	0.8669	1.3255
7.4627	0.8631	1.3250
7.4787	0.8620	1.3255
7.2610	0.8545	1.3819
7.2731	0.8598	1.3825
7.2707	0.8629	1.3825
7.2697	0.8665	1.3833
7.0125	0.8604	1.4213
6.9954	0.8614	1.4214
7.0144	0.8633	1.4216
7.0007	0.8681	1.4216
6.5164	0.8213	1.4676
6.5232	0.8241	1.4670
6.5213	0.8272	1.4683
6.5417	0.8270	1.4674
6.0953	0.7878	1.4955
6.1073	0.7846	1.4957
6.1085	0.7818	1.4953
6.1068	0.7832	1.4954
5.9672	0.7672	1.5034
5.9582	0.7698	1.5033
5.9647	0.7682	1.5039
5.9567	0.7715	1.5037

95% Speed

Mass Flow Rate (kg/s)	Efficiency	Pressure Ratio
7.9570	0.8145	1.2780
7.9433	0.8160	1.2776
7.9707	0.8186	1.2783
7.9665	0.8172	1.2773
7.8382	0.8381	1.3690
7.8410	0.8409	1.3680
7.8296	0.8428	1.3687
7.8586	0.8474	1.3682
7.6848	0.8500	1.4413
7.6788	0.8448	1.4412
7.6783	0.8452	1.4411
7.6738	0.8414	1.4404
7.4469	0.8574	1.4832
7.4460	0.8568	1.4825
7.4512	0.8596	1.4840
7.4530	0.8548	1.4818
7.1023	0.8293	1.5311
7.0947	0.8270	1.5300
7.0792	0.8307	1.5321
7.0915	0.8285	1.5311
6.7510	0.8025	1.5566
6.7472	0.8004	1.5576
6.7557	0.8058	1.5585
6.7517	0.8036	1.5575
6.4829	0.7843	1.5756
6.4722	0.7833	1.5744
6.4680	0.7851	1.5749
6.4668	0.7832	1.5749

100% Speed

Mass Flow Rate (kg/s)	Efficiency	Pressure Ratio
8.2790	0.8092	1.3059
8.2637	0.8043	1.3058
8.2727	0.8049	1.3053
8.2658	0.8032	1.3044
8.2081	0.8322	1.4071
8.2194	0.8312	1.4071
8.1948	0.8295	1.4060
8.1998	0.8297	1.4065
8.1158	0.8506	1.4823
8.1416	0.8539	1.4837
8.1479	0.8535	1.4835
8.1387	0.8519	1.4832
7.9998	0.8622	1.5327
7.9953	0.8645	1.5319
8.0040	0.8614	1.5313
8.0034	0.8623	1.5322
7.6637	0.8313	1.5913
7.6580	0.8287	1.5905
7.6629	0.8310	1.5913
7.6859	0.8293	1.5903
8.2907	0.8105	1.3058
8.2557	0.8058	1.3053
8.2835	0.8021	1.3053
8.2706	0.8042	1.3060
8.2050	0.8500	1.4379
8.1789	0.8453	1.4372
8.1979	0.8437	1.4368
8.1898	0.8464	1.4371
8.0644	0.8610	1.5135
8.0657	0.8591	1.5136
8.0555	0.8611	1.5137
8.0555	0.8552	1.5123
7.8610	0.8541	1.5646
7.8519	0.8521	1.5642
7.8540	0.8477	1.5632
7.8486	0.8472	1.5630
7.6307	0.8354	1.6025
7.6166	0.8335	1.6021
7.6212	0.8317	1.6022
7.6310	0.8323	1.6023
7.3300	0.8169	1.6336
7.3420	0.8192	1.6338
7.3357	0.8149	1.6335
7.3278	0.8133	1.6327

7.0747	0.7943	1.6502
7.0765	0.7941	1.6516
7.0852	0.7941	1.6507
7.1099	0.7912	1.6510
8.2648	0.8061	1.3059
8.2687	0.8081	1.3061
8.2624	0.8052	1.3066
8.2661	0.8029	1.3070
8.2054	0.8365	1.4040
8.2085	0.8358	1.4038
8.2194	0.8378	1.4042
8.2255	0.8414	1.4048
8.1254	0.8481	1.4745
8.1171	0.8461	1.4747
8.1173	0.8446	1.4741
8.1205	0.8485	1.4752
7.9654	0.8645	1.5356
7.9756	0.8655	1.5360
7.9820	0.8647	1.5359
7.9614	0.8699	1.5364
7.8694	0.8561	1.5567
7.8811	0.8580	1.5582
7.8777	0.8581	1.5574
7.8722	0.8581	1.5575

Steam-Induced Stall Tests

70% Speed

Mass Flow Rate (kg/s)	Efficiency	Pressure Ratio
6.0053	0.8364	1.1550
6.0043	0.8366	1.1547
6.0008	0.8383	1.1541
5.9962	0.8423	1.1546
5.6099	0.8396	1.1950
5.6174	0.8394	1.1950
5.6056	0.8443	1.1951
5.6200	0.8408	1.1950
5.0291	0.8116	1.2359
5.0681	0.8134	1.2357
5.0461	0.8089	1.2353
5.0358	0.8109	1.2354
4.8309	0.7868	1.2487
4.8255	0.7880	1.2483
4.8257	0.7872	1.2492
4.8300	0.7923	1.2492
4.6530	0.7671	1.2592
4.6528	0.7694	1.2588
4.6242	0.7655	1.2589
4.6571	0.7631	1.2585
4.5827	0.7563	1.2614
4.6019	0.7545	1.2612
4.6153	0.7534	1.2614
4.5659	0.7539	1.2616

80% Speed

Mass Flow Rate (kg/s)	Efficiency	Pressure Ratio
6.8971	0.8311	1.2035
6.9032	0.8324	1.2032
6.8784	0.8223	1.2027
6.8786	0.8267	1.2022
6.5447	0.8559	1.2615
6.5432	0.8566	1.2617
6.5449	0.8572	1.2612
6.5492	0.8605	1.2615
6.2362	0.8254	1.2946
6.2451	0.8282	1.2947
6.2585	0.8315	1.2952
6.2674	0.8448	1.2957
5.8695	0.8418	1.3293
5.8855	0.8371	1.3281
5.8651	0.8271	1.3278
5.8636	0.8217	1.3280
5.6776	0.8153	1.3412
5.6825	0.8120	1.3411
5.6653	0.8116	1.3411
5.6891	0.8111	1.3410
5.4110	0.7813	1.3588
5.3985	0.7804	1.3582
5.4011	0.7833	1.3579
5.3832	0.7865	1.3586
5.1918	0.7637	1.3729
5.1877	0.7639	1.3731
5.1901	0.7628	1.3728
5.1682	0.7585	1.3720

90% Speed

Mass Flow Rate (kg/s)	Efficiency	Pressure Ratio
7.3927	0.8414	1.3365
7.3843	0.8440	1.3369
7.3813	0.8468	1.3370
7.3874	0.8538	1.3362
7.1504	0.8551	1.3910
7.1474	0.8586	1.3913
7.1650	0.8589	1.3908
7.1511	0.8613	1.3904
6.9194	0.8461	1.4219
6.9365	0.8447	1.4207
6.9274	0.8476	1.4214
6.9352	0.8498	1.4212
6.4956	0.8208	1.4618
6.5133	0.8211	1.4620
6.5074	0.8210	1.4623
6.5064	0.8189	1.4616
6.1637	0.7890	1.4840
6.1658	0.7906	1.4839
6.1841	0.7933	1.4850
6.1860	0.7923	1.4850

95% Speed

Mass Flow Rate (kg/s)	Efficiency	Pressure Ratio
7.9330	0.8112	1.2884
7.9296	0.8110	1.2889
7.9323	0.8083	1.2883
7.9301	0.8079	1.2879
7.8123	0.8540	1.3737
7.8233	0.8514	1.3736
7.8114	0.8405	1.3721
7.8055	0.8437	1.3728
7.6245	0.8507	1.4358
7.6352	0.8525	1.4357
7.6482	0.8530	1.4364
7.6617	0.8541	1.4377
7.6559	0.8552	1.4368
7.6408	0.8522	1.4362
7.6516	0.8553	1.4372
7.4220	0.8542	1.4805
7.4306	0.8534	1.4799
7.3971	0.8513	1.4799
7.4139	0.8533	1.4801
7.2489	0.8324	1.5033
7.2309	0.8319	1.5020
7.2289	0.8320	1.5024
7.2443	0.8334	1.5026
7.0090	0.8142	1.5266
7.0082	0.8151	1.5271
6.9888	0.8160	1.5268
7.0225	0.8171	1.5276
6.6720	0.8009	1.5550
6.7150	0.7983	1.5534
6.6777	0.7976	1.5533
6.7202	0.7991	1.5533

INITIAL DISTRIBUTION LIST

1. Defense Technical Information Center
Ft. Belvoir, Virginia
2. Dudley Knox Library
Naval Postgraduate School
Monterey, California
3. Professor and Chairman Knox Millsaps
Department of Mechanical Engineering and Aeronautical Engineering
Naval Postgraduate School
Monterey, California
4. Professor Anthony Gannon
Department of Mechanical Engineering and Aeronautical Engineering
Naval Postgraduate School
Monterey, California
5. Professor Garth Hobson
Department of Mechanical Engineering and Aeronautical Engineering
Naval Postgraduate School
Monterey, California
6. ENS Collin Hedges
Monterey, California